_____

## SCUOLA DI SCIENZE
Dipartimento di Chimica Industriale "Toso Montanari"


Corso di Laurea Magistrale in
## Chimica Industriale
## Curriculum: Advanced Spectroscopy in Chemistry
Classe LM-71 - Scienze e Tecnologie per la Chimica Industriale


# Synthesis and characterization of defective PBAs electrode material

CANDIDATE            SUPERVISOR

**Anastassiya Khan**        **Prof. Marco Giorgetti**

CO-SUPERVISOR

**Dr. Dino Tonti**
**Dott. Min Li**

Session I

_____

**Academic Year 2019/2020**

_____

# Table of contents

# Abstract

Sodium manganese hexacyanoferrate (NaMnHCF) and its derivatives have been synthesized by simple co-precipitation method with addition of the citric and ascorbic acids respectively. The corresponded crystal structure, water content, chemical formula and a deep structural investigation of prepared samples have been performed by means of the combination of the laboratory and synchrotron techniques (PXRD, FT-IR, TGA, MP-AES and XAS). Electrochemical tests have been done using three-electrode system in sodium nitrate solution at different concentration. From cyclic voltammetry curves, $Fe^{3+/2+}$ redox peak has been observed, whereas $Mn^{3+/2+}$ peak was not always evident. Structural stability of the cycled samples has then been tested using 2D XRF imaging and Transmission X-ray microscopy (TXM) techniques. The intercalation of NaMnHCF after 20 cycles has been found by micro-XANES analysis of the highlighted spots which have been found in the XRF images. TXM has also confirmed the appearance of the intercalated particles after 50 cycles comparing the spectra between charged and discharged materials at three different edges (Mn, Fe and N). However, by comparison with lithium samples, it seems obvious that sodium samples are more homogeneous and intercalation is at the very beginning indicating the relative structural stability of sodium manganese hexacyanoferrate electrode material.

# 1. Literature survey

## 1.1 Batteries topics

### 1.1.1 Study background

In this growing age of clean energy and the use of power storage to circumvent the use of traditional fossil fuel technologies, batteries of greater capacity, storage, and power are increasingly becoming indispensable [1]. Possessing high energy density and design flexibility, batteries can be the best option for solving the problem of excessive supply of energy when demand is relatively low. Among the various existing types of batteries (figure 1 [2]), Li-based batteries currently outperform other systems, constituting for 63% of worldwide sales values in portable batteries. This explains current highest attention to them at both fundamental and applied levels [2, 3].
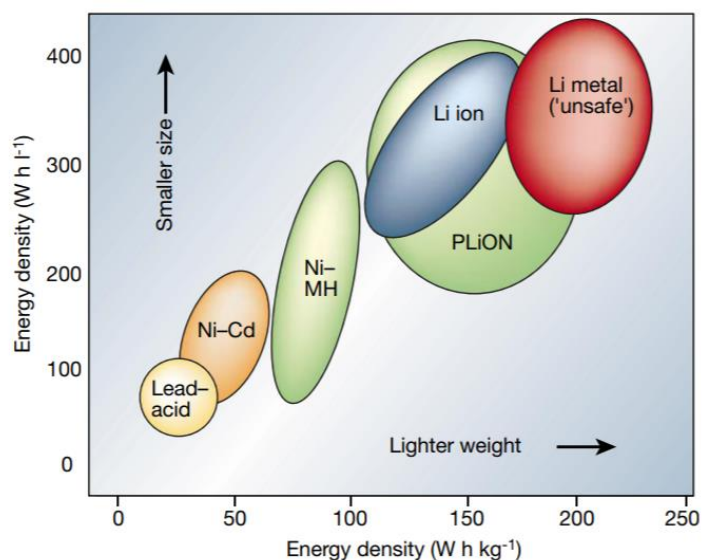


*Figure 1. Comparison of the different battery technologies in terms of volumetric*
*and gravimetric energy density.* [3]

The reason for using lithium as anode material in battery technology, based on the several facts. Firstly, Li has -3.045 V ve. SHE reduction potential, allowing Li based batteries to have the highest possible cell potential. Secondly, Li is the third lightest element and has one of the smallest ionic radii of any single charged ion. These factors allow Li-based batteries to have high gravimetric and volumetric capacity and power density [4]. The benefit of using Li metal was firstly showed in the 1970s with the assembly of first Li cells [5]. During that time, various inorganic compounds were

shown to react with alkali metals in a reversible way. The discovery of such materials, which were later identified as intercalation compounds, was of significant importance in the development of high-energy rechargeable Li systems [4]. In 1980s, Goodenough et al. proposed family of compound with general formula $Li_xMO_2$ (where M is Co, Ni or Mn) which are used almost exclusively as intercalation compounds in today's batteries [6]. Finally, in 1991 Sony Corporation produced C/LiCoO2 rocking-chair cell which has a potential exceeding 3.6 V (three times that of alkaline systems) and gravimetric energy densities as high as 120–150 W h $kg^{-1}$ (two to three times those of usual Ni–Cd batteries [7].

One of the main restrictions in production of lithium batteries today are still relative high cost, little abundance of Li and some of the transition metals currently used in Li-ion batteries and specific safety risks [8]. Currently new ways are being developed to increase the capacity of traditional lithium ion batteries and to develop batteries beyond lithium ion.

Sodium and potassium ion battery technology has recently paid high attention inside the scientific community, representing valid and more environmentally friendly alternative to Li-ion, owing to the abundance and accessibility of alkali metals (Na+, K+). Possessing similar trend of losing electrons and having relatively small difference in potential ( -2.924 V vs SGE for potassium; -2.711 V vs. SHE for sodium), alkali metals can be viable option for developing new systems without incorporation of Li-ion. Possibility of using the same research experiences as well as the developments in the electrodes of Li-ion batteries for new alkali-ion batteries can be seen as one of the main advantage of these materials.

### 1.1.2 Prussian blue (PB)

Prussian blue is definitely one of the most ancient coordination materials, which earliest announcements can be dated back to the very beginning of the eighteenth century [9, 10]. One of the key characteristic of this material is its zeolite-type open structure which was firstly investigated by Keggin and Miles using X-ray diffraction spectroscopy [11] and has been determined more precisely by Ludi and coworkers from single crystals by electron and neutron diffraction measurements [12]. PB crystallizes in a cubic structure (Fm–3 m space group) with lattice parameter a = 10.2 Å and consist of alternating iron(II) and iron(III) located on a face centered cubic lattice in such a way that the iron(III) ions are surrounded octahedrically by nitrogen atoms, and iron(II) ions are surrounded by carbon atoms [11]. The characteristic intense blue color can be attributed to the mixed-valence nature of compound and explained by corresponding charge transfer between two iron centers. PB can be crystallized in two different forms: «soluble» and «insoluble», which can be seen in Figure 2. It is important to mention here that term «solubility» is referred to the ease of peptization of compounds rather than actual solubility which is low for both forms ($K_{sp} = 10^{-40}$) [13]. In the first form ($KFe^{III}[Fe^{II}(CN)_6]$), Prussian Blue contains interstitial alkali metal ions (e.g., Na+ and K+) which are balancing the charge, whereas in the second form ($Fe^{III}_4[Fe^{II}(CN)_6]_3xH2O$) interstitial water molecules are presented. These water molecules can be divided into 2 groups: molecules that are coordinated to $M^{II}$ sites and the ones that are inside cavities and do not coordinate to the metal site.
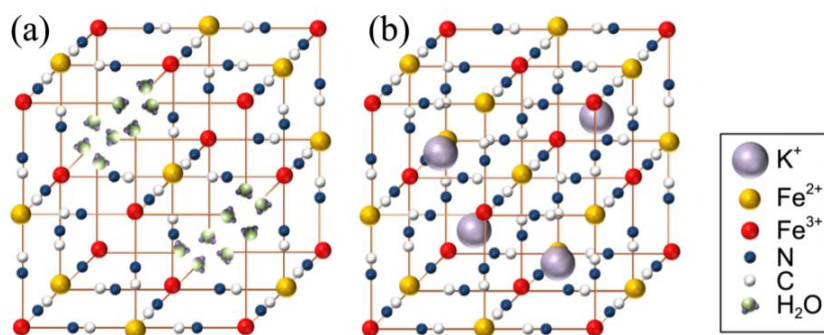


*Figure 2. The crystal structures of (a) insoluble and (b) soluble Prussian blue forms* [14].

One of the most important factors is to control morphology of Prussian blue because its structure has direct effect on its properties. Changing one of the synthetic parameter makes it possible to produce several crystalline shapes, sizes, and compositions which can lead to versatile applications of PB and its analogues for example in medicine as a sequestering agent [15, 16].

The structure of PB exhibits open channels suitable for ion diffusion which, along with the redox $Fe^{+2}/Fe^{+3}$ pair, result in an appealing electrochemical behavior first reported by Neff [17]. He showed that Prussian blue forms electroactive layers after chemical deposition onto the electrode surface, and has opened a new area in fundamental investigation of this unique inorganic polycrystal. Itaya and coworkers [18] showed that Prussian White (reduced form of PB) and Prussian Green (oxidized form of PB) can be formed by corresponding electrochemical reduction and oxidation processes which are summarized by equations 1 and 2:

(reduction of PB)

$$Fe^{III}_4[Fe^{II}(CN)_6]_3 + 4e^- + 4K^+ = K_4Fe_4^{II}[Fe^{II}(CN)_6]_3$$

(oxidation of PB)

$$Fe^{III}_4[Fe^{II}(CN)_6]_3 - 3e^- + 3Cl^= = Fe^{III}[Fe^{III}(CN)_6 Cl]_3$$
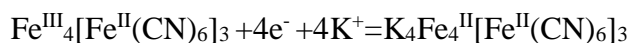
Cyclic voltammetric characteristic of the Prussian blue-modified electrode was tested in the aqueous medium of 1M KCl, and, as a result, two sets of peaks with a separation of 15–30 mV were observed, where the reduction of PB is accompanied with the loss of color and the oxidation – with subsequent change to yellow color [19].
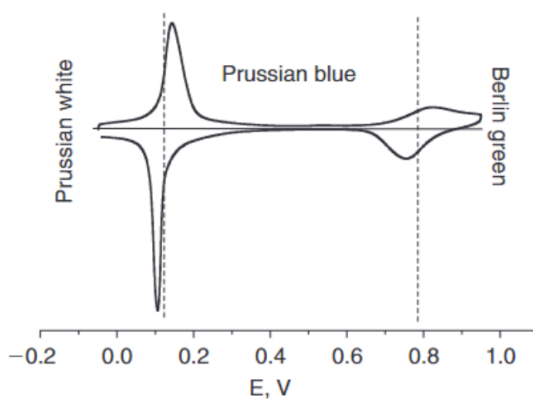


*Figure 3. Cyclic voltammogram of PB-modified electrode, 0,1M KCl, 40 mV s$^{-1}$*
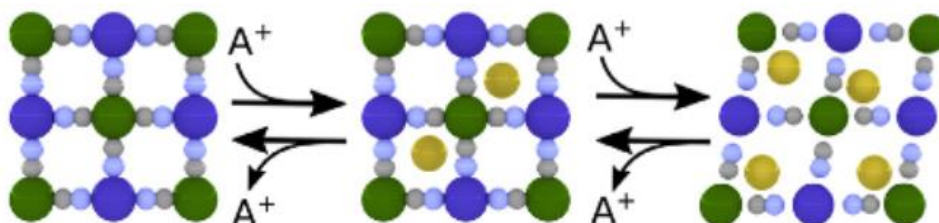
### 1.1.3 Metal Hexacyanoferrate

Prussian blue can be attributed to an extensive class of compounds which is called metal hexacyanoferrates with general formula $A_xB_y[M(CN)_6] \cdot nH2O$, where A is cation of alkali metal ($Li^+$/ $Na^+$/$K^+$), B and M are transition metal ions (Fe,Cu,Mn,Ti, etc) which are octahedrally coordinated to six cyanide ligands via the nitrogen and carbon atom, respectively. Under various modifications of structure such as replacing of one or both iron atoms on other metals, Prussian blue transforms to the series of so-called Prussian blue analogues (PBAs) compounds. These changes in the structure can happen without breaking existing crystal lattice but can lead to interesting modifications in properties, several of which are highly desirable in energy storage [20]. Use of PBAs as an electrode material can be explained by following advantages:

i.  Nanoporous, open-framework structure arising from cubic geometry and corresponding wide channels which leads to rapid ionic conduction for high rate capability. The structure of PBAs contains open <100> channels of 3.2 Å and interstitial sites of 4.6 Å in diameter. Presence of relatively large interstitial sites inside the structure allows to host water and alkali ions, whereas the wide channels among the interstitial sites gives opportunity for rapid transport of $Li^+,Na^+,K^+$ ions throughout the lattice [21, 22].

ii.  Lattice strain presented after electrochemical cycling is relatively small and can keep the structure stable because the size of interstitial sites are larger than size of extracted ions [22]. For example, the decrease in volume of the unit cell of MnHCF after lithiation is just 3.5% [22, 23] and the similar tendencies can be seen for other PBAs after insertion of different alkali ions [24]. This high degree of reversibility leads to extremely long cycles lives. Goodenough and coworkers demonstrated that synthesized $KM[Fe(CN)6]$ compounds (M = Fe, Cu, Mn, Ni and Zn) exhibited a reversible capacity near 100 mAh $g^{-1}$ with no capacity fade until 30 cycles [25]. Cui et al. showed that NiHCF electrode can be well cycled at high current density in inexpensive aqueous electrolytes, and this open-framework structure allows retention of 66% of the initial capacity even at a very high rate, whereas at low current densities, its round trip energy efficiency reaches 99% [26].

iii.  Presence of potentially two redox metal centers ($Mn^{2+/3+}$) in PBAs leads to double contribution of a 2 electron transfer capacity through reversible insertion/extraction reaction process. Moreover, substitution of one of the metal on another in PBAs (which can happen without significant damage to the existing crystal structure) can lead to mentionable improvement in capacity or cyclability. As was demonstrated by Xie et al., by simply replacing one metal center

with Ti, the new compound sodium titanium hexacyanoferrate (NTH) was synthesized which exhibits better electrochemical performance with both high capacity (92.3 mAh g$^{-1}$) and good cycling stability with two redox couples at 2.6/3.0 V and 3.2/3.4 V, corresponding to high-spin Ti$^{3+/4+}$ couple and low-spin [Fe(CN)$_6$]$^{4-/3-}$ couple, respectively [27].

iv.   Easiness in preparation and relatively low cost. Usual procedure for synthesis of PBAs is a simple and inexpensive coprecipitation reaction between aqueous precursors with good final yield.

The main disadvantage of Prussian Blue analogues materials is their low crystal density (1.96 g cm$^{-3}$for defect-free sodium iron hexacyanoferrate), which two times less that of high-performing lithium-ion cathodes. For this reason, PBA batteries are unlikely candidates for use in consumer electronics or electric vehicles [22, 28, 29]. Also, at a high concentration, the lattice cooperatively can be displaced in the <111> direction, transforming to rhombohedral geometry (Figure 4). This change in structure can lead to decrease in ionic conductivity and reversibility, lowering rate capability and cycle life, respectively. So, considerable attention should be done to the benefits of high capacity in lithium- and sodium-ion electrodes which must be accurately weighed against sacrificing to these other performance metrics [22].



*Figure 4. Insertion of alkali ions at critical concentrations can distort the structure to a less symmetric rhombohedral geometry* [22]

### 1.1.4 Manganese Hexacyanoferrate (MnHCF)

Manganese hexacyanoferrate is one of the promising cathode materials for sodium-ion batteries. Compared to other PBAs, MnHCF has several advantages: 1) it consist of only abundant metals, which leads to relatively low price for final battery; 2) it has a large reversible specific capacities (>120 mAh g−1) and high potentials for the storage of alkali ions ($K^+$, $Li^+$, $Na^+$) [30]. Takachi et al. reported the structural, electronic, and electrochemical properties of $Na_{1.32}Mn^{II}[Fe^{II}(CN)_6]_{0.833}*5H_2O$ thin film electrodes with observed discharge capacity of 135 mAh/g which attributed to the $Mn^{3+}/Mn^{2+}$ reduction at 3.7 V and the $Fe^{3+}/Fe^{2+}$ reduction at 3.3 V [31]. The drawback of synthesized compound is well-known Jahn–Teller effect presenting in all trivalent Mn-based materials which lead to instability of $Mn^{3+}$ ion hindering the manganese reduction reaction at a high rate [32].

Generally, three possible structures of $Na_xMn[Fe(CN)_6]$ exist: rhombohedral, monoclinic and cubic. The first two showed poor cycling stability because of the multiple phase transitions and structural changes during Na+ insertion/extraction. For instance, J. B. Goodenough and reported that rhombohedral $Na_xMnFe(CN)_6$ revealed rapid capacity fading as a result of a phase transition from rhombohedral to cubic during the uptake and removal of Na+ ions. Turning to monoclinic $Na_{1.89}Mn[Fe(CN)_6]_{0.97} \cdot 1.87H_2O$, it goes through complicated series of phase conversion (monoclinic - cubic - tetragonal ) during initial charging process [33, 34, 35]. These structural changes lead to poor cycling stability and low initial coulombic efficiency. Oppositely, unlike rhombohedral and monoclinic phases, cubic sodium manganese hexacyanoferrate exhibits highly structural symmetry, which should lead to higher stability in structure during sodium insertion/extraction processes. However, so far the cubic $Na_xMnFe(CN)_6$ is rarely used as cathode material for sodium-ion batteries because cooperative sodium displacement along a [111] axes at higher sodium concentration modify the crystal symmetry to distorted rhombohedral or monoclinic phase [35]. Y, Tang and coworkers found that cubic and monoclinic structured $Na_xMnFe(CN)_6$ synthesized with addition of citric acid show completely different cyclic stability. It was reported that cubic structured $Na_xMnFe(CN)_6$ can remain the cubic phase during the whole Na+ insertion/extraction process, whereas monoclinic structured $Na_xMnFe(CN)_6$ goes through undesirable changes during the whole cycle leading to mentionable lattice distortions and mechanical stress. As a result, cubic structured manganese hexacyanoferrate reveal a high capacity of ≈120 mAh $g^{-1}$ and excellent cycling stability of ≈70% capacity retention over 500 cycles at 200 mA $g^{-1}$, compared to that of monoclinic structured with only 38% capacity retention [36].

Recently, a lot of studies have been focused on improving the performance of MnHCF and other PBAs as a cathode material [37] :

i.    Optimization of the crystallization processes by opening novel synthetic methods because most of the Prussian blue compounds obtained from the conventional synthetic routes contain large amounts of Fe(CN)6 vacancies and coordinated water molecules, which leads to the collapse of cyano-bridged framework and serious deterioration of their Na-storage ability [38]. Qian et al. proposed synthesis of vacancy-free $Na_2CoFe(CN)_6$ with superior cyclability by a controlled crystallization reaction using sodium citrate as the chelating agent [39], whereas Guo et al. reported about low defect Prussian blue crystals with superior electrochemical performance by a single iron-source method [38].

ii.   Changing in the composition and framework structure to get better performance characteristics. Y. Morimoto and coworkers investigated how the partial substitution of Mn on Fe, Co, and Ni in Mn-HCF influence on the SIB rate and cycle performance: at 50C noticeable discharge capacity was still observable for substituted samples, whereas it completely disappeared already at 20C for initial compound. This improvement was attributed to the partial suppression of the Jahn-Teller distortion of $Mn^{3+}$ and the subsequent activation of the Mn reduction reaction [40].

iii.  Preparation of high sodium content materials by reacting in Na-rich environment. As was demonstrated by W.J. Li et al [36], Na-rich PBAs shows a higher specific capacity of more than 100 mAh $g^{-1}$ and excellent capacity retention of 97% over 400 cycles compared to Na-poor analogues.

iv.   Improvement of electrochemical performance by modification of surface of particle by conductive materials. By introducing polypyrrole coating, sodium iron hexacyanoferrate exhibits improved cycling stability with 79% capacity retention over 500 cycles at 200 mA $g^{-1}$. These effects can be related to polypyrrole which is playing a role of both an electronic conductor to enhance the conductivity and a protective layer to prevent the side reactions [41].

**8**

### 1.1.5 Sodium-ion batteries (SIBs)

Possessing obvious benefits as a high natural abundance of sodium resource (the fourth most abundant element on Earth) and similar intercalation chemistry as lithium-ion batteries, sodium-ion batteries can significantly decrease the batteries' price and make them one of the most promising alternatives to LIB [42]. The first study on SIB are going back to the beginning of 1980 [43], but after the huge success of lithium-ion batteries commercialization in 1991 the whole world attention was taken to LIB rather than to SIB [44].

In 2000, Stevens and Dahe reported that hard carbon shows a reversible sodium-ion storage capacity of about 300 mAh·g$^{-1}$, which is comparable to graphitic carbon for lithium ion storage [45]. This research and already existing challenges with LIB such as lithium metal shortage and increased price, led to a resurgence in the field of sodium-ion batteries. Starting from 2010, a large amount of novel electrode materials such as Prussian blue, NASICON, olivine and oxides [46, 47] started to be reported.

Because of the open zeolite-like structure, compositional and electrochemical tenability, Prussian blue analogs treated as an attractive cathode material for sodium-ion batteries. But difficulties in water control in synthetic part and the potential toxicity from cyanide release restrict their applications [46]. NASICON compounds, such as $Na_3V_2(PO_4)_3$ and $Na_3V_2(PO_4)_2F_3$, were also used as electrodes for sodium-ion batteries. Having good characteristics (capacity of ∼100 mAh/g, excellent rate capacity and cycle stability [47]) both $Na_3V_2(PO_4)_3$ and $Na_3V_2(PO_4)_2F_3$ showed promising Na storage performance, but the probability of liberation of fluorine gas as well as toxic $V^{3+}/V^{5+}$ ions limit the large-scale manufacture [48]. Using of olivines such as $NaFePO_4$ can be complicated by the difficulties in synthesis procedure which inevitably leads to the increase in cost of production [49]. Following the success of layered-$LiCoO_2$ in LIB [50], sodium analogues $Na_xMO_2$ (M: Ni, Mn, Co, Ti), which also have layered or tunneled structures based on Na content, were investigated. For example, tunnel-type $Na_{0.44}MnO_2$ reported by Doeff et al. exhibit a unique structure limiting the interaction with $H_3O^+$, which is useful as a cathode or anode for non-aqueous and aqueous SIB [51]. Turning to metal-oxides ($Fe_2O_3$, $Sb_2O_4$ and $MnO_2$), they demonstrate good capacity of 200 mAh/g, but the conversion reaction involved in charge transfer may result in low initial coulombic efficiency and electrode instability [52].

The main problems with SIB still remain low reversible capacity and poor cyclability which are consequence of large volume changes and irreversible phase transitions during intercalation and deintercalation of sodium ions (1.02 Å) [53].

**1.2 Characterization techniques**

**1.2.1 Synchrotron radiation**

A synchrotron is a very bright, broadband, polarized, pulsed source of light that scientists can use to get the information about the structural and chemical properties of versatile materials at the molecular level [54]. It produces light by using radio frequency waves and powerful electro-magnets to accelerate electrons to nearly the speed of light. Energy is added to the electrons during the acceleration, so when the magnets change their direction, they naturally emit a very brilliant, highly focused light. The energy spectrum of this radiation is white, covering the infrared to the hard X-ray regions. When this light is directed down particular beam line, researchers choose the desired wavelength to study their samples [55].

There are three main parts of any synchrotron facility: linear accelerator (LINAC), booster and storage ring. The electron gun begins the process by running high voltage electricity through a heated cathode which produces pulses of electrons that enter the LINAC. This is done by using a tungsten-oxide disk as the cathode material. When the electricity flows through the cathode, it heats (at about 1000°C) to incandescence which provides enough energy for some electrons to leave the surface of the cathode. Then, a nearby screen is given a short, strong positive charge (125 times per second) which pulls the electrons away from the cathode towards the LINAC. The LINAC is a series radio frequency cavities which accelerate the electrons to energy of 250 MeV. After that, electrons directed to the booster ring where they raise the energy up to 2900 MeV and transferred to the storage ring. In electron storage rings there are three possible sources of synchrotron radiation: dipole (bending) magnets; wigglers, which act like a sequence of bending magnets with alternating polarities; and undulators, which are also multiperiod alternating magnet systems but in which the beam deflections are small, resulting in coherent interference of the emitted light. Once the electrons are in the Storage Ring, they circulate for 4 to 12 hours producing photons every time when the direction of electrons flow is changed by the dipole magnets [56].

Synchrotron radiation has the unique potential as a valuable research tool because it possess some distinctive advantages: (1) it has a broad, smooth, spectrum extending from the infrared (IR), through the visible and ultra- violet (UV) and, depending on the energy of the electrons and the dipole field of the source, into the X-ray region; (2) it is highly collimated in the vertical plane, and provides X-ray intensities that are $10^{10}$ orders of magnitude greater than those available from conventional sources; (3) the radiation is linearly polarized in the plane of the accelerator, with elliptical polarization off axis; and (4) the radiation has a high frequency time structure imposed by the radio frequency accelerating voltage in the accelerator; in some circumstances, short pulses at lower frequencies can be

generated, permitting unique opportunities for time resolved research [57]. All this makes synchrotron radiation rather extraordinary source for a wide variety of science and technological experiments.

### 1.2.2 Synchrotron based X-Ray techniques

Since 1970s, when synchrotron radiation became widely available, the special attention was directed to the X-Rays techniques which applications were restricted at that moment. Synchrotron radiation became the most intense source of X-rays and possesses a large number of advantages compared to conventional sources which eventually makes it irreplaceable source for different X-ray spectroscopic techniques in the next decades.

One of the most interesting applications is to use SR and especially synchrotron based X-ray techniques for study of batteries materials. Deep understanding of different aspects of sodium-ion batteries, such as charge storage and performance degradation mechanisms, reactions at the electrode/electrolyte interfaces and cycling stability, are critically important. The synchrotron-based X-ray techniques provide powerful methods for studying and monitoring the changes of crystal and electronic structure, chemical composition and morphology of electrode materials in electrochemical cells during its operation. The results can help to improve the performance of existing systems and to design new battery materials. During the last years, developments in synchrotron-based X-ray techniques have provided significant opportunities to study the mechanisms of battery materials performances. Combined with other techniques such as scattering, spectroscopy, and imaging, extensive studies have been performed to understand the problems arised during batteries work. Synchrotron-based X-ray techniques and the information that obtained by each method are summarized in Figure 6 [58, 59]. Moreover, synchrotron X-ray sources allow performing in situ/operando experiments with various techniques to investigate dynamic properties and time-dependent reaction process. The benefits of in situ/operando approaches over ex situ characterization are following:

(1) in situ measurements directly study the proceeding reaction, guaranteeing better reliability and higher precision for the data analysis;

(2) in operando measurements incessantly monitor electrochemical, physical, or chemical processes on a single sample under operating conditions, providing more real-time operation information;

(3) it allows the study of the non-equilibrium or fast-transient process during electrochemical chemical reactions. The short-lived intermediate states or species, which cannot be detected by ex situ characterizations, can be identified.

(4) In situ methods decrease the probability of contamination, irreversible changes of highly reactive charged/discharged samples during preparation and transferring them for ex situ

**11**

measurements and the true reaction products can be more reliably identified. The last results from advanced in situ/operando synchrotron-based experiments help to obtain deeper insight into the complicated reaction mechanisms in batteries material [58]. However, it should be considered that not all the experiments can be suitable for operando data acquisition. Also the electrode preparation and characteristics may vary respect to the normal operating parameters (such as mass loading and sample geometry).
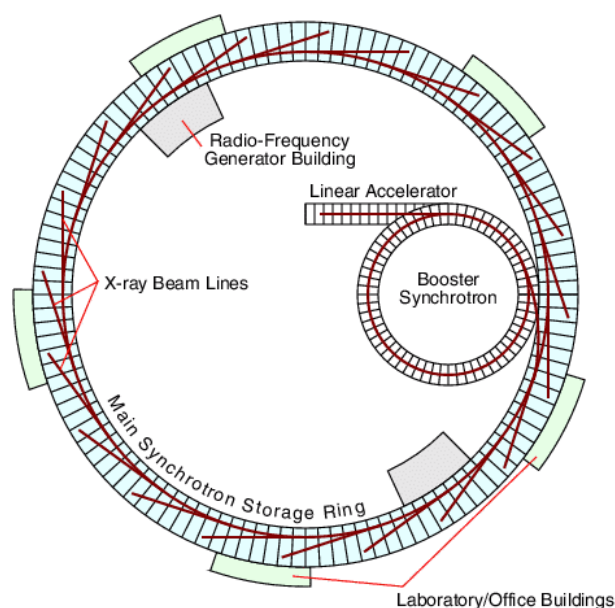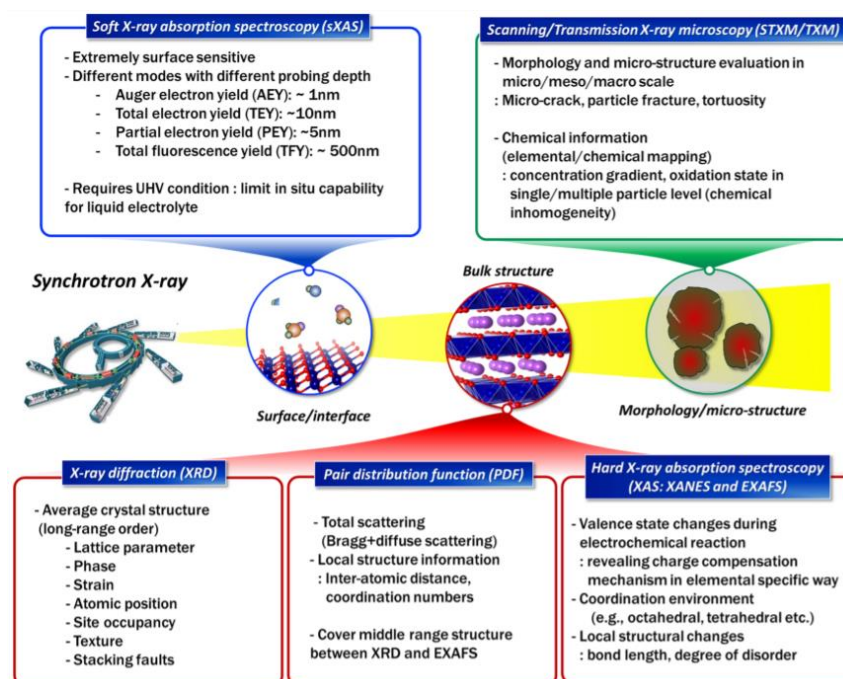


*Figure 5.Synchrotron construction* [60]



*Figure 6.Synchrotron-based X-ray techniques*

### 1.2.3 X-Ray absorption spectroscopy (XAS)

X-Ray absorption spectroscopy (XAS) is a powerful technique for determination of the local geometry and electronic structure of matter. It has several distinctive advantages:

a) XAS can be used for crystals as well as for materials with little or no long-range translational order (which makes it different from XRD);

b) it is element selective that allows to probe the local structure around the selected element within a material concentrating on its K (or L) absorption edge;

c) the physicochemical information contained in the near-edge structure of the XAS signals can be used to reveal the formal oxidation state and the local symmetry of the probed atom;

d) the possibility of doing operando/in-situ measurements by collecting XAS spectra during electrochemical cycling using specifically developed in situ cells;

e) analyses of elements at low concentrations are possible. Concentrations of~500 ppm and about 0.5 wt% of a particular element can be analyzed using the fluorescence and transmission modes, respectively.

On the other hand, XAS possesses several disadvantages:

a) when sample is consist of several different phases containing the same element, an observed XASS spectrum will be an average of spectra from the different phases. Therefore, it is difficult to identify materials from a mixture of phases;

b) in order to get the information about the local structure, a complex procedure for spectral analysis has to be done;

c) structural information in three dimensions and long-distance ordering cannot be obtained from XAFS, unlike X-ray crystal structural analysis using XRD.

At that point considering all aforesaid, XAS can be considered as an interesting characterization tool to be used in the field of batteries. Indeed, for instance, to retrieve structural and electronic information for materials which are not crystalline and, thus, cannot be investigated by diffraction techniques, XAS can be extremely useful. Or, in case of XAS operando measurements, properties and the local structure of the studied element can be monitored at any specific moments during the charge and discharge processes. The primary use of XAS technique in the study of batteries was reported by Mc. Breen et al. in the late 80s [61]. Nowadays, more and more reviews were published describing the inevitable advances of XAS application in batteries research field [62, 63, 64, 65].

XAS (or XAFS) is generally divided in two regions: X-ray absorption near edge spectroscopy (XANES), which is restricted by 80–100 eV above the edge, and a post-edge region extended X-ray absorption fine structure (EXAFS), which is covered up to 1000 eV above the absorption edge

(Figure 7). The difference in between XANES and EXAFS is that the last one can be interpreted in a more quantitative way as a result of some important approximations in the theory («one electron», «sudden» approximation etc). On the other hand, the XANES region, consisting from the pre-edge and the absorption edge itself, can be used to determine the oxidation state and coordination chemistry of the absorbing atom. The EXAFS region has been mainly used to get quantitative structural information such as first shells' distance of the metal site and the coordination number. It consists of periodic oscillations that decay in intensity as the incident energy increases well above the absorption edge. These undulations arise from the scattering of the emitted photoelectron with the surrounding atoms.
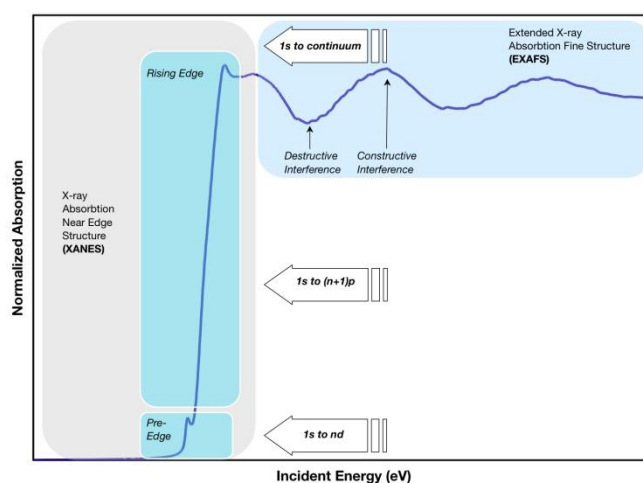


*Figure 7. XANES and EXAFS regions in XAS spectrum*

XAS is one of the most well-known and simplest techniques to investigate the structural end electronic modification of a cathode or anode material. At a certain state of battery's charge, XAFS spectra are collected at a selected edge. Two different geometries can be used for this purpose: transmission and fluorescence. In the first mode, the sample is placed between detectors and the absorption is measured followed the Beer's law exponential decay. On the other hand, the fluorescence detection is proceeded by tilting the specimen at angle of 45 degree and collecting the fluorescence X-rays by means of solid-state detector at the certain angle related to $I_0$. Apart from such an ex situ XAS measurements, operando XAS appeared recently and complement the studies of electrode material. Use of this method allows avoiding several distinctive disadvantages of ex situ experiments due to the need of transferring the sample. For instance, change of samples' structure which are sensitive to air and moisture  as well as the relaxation reactions which might occur when the electrical circuit is open, leading to a transformation of the unstable cycled material, can be escaped. Because the sample stay in the same position during the measurements, the effects related to sampling deviations can also be avoided.

Finally, the whole experiment can be carried out using single test cell suppressing the consequences of uncontrolled differences in a set of cells which are used for a stepwise ex situ study of the electrochemical mechanism. For this an experiment, a special in situ electrochemical cell, with respect to the specific requirements of XAS, has to be used. This cell include an electrode containing the active material, a lithium foil, a separator, which is typically a polymeric membrane such as Celgard, and an electrolyte, usually based on organic carbonate solvents such as propylene carbonate (PC), dimethyl carbonate (DMC) and ethylene carbonate (EC) [66]. Generally, two types of electrochemical cell are used for in situ experiments: pouch cell and stainless steel cell as shown in figure [61]. The former has a film containing the active material which is deposited on a square Al (or Cu) current collector and assembled in a glove box together with a Li (Na) counter-electrode, a separator and the electrolyte; the latter uses self-supported films or pellets of electrode material of smaller dimension which is successfully employed in both transmission and fluorescence geometry, as well as in other techniques including *in situ* XRD [61], Mossbauer [62] and Raman spectroscopy [63] measurements.
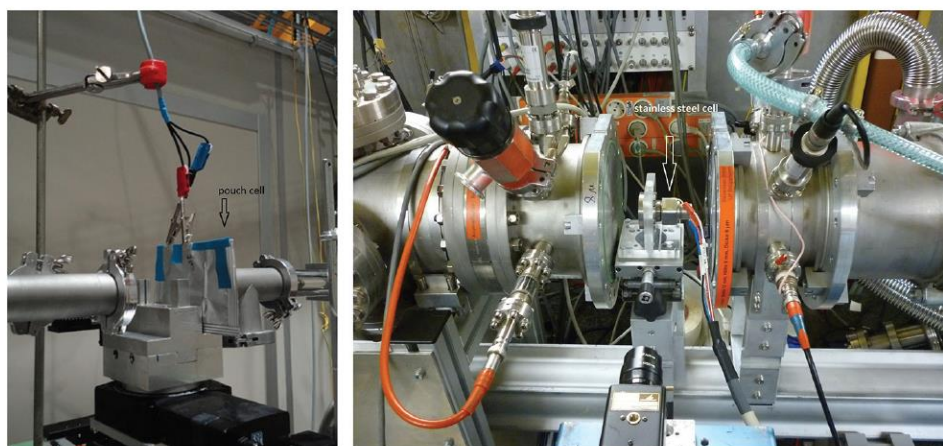


*Figure 8.Two types of in-situ electrochemical cells: a) pouch cell (left) and b) a stainless steel cell (right) mounted on different XAS beam lines* [61]

### 1.2.4 Analyses of XANES

As was mentioned above, XANES consist of strong oscillations observed within the region of 80 eV (including pre-edge). At this part of the spectra, a photoelectron perceives strong perturbations from surrounding atoms as a result of interactions between the direct and the multi scattering wave. Because the multi-scattering wave depends on both atomic distance and the coordination geometry of surrounding atoms, XANES is very sensitive to these structural factors. Theoretically, it can lead to possibility of extracting three dimensional structure information from XANES spectra, but these theoretical simulations are still remain extremely difficult. Despite the fact that much progress has recently been done in the theoretical modeling, most of the applications of XANES still remain qualitative [67].

XANES can be related to the process of excitation of an inner shell electron to a vacant level across to the Fermi level. On the low energy side of the absorption edge several weak transitions can usually be observed arising from bound state transitions such as 1s-3d and 1s-4p transitions which can help us to determine the corresponding structure of material (tetrahedral or octahedral coordination).At the same time, shift of the edge position can indicate the changes in the valence state. This technique is already applied to discern coordination and oxidation states of metals in compounds and complexes Decomposition of the spectral components can differentiate between different site symmetries and assist in quantifying oxidation state [68]. As shown, for example, in figure 9, corresponding pre-edge peak increases its intensity reflecting the decrease in the symmetry and increases in the vacancy of 3d orbits (Ni<FeO<$ZnFe_2O_4$). The splitting in the pre-edge peak of FeO and $ZnFe_2O_4$ is attributed to the crystal field splitting of d-orbitals ($t_{2g}$, $e_g$) [69, 70, 67].
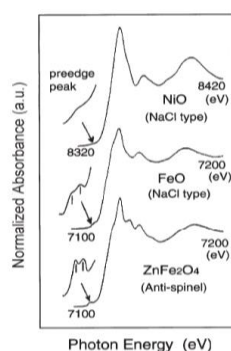


*Figure 9.XANES spectra of NiO, FeO and ZnFe2O4* [67]

XANES is a much larger signal than EXAFS and can be obtained at lower concentrations and less than perfect sample conditions. However, because of absence of simple analytical equation, it is considerably harder to fully interpret and usually is described qualitatively (and nearly quantitatively) in terms of coordination chemistry, molecular orbitals, band-structure and multiple-scattering [71].

**1.2.5 Analyses of EXAFS**

The EXAFS process can be interpreted as in situ electron diffraction, where the X-ray absorbing atom is the photoelectron source [71]. When $E_k$ of the ejected photoelectron is sufficient to allow it to escape the bound state, it will interact with other electrons in the bound states of other atoms within the local chemical environment surrounding the absorber. These interactions lead to the series of constructive and destructive interferences between outgoing scattering and incoming backscattering waves resulting in low frequency oscillations between ~50 and ~1000 eV above the absorption edge. These oscillations constitute EXAFS and contain important structural and chemical information specific to the particular scattering atomic shells representing a group of atoms of the same species at the same distance from the absorbing atom. Qualitatively, the EXAFS oscillations are of higher frequency for long interatomic distances between the backscattering elements and the absorber, and of lower frequency for shorter interatomic distances. Quantitatively, the amplitudes of EXAFS oscillations can identify the type and number of backscattering atoms as well as the distribution of these atoms about a mean distance from the absorbing atom. The higher energy portions of EXAFS spectra are dominated by single scattering events within only some tenths of nm (5-6 Å) from the absorber, and contain information specific to the local structure surrounding the absorber [71, 72].

The observed EXAFS oscillations ($\chi(k)$,) can be described by following equation:

$$\chi(k) = \sum_i \frac{\left(N_i S_0^2\right) F_i(k)}{kR_i^2} \sin\left[2kR_i + \delta_i(k)\right] e^{-2\sigma_i^2 k^2} e^{-\frac{2R_i}{\lambda(k)}}$$

It can be divided by 2 parts: the first one is the amplitude $A_j(k)$ contains information about coordination number (N) and disorder ($\sigma$) ; the second part is the phase shift representing by the sine function and depends on the shell distances. Two limitation of EXAFS equation can be mentioned: a) Debye–Waller factor which is responsible for the thermal effects and structure disorder leading to the damping of the fine structure signal, since the structure disorder generally increases with the distance R, b) EXAFS signal is inversely proportional to the square of the distance R so usually it is limited up to 5-6 A [73]. Although EXAFS equation gives a complete description of the EXAFS oscillations, it can be not convenient to visualize the information content of an EXAFS spectrum. For that purpose, Fourier transformation can be used to resolve the data into individual waves corresponding to the different types of neighbors (SS) and bonding configurations (MS) around the absorbing atom [71]:

$$FT(R) = \frac{1}{\sqrt{2\pi}} \int_{k_{min}}^{k_{max}} k^n \, \chi(k) e^{i2kR} \, dk$$

The FT is a useful approach for qualitative analysis of EXAFS, because it shows which shells may be present in a system and allow compare the obtained fit to the theoretical data. However, it should be noted that several potential problems can arise from FT. For example, in some cases, multiple shells of scatterers cannot give rise to multiple peaks; also, interference between two different peaks in the FT may give rise to a false third peak. The latter arises from the fact that the FT of an EXAFS spectrum is a complex number consisting from both real and imaginary components, but only the modulus of the FT is plotted [74].

In order to extract the distances and coordination numbers from the experimental EXAFS data, accurate values for the scattering amplitude and phase-shifts are needed. In the first EXAFS analyses, they could only be calculated from experimental spectra where the near-neighbor distances and species were known precisely. Nowadays, determinations of f(k) and δ(k) have become more accurate using the programs FEFF, GNXAS, and EXCURVE . The calculated factors are not restricted to the first shell and can account for multiple-scattering of the photo-electron. The general approach for determining the average coordination structure around the absorber atom from EXAFS data is to generate a theoretical model for the sample and calculate the theoretical EXAFS spectrum for that model using a computer program like FEFF or Artemis. With the help of these programs, the structural parameters in the EXAFS equation can be adjusted until a least-squares fit is obtained between the theoretical (modeled) and experimental EXAFS spectra [71]. In practice, some of the parameters in the EXAFS equation are calculated ab initio, while others are found by fitting the model to experiment. For example, the effective scattering phases and amplitudes are generally calculated, while a variety of other parameters are used as fitting variables. The standard procedures used for preprocessing of data, and the extraction of structural parameters by fitting to the EXAFS equation can be described as follows [75]. First the oscillatory fine structure $\chi$ (k) is extracted from the data by subtracting a smooth background function. After that, it should be normalized, and then Fourier transformed to real (R) space which gives amplitude that is akin to a radial distribution function, with contributions from longer scattering paths peaking at higher R value. Obtained value then should be corrected using fitted parameters for higher precision.

### 1.2.6 X-ray diffraction

Synchrotron radiation X-ray powder diffraction (SR-XRPD) is a powerful characterization technique that uses the interaction between synchrotron X-rays radiation and matter to study the microstructures of materials. Generally, from XRD data, it is possible to accurately acquire different information such as (i) phase compositions and phase abundances, (ii) Bravais lattice symmetry and lattice parameters, (iii) residual strain (macrostrain), (iv) crystal structure, (v) crystallite size and microstrain, and (vi) evolutions of all aforementioned properties as a function of pressure, time, temperature, gas environment [59]. To extract all this structural information from XRD data, Rietveld refinement software (e.g. GSAS, FullProf etc) are often used. By using synchrotron radiation light X-ray diffraction patterns with a high S/N ratio can be obtained. Weak diffraction peaks, which could barely be observed before using conventional X-ray source, appear as a distinct peak. Good crystal structure refinement using the Rietveld method is possible, because the absorption and preferential orientation are negligible, and the superior dynamic range of the imaging plate guarantee that we can observe high-quality diffraction peaks.

In situ or in operando XRD measurements have been widely utilized to study changes in structure in battery materials during electrochemical processes using synchrotron light sources. For example, $LiFePO_4$, cathode material that is used in some commercial batteries, has two-phase reaction mechanism occuring during charge which has been verified by means of in situ and ex situ XRD studies. Plenty of studies have been carried out to reveal the mechanism of intercalation reaction in $LiFePO_4$ at the microscopic scale. Delmas and al. proposed the "domino-cascade" model based on analyses of ex situ XRD data collected at different states of charge (SOCs). They found that the coherent domain length of both $LiFePO_4$ and $FePO_4$ did not change significantly during the entire delithiation process and concluded that the lithium intercalation/deintercalation process proceeded through a $LiFePO_4/FePO_4$ two-phase reaction at a very high rate [76].

### 1.2.7 Transmission soft X-ray microscopy

Energy - dependent full - field transmission soft X - ray microscopy is a useful technique which provides chemical information with good spatial resolution. This spectromicroscopical method based on synchrotron radiation can give a full picture of the oxidation state and spatial distribution in the cathode materials at the nanometer scale. By using X-rays of the "soft" energy region (<3 KeV), it is possible to access transitions from core levels of light elements, among them the K-edge of nitrogen, oxygen, fluorine, as well as L – and M - edges of other elements.

There are two types of lens-based microscope geometries used at synchrotron radiation sources: the full-field transmission X-ray microscope (TXM) and the scanning transmission X-ray microscope (STXM), as shown in figure 10. Both of them are lens microscopes based on the application of Fresnel Zone Plate diffractive lenses (ZP) that work like a circular diffraction grating whose period radially going down from the center in a way that all the waves with the same diffracted order directed to the same point. For the TXM the typical scheme of a common visible light microscope is used: a sample is placed at the focal plane of two lenses, where he first lens, usually called "condenser", focalizes the beam on to the sample plane, while the second lens, called "objective lens", produces a full magnified image of the sample on to the detector plane.

The main difference between STXM and TXM system lies in the radiation dose: when the lens is before the sample, then all the photons emerging from the sample are used to produce the image. Oppositely, in a TXM system, the ZP is after the sample, leading to the point that most of the photons arising from the sample will not contribute to the formation of the image. Therefore to get the same image quality as a STXM, the TXM will need to absorb higher radiation dose. On the other hand, the main advantage of the TXM over the STXM system is the exposure time: in one "snapshot" the full image of the sample can be obtained.
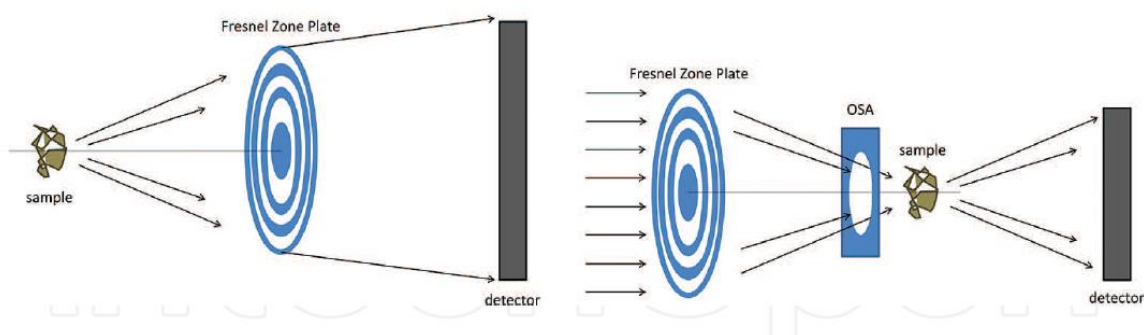


*Figure 10.Scheme of the two common transmission X-ray microscopes: (a) Full-field microscope; (b) Scanning microscope*

In a transmission soft X-ray microscopy, the contrast of the obtained picture depends on several factors: sample thickness, elements from which it is consist of, their density, and the energy and polarization of the incident radiation. Parts of the images can become darker (or brighter if we use the absorbance) when the radiation is triggering some allowed electronic transitions. It is also possible to detect chemical states of the same element because the exact energy is also dependent on the atom environment. All this chemical information is available with spatial resolution down to few tens of nanometers by using in a synchrotron-based transmission X-ray microscopy. An example of a state-of-the-art soft X-ray full-field transmission microscope is the one installed at the Mistral beamline in ALBA synchrotron. A part of the experimental part of the beamline is represented in Figure 11.



*Figure 11. TXM at the MISTRAL beamline*

### 1.2.8 Cyclic Voltammetry

Cyclic Voltammetry (CV) is an electrochemical technique which measures the current that develops in an electrochemical cell under conditions where voltage is in excess of that predicted by the Nernst equation. CV is performed by cycling the potential of a working electrode, and measuring the resulting current [77, 78]. A potentiostat is used to linearly sweep the potential between the working and reference electrodes until it reaches a preset limit, and then swept back in the opposite direction, switching the potentials. It is repeated multiple times during a scan and the changing current between the working and counter probes is measured in real time. The resulting 'duck-shaped' plot is called a cyclic voltammogram, illustrated in figure 12 [79]. At some point after the reduction potential of the analyte is reached, the cathodic current will decrease as the concentration of reducible analyte is depleted. If the redox couple is reversible then during the reverse scan, the reduced analyte will start to be re-oxidized, giving rise to a current of reverse polarity (anodic current) to before. The more reversible the redox couple is, the more similar the oxidation peak will be in shape to the reduction peak. Hence, CV data can provide information about redox potentials and electrochemical reaction rates. If the electron transfer at the working electrode surface is fast and the current is limited by the diffusion of analyte species to the electrode surface, then the peak current will be proportional to the square root of the scan rate. This relationship is described by the Randles–Sevcik equation. In this situation, the CV experiment only samples a small portion of the solution, i.e., the diffusion layer at the electrode surface [80, 81].
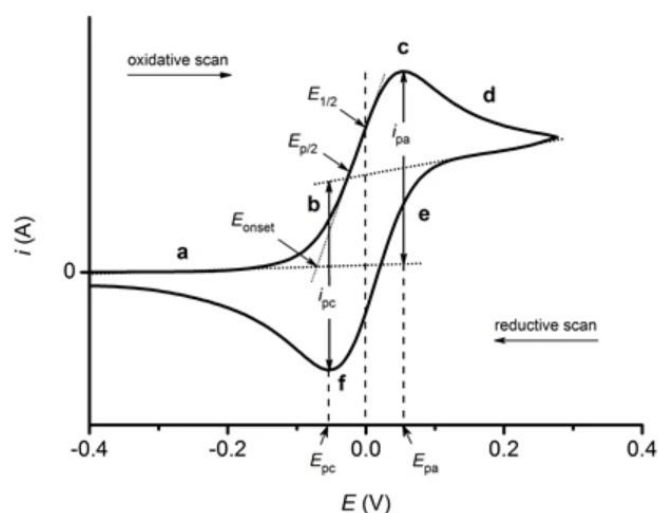


*Figure 12. Cyclic voltammogram for an electrochemically-reversible one-electron redox process.*

A CV system consists of the following parts: an electrolysis cell, a potentiostat, a current-to-voltage converter, and a data acquisition system. The electrolysis cell itself includes working electrode, counter electrode, reference electrode, and electrolytic solution (Figure 13 [82]). The working electrode's potential is changed linearly with time, while the reference electrode maintains a constant potential. The counter electrode conducts electricity from the signal source to the working electrode. The purpose of the electrolytic solution is to provide ions to the electrodes during oxidation and reduction and therefore to guarantee the ionic conductivity of the solution [83].

Cyclic voltammetry (CV) is a powerful and widely used electroanalytical technique in different parts of chemistry. It is often used to study a variety of redox processes, to determine the stability of reaction products, the presence of intermediates in redox reactions, [84] electron transfer kinetics [85], and the reversibility of a reaction [86]. CV can also be used to calculate the electron stoichiometry of a system, as well as diffusion coefficient of an analyte, and the formal reduction potential of an analyte. In addition, because concentration is proportional to current in a reversible, Nernstian system, the concentration of an unknown solution can be determined by generating a calibration curve of current vs. concentration [87].
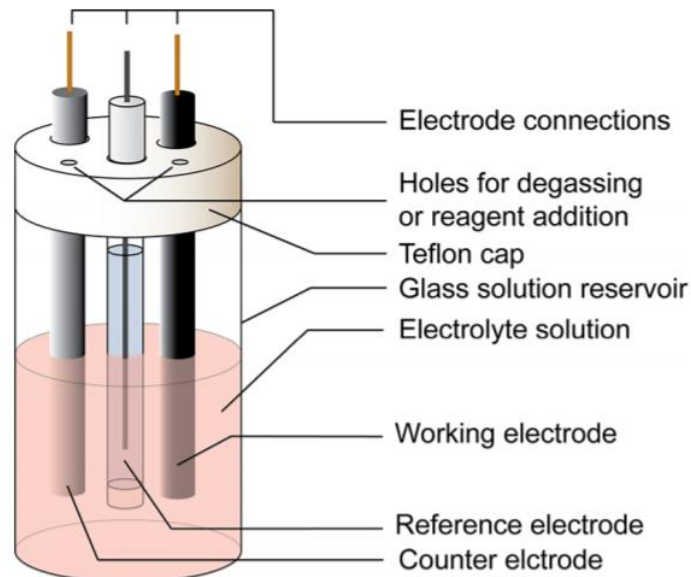


*Figure 13. Schematic representation for electrochemical cell*

**1.2.9 Electrochemical impedance spectroscopy (EIS)**

Electrochemical impedance spectroscopy, which is also called AC impedance or just impedance spectroscopy, is a multifrequency AC electrochemical measurement technique which is following the electrical resistance (impedance) of the metal/solution interface over a wide range of frequencies (from 1 MHz to 10 kHz). The results from EIS give possibility for determination of the polarization resistance (low-frequency region), the solution resistance (high-frequency region), and capacitance of double layer. EIS analysis offers mechanistic and kinetic information on a wide range of materials, such as batteries, fuel cells, corrosion inhibitors, etc. Theoretically, impedance measurements can be used to check any intrinsic property that has impact on the conductivity of a particle's solution interface [88].

The EIS concept proposed that the intricate electrochemical behavior of an electrode in electrochemical reaction is dependent on the several factors such as: ohmic resistance of the electrolyte between the working and reference electrode, the double capacitance resistance (DR) resulting from surface buildup of water molecules, adsorbed ions and organic molecules, charge transfer resistance or polarization resistance (PR) emanating from anodic and cathodic electrochemical reactions, Warbug factor and the adsorption of reactant and product on the electrode surface. The overall electrochemical behavior of an electrode can be described as an equivalent circuit comprising resistance, inductance, and capacitance. Instead of direct current (DC), alternating current (AC) is used in EIS to promote electrochemical reactions on working electrode. EIS test is usually performed using AC impedance analyzer, the electrochemical cell, and computer to acquire the data over a period of time. The principal method of EIS is the application of a spectrum of small-amplitude sinusoidal AC voltage excitations to the system, with the system's response to this perturbation from equilibrium measured in terms of the amplitude and phase of the resultant current. The frequency of the AC signal is changed, and the overall impedance of the cell is recorded as a function of frequency. The impedance is represented as a complex quantity Z comprising of real ($Z_{im}=R$) and imaginary {$Z_{im}=\omega-c$} parts. The result is represented graphically using two types of plot: a plot of imaginary vs. real impedance at different frequencies, so called the Nyquist plot (complex plane plot), and absolute impedance vs. frequency, or the Bode plot. The more depressed the semicircle in the Nyquist plot, the lower the electron transfer resistance behavior of the analyte; and the higher the electron transfer resistance, the less depressed the semicircle. The Bode plot shows the same data as the Nyquist but illustrates more clearly the dependence of impedance on frequency [89].

### 1.2.10 Thermogravimetric analysis

Thermogravimetric analysis is a technique in which the mass of a substance is monitored as a function of temperature or time when the sample is subjected to a controlled temperature program in a controlled atmosphere [90]. TGA instrument consist of a radiant heating chamber, temperature controller, precision balance, gas feeding system, and data analyzer (as shown in Figure 14 [91]).
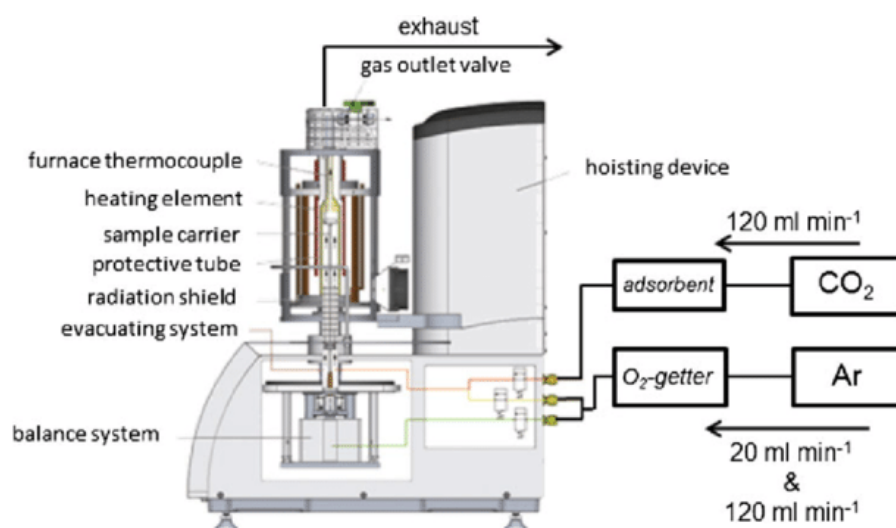


Figure 14. Schematic representation of TGA experimental set-up

A crystalline or powder sample is placed in a platinum basket and the temperature is continuously recorded by a thermocouple. Generally, two plots can be obtained as a result of TGA analysis: plot of sample's weight against temperature (TGA curve) providing thermal decomposition temperatures with residue amount as a function of temperature, and plot based on the derivative of the TGA curve, indicates mass loss rate depending on the increase of temperature [92]. TGA analysis can be used to calculate loss of water, solvent or plasticizer, decarboxylation, pyrolysis, oxidation, decomposition, weight % filler, amount of metallic catalytic residue remaining on carbon nanotubes, and weight % ash. All these quantifiable applications are usually carried out upon heating, but there are some experiments where information may be obtained upon cooling. It can also be used to evaluate the thermal stability of a material. In a certain temperature range, if a species is thermally stable, no observed mass change will be detected. Small mass loss corresponds to little or no slope in the TGA trace. TGA also gives the upper use temperature of a material, beyond which the material will begin to degrade [90].

## 1.2.11 FTIR

Fourier Transform Infrared Spectroscopy (FTIR) is a spectroscopic technique that uses low energy radiation to induce vibrational and rotational excitation of atoms and groups of atoms within molecules [93]. Because of the variety of symmetry of atomic groups and their differences in atomic masses and electronic structure, the absorption patterns for a specific species are unique, allowing to easily identify them. When photons interact with a molecule, the molecule may respond by absorbing the photons and subsequently the energy of the absorbed photons cause the molecule to vibrate in a higher energy level. Absorption occurs when the incoming IR radiation that is interacting with a molecule has sufficient energy to raise the vibrational energy level of the molecular system to the next allowed level. The frequencies of absorption are determined by the masses of atoms, the force constant of bonds, and the geometrical shapes of the molecule. Absorption of the mid-IR (4000- 400 cm-1) region is due to combination of interacting vibrational modes, which allows for unique fingerprinting of molecular species [94].

FTIR spectrometers evolved from dispersive IR instrumentation and have several distinct advantages. Firstly, FTIR utilizes Mickelson interferometer (Figure 15 [95]) instead of a monochromator which allows to make the scanning and the spectral collection process faster and more precise. Secondly, by avoiding the use of dispersive gratings, higher throughput of IR frequency is achieved. Thirdly, because of the simultaneous signal acquisition, FTIR interferometer has a greater sensitivity and speed in detection of signals. In addition to all above mentioned, FTIR varies from traditional dispersive spectrometers due to the use of the Fourier transform. The Fourier transform use a mathematical relationship, which entails conversion of a time domain to a frequency domain. The intensity of the reflected radiation of a broad-band source is converted to the interferogram.
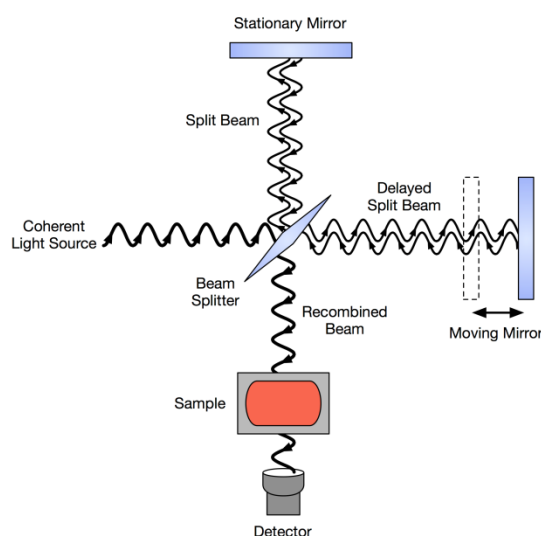


*Figure 15. Schematic representation of Mickelson interferometer*

**1.2.12 MP-AES**

Microwave plasma atomic emission spectroscopy is an atomic emission technique that is used for simultaneous multi-analyte determination of major and minor elements. The working principle of this technique is based on the fact that once an atom of a specific element is excited, it emits light in a characteristic pattern of wavelengths – an emission spectrum, as it returns to the ground state. There are several sources for atomic emission include the microwave plasma (MP) and the inductively coupled argon plasma (ICP) both of which are high temperature sources, and therefore excellent excitation sources for atomic emission spectroscopy. The nitrogen fuelled microwave plasma reaches temperatures nearing 5,000 K. At these temperatures, atomic emission is strong, producing excellent detection limits and linear dynamic range for most elements [96].

MP-AES uses microwave energy to produce a plasma discharge using nitrogen supplied from a gas cylinder or extracted from ambient air, which eliminates the need for sourcing gases. Samples are usually nebulized before to interact with the plasma in MP-AES measurements. The atomized sample goes through the plasma and electrons are promoted to the excited state (Figure 16 [97]). The light emitted electrons return to the ground state and then separated into a spectrum where the intensity of each emission line measured at the detector. Most commonly determined elements can be measured with a working range of part per million (ppm) to weight percent (wt. %). Comparable to traditional AA and AES, MP-AES has several advantages including lower cost of operation, improvement of safety, increasing detection limits and simplification of sample preparation [96].
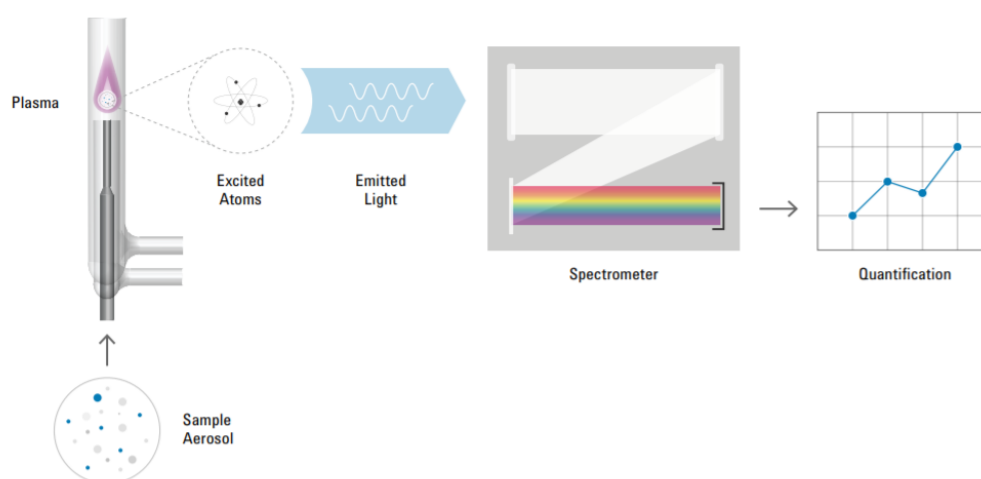


*Figure 16. Schematic diagram of a microwave plasma atomic emission spectrometer.*

# 2. Experimental part

## 2.1 Synthesis of Manganese Hexacyanoferrate (MnHCF) and its derivatives. Electrode preparation.

MnHCF was synthesized using simple reproducible co-precipitation method [66]. The solutions of manganese sulfate monohydrate ($MnSO_4 \cdot H_2O$) and sodium ferrocyanide decahydrate ($Na_4[Fe(CN)_6] \cdot 10H_2O$) (0.1 L, 0.1 M each) were prepared and added drop wise under the nitrogen flow to the solution of sodium sulfate $Na_2SO_4$ (0.1 L, 0.1 M) by means of a peristaltic pump at a rate of 4 mL min$-1$. During the addition, the reaction batch was stirred at constant temperature (40 ± 2 °C) using a thermostated bath and was stopped several minutes after the complete runover of the reagents. The obtained solution was aged for 5 days and the precipitate was collected via several consecutive centrifugation at 4000 rpm for 20 min using test tubes. After removing the supernatant, the precipitate was washed three times with distilled water, and then dried at 60 °C for 48 h.
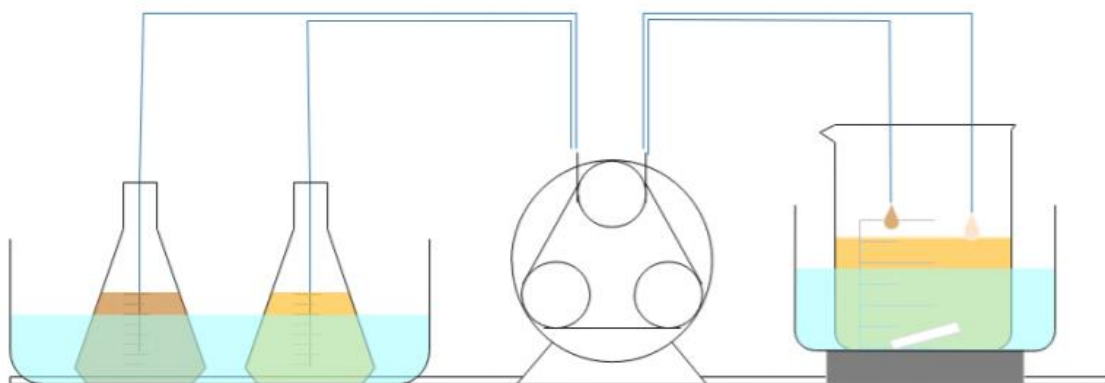


*Figure 17. Experimental set-up adopted for the synthesis of Na-rich MnHCF* [65]

The same procedure was used for synthesis of MnHCF derivatives (MnHCF-A with addition of ascorbic acid, MnHCF-C with addition of citric acid). The additional reagents (citric and ascorbic acids respectively) were added on the first stage to the solution of $MnSO_4$ with the same concentration and pumped directly to the $Na_2SO_4$ solution under the same conditions as was mentioned previously.

*Table 1. Masses of reagents for synthesis of MnHCF and its derivatives*

|  | $M_w$ (g mol$^{-1}$) | m (g) | c (M) |
|---|---|---|---|
| MnSO$_4$·H$_2$O | 169.01 | 1.6901 | 0.1 |
| Na$_4$[Fe(CN)$_6$]·10H$_2$O | 484.06 | 4.8407 | 0.1 |
| Na$_2$SO$_4$ | 142.04 | 1.4223 | 0.1 |
| Citric acid | 192,12 | 1.9201 | 0.1 |
| Ascorbic acid | 176.12 | 1.7617 | 0.1 |

To prepare the cathode slurry for Cyclic Voltammetry tests, 75 mg of synthesized compound and 20-25 mg of conducting agent (Super C65, IMERYS) were mixed properly in a mortar. After the addition of 5 mg of binder (PTFE, Solef 6020, Solvay polymer specialties), the obtained mixture was grinded around one hour until obtaining the homogenous thin solid slice. Using Hohsen puncher (with diameter 5mm) disk shaped electrodes were prepared, cast in aluminum foil (thickness 20 µm) using a blade coater and fixed to the thin electrode by pressing at 10 tons for 10 seconds. Before the actual test the electrode is placed in the corresponding electrolyte solution and left under vacuum for 2 hours.

### 2.2 Electrochemical tests

Electrochemical properties of the synthesized material were evaluated using three-electrode mode aqueous system with platinum wire as counter electrode and saturated calomel electrode (SCE) as reference electrode as shown in figure. T-shaped working electrode (Figure 18 b) was prepared from sample in aluminum foil and coated to silver for better conductivity.

Cyclic voltammetry (CV) test was performed by means of CH Instruments Model 660 at the potential range of -1.3~1.3 V vs SCE in aqueous electrolyte at different scan rate (20 mV/s, 10 mV/s, 1 mV/s), starting from OCP conditions with positive polarization. Electrochemical impedance spectroscopy (EIS) was carried out on the electrochemical workstation (CH Instruments Model 660) over the frequency range of 0.01–100 kHz with an amplitude of 5 mV.
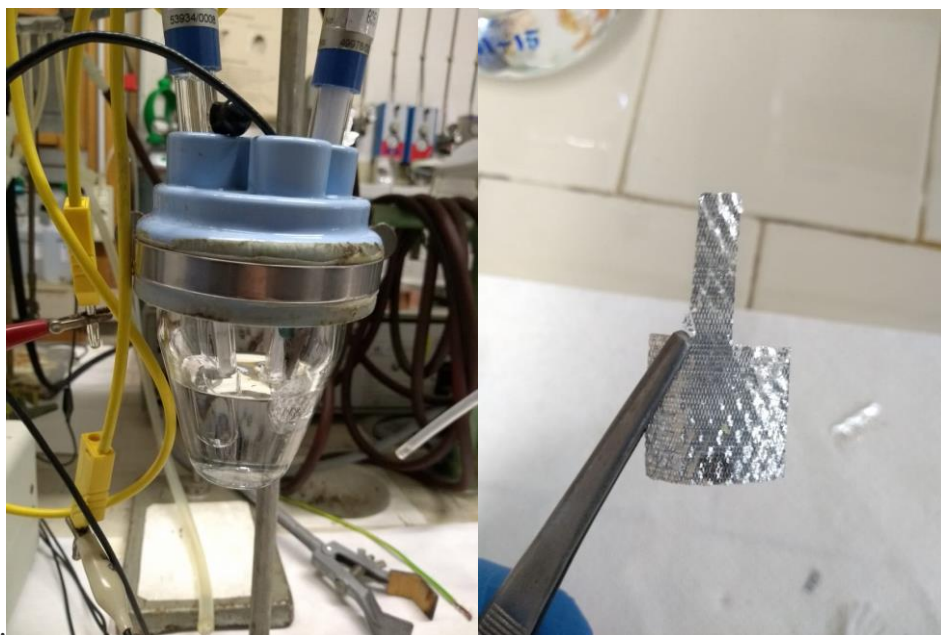
*Figure 18. a) Three-electrode test system; b) T-shaped working electrode fixed by aluminum mesh*

## 2.3 Laboratory techniques

Thermo gravimetric analysis (TGA) was carried out in TA Discovery TGA instrument from room temperature to 500°C, with a ramp of 5°C/min, and rapid cooling.

Microwave plasma-atomic emission spectrometer (MP-AES) composition analysis was done by means of MP-AES 4210 atomic emission spectrometer. During the test, first different concentration (0, 10ppm, 20 ppm, 30 ppm and 40 ppm) standard solution of Fe, Mn and Na was prepared (diluted by 0.5M nitric acid); then the sample was solved in 0.5M nitric acid. Three different analytical lines (wavelengths) were chosen for each element during the test.

Infrared spectrum was obtained using Bruker Alpha FT-IR spectrometer in ATR (attenuated total reflectance) mode at spectral range of 4000-400 cm-1.

## 2.4 Synchrotron techniques

Powder X-ray diffraction (PXRD) data were recorded using a monochromatic X-ray beam with a wavelength of 1.0000 Å at the MCX beamline in ELETTRA synchrotron Trieste, Basovizza, Italy. Data were collected on the sample in a capillary geometry, setting the spinner at 300 rpm. The X-ray diffraction (XRD) pattern was collected consecutively in the range 5°<2θ<70 °, with steps of 0.01 ° and an acquisition time of 1s/step. The corresponding optics of the line includes two mirror and monochromator where the first cylindrical mirror coated in platinum collimates the beam on the

horizontally focusing double crystal monochromator in configuration 1 to 1 and the second flat and bendable mirror focuses vertically. The double crystal monochromator (DCM) composed of two Si crystals (active area 50x50 mm$^2$, manufactured cut along the [111] direction, which can be precisely positioned and oriented in the X-ray beam). Working range of the beamline is from 6 to 20 eV, monochromator wavelength is around 1 A, max flux $10^{11}$ ph/s (9 keV), spot size on the sample is 300-2000 um and 300-1000 um for horizontal and vertical respectively. Rietveld refinement was performed using FullProf Suite software where Pseudo-Voigt * Axial divergence asymmetry shape was used. Peak shape parameters, cell parameters, background and atomic parameters were consequently refined.

X-ray absorption spectroscopy (XAS) experiments were carried out at Elettra Synchrotron Trieste, Basovizza (Italy), at XAFS beamline. The storage ring was operated at 2.0GeV in top-up mode with a typical current 300 mA. Data were recorded at both Mn and Fe K-edge in transmission mode using ionization chambers filled with a mixture of Ar, N2, and He to have 10, 70, and 95% of absorption in the I0, I1 and I2 chambers, respectively. An internal reference of titanium was used for energy calibration in each scan. This allowed a continuous monitoring of the energy during consecutive scans. The white beam was monochromized using a fixed exit monochromator equipped with a pair of Si (111) crystals. Data were collected alternatingly from 6339 to 7110 eV and from 6912 to 8346 eV around the Mn and Fe K-edges, respectively. The energies were calibrated assigning the first inflection point of the metallic manganese and iron spectra to 6539 and 7112 eV, respectively XAS data pre-treatment was carried out by means of ATHENA software. The pre-edge background was removed by subtraction of a linear function extrapolated from the pre-edge region, and the XANES spectra were normalized at the unity by extrapolation of the atomic background.

Transmission X-ray microscopy analysis was performed in MISTRAL (Soft X-ray microscopy beamline), Cerdanyola dell Valles, Barcelona, Spain. The microscope working range is varying from 270 eV to 1200 eV. A single-reflection elliptical glass capillary condenser uses to focus monochromatic light on to the sample at cryo temperature. Objective Fresnel Zone plate (of 25 or 40 nm outermost zone widths) is used to collect transmitted signal and a final magnified image is obtained by CCD camera. The usual spatial resolution in 2D TXM is 30 nm.. Energy resolution is up to E/DE=5x10$^3$, sample format -3.05 mm TEM round grid. There is possibility for tilting the angle ±65º, X-ray magnification adjustable range depends on the objective which was used. Detector type is PIXIS-XO: pixel size = 13um. Electrochemical experiments were conducted in a Swagelok-T-cell with metallic sodium as counter and negative electrode and $Na_{1.9}Mn_{1.1}Fe(CN)_6$ formulated electrode as a positive electrode. As an electrolyte, 1M $NaPF_6$ in PC was used. Approximate mass loading was 1.91 ± 0.09 mg/cm$^2$. Considered theoretical specific capacity was 150 mAh/g. Potential range: 2 < E < 4 V.

Series of samples have been cycled to the different states of charge (Table ). The cell have been dismantled in the glove box to extract the electrodes that were rinsed with DMC, dried and scraped. The powder then was deposed on the standerd-coated TEM grids and introduced to the TXM microscope through a special transport chamber that avoids contact with the air.  The samples have been tested tested to assess difference in composition, thickness effect, presence of carbon and homogenity of the samples. The resulting data was analyzed using Image J software [98].

The XRF data was collected in XRF beamline in "Elettra" synchrotron Trieste, Basovizza (Italy). Double crystal monochromator was used with resolving power $1.4 \cdot 10^{-4}$ enabling the access to the energy range of 2-14 keV. The source is re-imaged to a 450 x 300 μm beamsize at exit slits (~ 23 m from the source), with an angular divergence of 0.15 mrad and a transmitted flux of about 5 109 ph/s (at 5500 eV, machine mode 2GeV). The experimental flux curves for the 2 storage ring operation energies and are normalized to the beam. Also 2 ionization chambers are available, behind a 0.3mm thick Beryllium window. The fluorescence measurements are performed using a Silicon Drift Detector (SDD) (XFlash 5030, Bruker Nano GmbH, Germany). It has a 30 mm$^2$ nominal crystal area, a thickness of 450 μm and resolution equal to 131 eV and equipped with a Super Light Element Window (SLEW). A Zr collimator is placed in front of the detector chip to prevent the detection of photons at the edges of the crystal and to improve the energy resolution and the peak to background ratio. To prevent the detection of photo- or Auger electrons emitted from the sample surface, the SDD is coupled with an electron trap (permanent magnet) placed in front of the end [99] .

# 3. Results and Discussion

Increasing the Na content in cathode materials is one of the effective ways to achieve higher energy density. In our case, we tried to obtain sodium iron hexacyanoferrate with higher sodium content by controlling the reducing agent and reaction atmosphere during synthesis. For that purpose citric and ascorbic acids were added on the first stage to chelate the $Mn^{2+}$ in order to slow down the nucleation of NaMnHCF and promote homogeneous and near-stoichiometric crystal growth. You et al. reported that sodium iron hexacyanoferrate with high Na content ($Na_{1.63}Fe_{1.89}(CN)_6$) can be obtained with addition of ascorbic acid [99], whereas Tang and coworkers proposed the following mechanisms for citrate-assisted crystallization process of the $Na_{1.90}Mn[Fe(CN)_6]_{0.93}$: the $Mn^{2+}$ ions were first coordinated with citrate ions to form $Mn^{2+} \cdot citrate^{3-}$ chelate and then slowly coprecipitated with $Fe(CN)_6^{4-}$ to form the target products (as shown in Figure 19) [100].
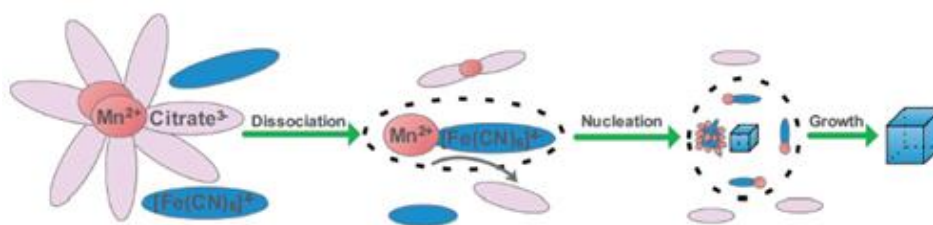


*Figure 19. Schematic representation of the citrate-assisted controlled crystallization process for the synthesis of $Na_xMnFe(CN)_6$ samples*

The stoichiometry of resulting sodium rich manganese hexacyanoferrate and its derivatives are calculated based on MP-AES composition analysis (Appendix A) and summarized in Table 2. As we can see, in defective manganese hexacyanoferrate compounds the content of sodium is gradually increased from 1.73 in MnHCF to 1.85 in MnHCF-A and 1.75 in MnHCF-C respectively that is in agreement with literature resources.

| | |
|---|---|
| *MnHCF* | *$Na_{1.73}$ Mn [Fe(CN)$_6$]$_{0.8}$* |
| *MnHCF-A* | *$Na_{1.85}$ Mn [Fe(CN)$_6$]$_{0.89}$* |
| *MnHCF-C* | *$Na_{1.75}$ Mn [Fe(CN)$_6$]$_{0.88}$* |

*Table 2. Calculated formula of MnHCF and its derivatives*

Thermogravimetric analysis (TGA) of synthesized samples exhibits two consecutive weight losses as presented in Figure 20. According to the literature [66], the first one (below 120 °C) can be attributed to the elimination of adsorbed water, whereas the second one (120-200°C) can be explained by the loss of interstitial water. In our samples, it can be easily seen that the total water content is decreased in the row MnP-MnA-MnC: 13.87%, 12.3% and 12.13% respectively. Using the first derivative of the curve, we can find inflection points which provide us information about the temperature corresponded to the maximal loss of the water at particular stage: for MnP (pristine MnHCF) it is 108 and 182°C, for MnHCF-A -106 and 181°C, while for MnHCF-C it is 173 °C for second stage and no certain temperature indicated for the first water loss. Using obtained information, we recalculated the formula of our compounds with addition of water (Table 3). General decrease in water content with increasing sodium content indicates the improved crystallinity, because zeolitic water located in the cavities can be expelled by the Na+ ions. Unlocking the active sites for the Na-storage reaction can lead to better utilization of the insertion capacities of MnHCF materials.

Table 3. Recalculated formula of MnHCF and its derivatives with addition of water

| MnHCF | $Na_{1.73} Mn [Fe(CN)_6]_{0.8} \cdot 2,36 H_2O$ |
|---|---|
| MnHCF-A | $Na_{1.85} Mn [Fe(CN)_6]_{0.89} \cdot 2,22 H_2O$ |
| MnHCF-C | $Na_{1.75} Mn [Fe(CN)_6]_{0.88} \cdot 2,16 H_2O$ |

Table 4. Weight losses in percentage and temperatures corresponding to the maximum mass losses.

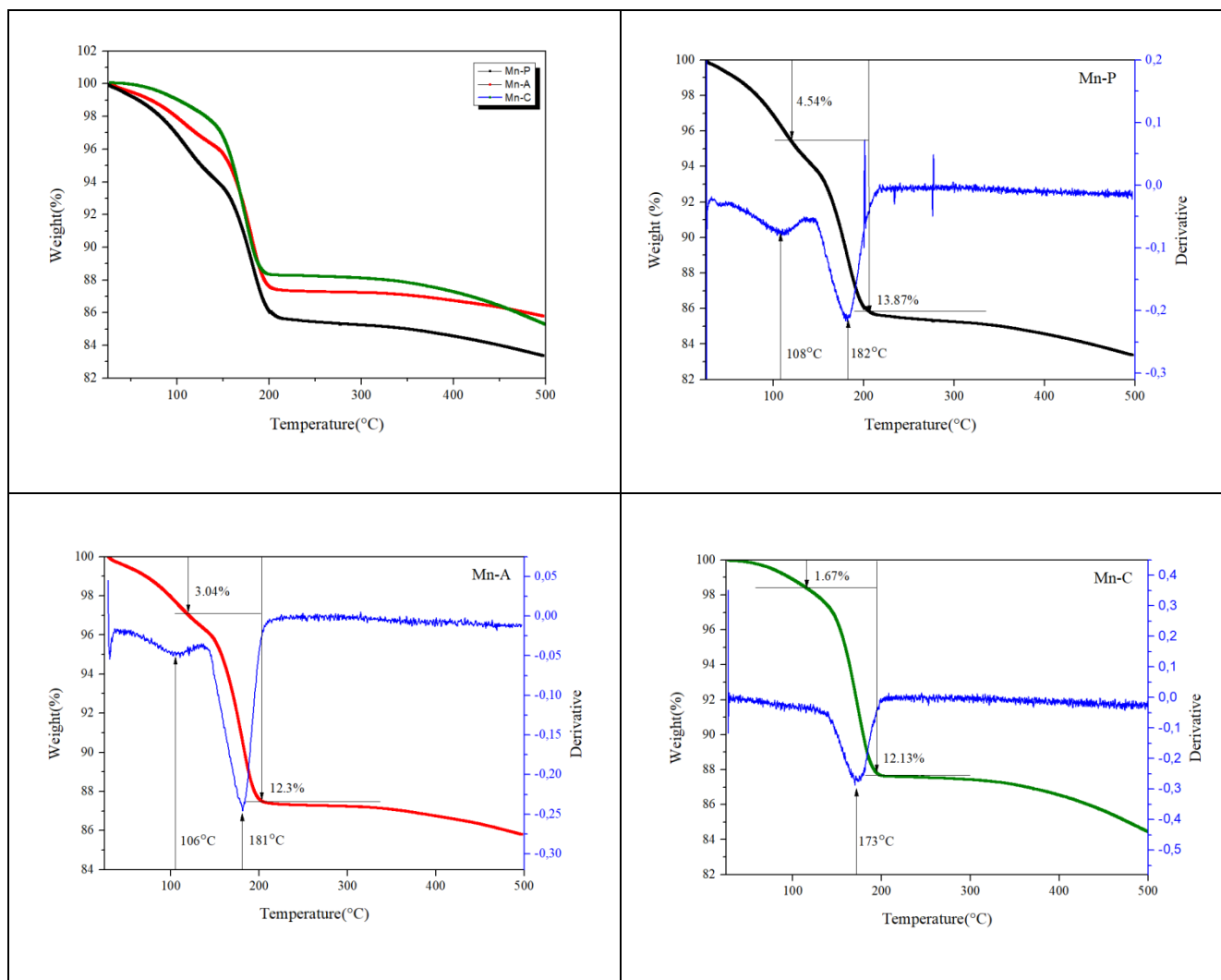| Sample | $1^{st}$ weight loss | T(°C) | $2^{nd}$ weight loss | T(°C) |
|---|---|---|---|---|
| Mn-P | 4.54 | 108 | 13.87 | 182 |
| Mn-A | 3.04 | 106 | 12.3 | 181 |
| Mn-C | 1.67 | - | 12.13 | 173 |

*Figure 20. (a) Comparison of TGA curves of three samples (Mn-P/Mn-A/Mn-C); (b-d) Individual TGA curve with corresponding derivative spectrum*

Infrared spectra, shown in figure 21, reveal that all three compounds have the same pattern just with slight difference in the intensity of the peaks. Peaks at 1620 and 3529 cm$^{-1}$ are related to interstitial water (stretching and bending mode respectively), whereas the peak at 3605 cm$-1$ is characteristic of the free surface water. A distinguishable peak at 2066 cm$^{-1}$ arises from the CN group in manganese hexacyanoferrate structure [101]. According to literature, peak corresponded to Mn-N stretching vibration mode were found in 200-350 cm$^{-1}$ region which is not observed here [102]. Fe-CN-Fe bending modes are usually observed in the far infrared region around 450-600 cm$^{-1}$. So the band at 590 cm$^{-1}$ can be assigned to Fe$^{2+}$-CN stretching mode from ferrocyanide [103, 104].
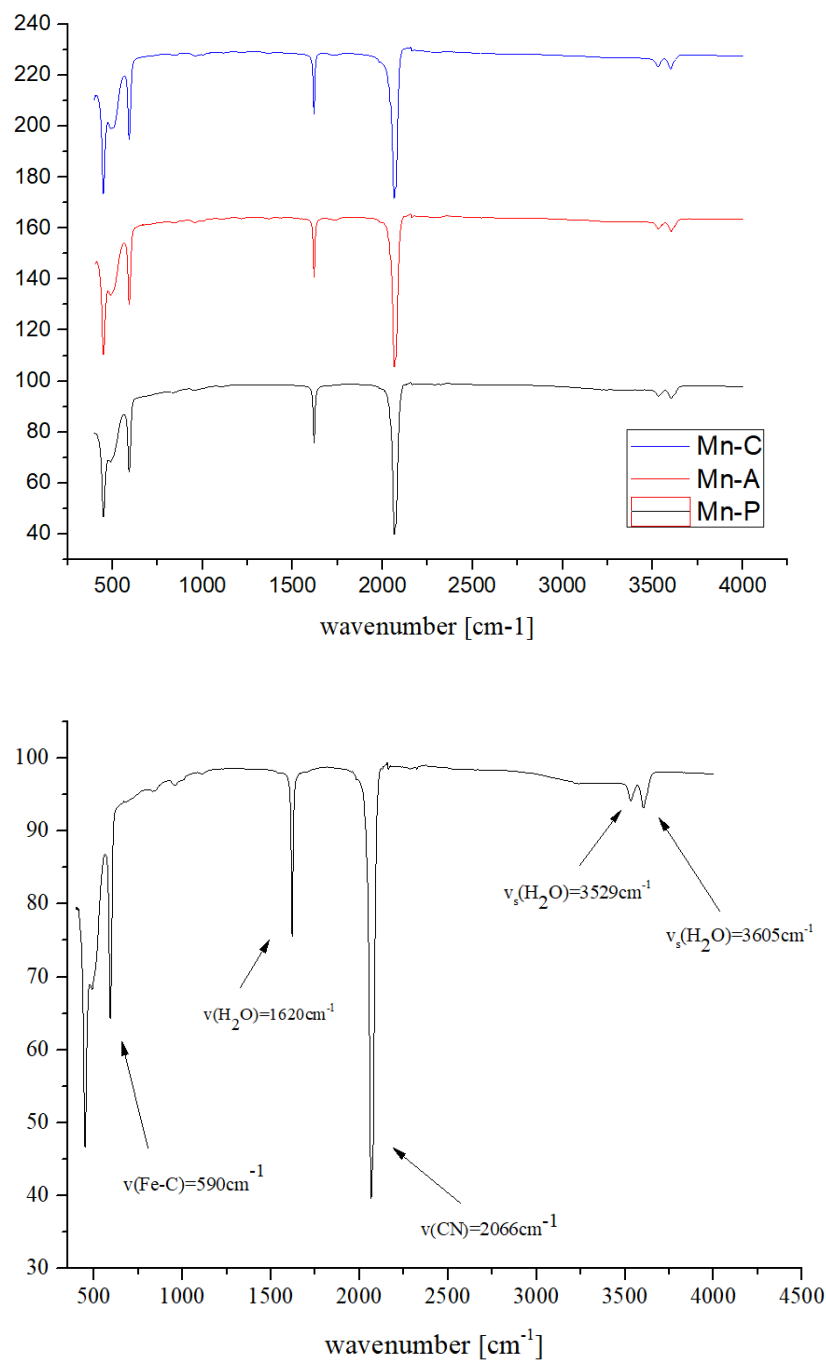
*Figure 21. a) FTIR spectrum of MnP, MnA and MnC samples b) FTIR spectrum with peak assignment*

The next step was to perform XRD analysis of MnHCF samples. For that purpose, at the beginning, using FullProf software we performed Rietveld refinement of silicon standard to derive parameters for refinement of actual samples. Generally, Rietveld refinement allows extracting a lot of information from powder XRD data such as:

- ✓ Unit cell dimensions
- ✓ Phase quantities
- ✓ Crystallite sizes / shapes
- ✓ Atomic coordinates
- ✓ Micro-strain in crystal lattice

Standard Reference Material (SRM) is used for calibration of diffraction line positions and line shapes, determined through powder diffractometry. A unit of SRM 640e consists of approximately few mg of silicon powder that is placed in a capillary for XRD. The NIST certified lattice parameter for a silicon sample at 22.5 °C is 0.5431179 nm ± 0.000 008 nm. Knowing already defined structural parameters of silicon sample, we obtain some profile related parameters (U,V,W,eta,asym)(Table 4) and use them for refinement of our samples.

Table 4. Profile related parameters from silicon standard sample

| U | 0.001606 |
|---|---|
| V | -0.000674 |
| W | 0.001116 |
| Eta_0 | 0.034160 |
| X | 0.003850 |
| Asym1 | 0.107830 |
| Asym2 | 0.014980 |

According to the literature, NaMnHCF has three different structures when precipitated under different conditions. Generally, room-temperature precipitation leads to a cubic phase with low interstitial $Na^+(x >1.5)$ and high water content (>12 wt%), whereas precipitating at elevated temperature can increase the $Na^+$ filling (1.5 <x <1.8) and reduce the interstitial water and $Fe(CN)_6^{4-}$ vacancies, resulting in a monoclinic structure that is slightly distorted (β=92.1º) from cubic. However, the remaining water in monoclinic NaMHCF is still too high (>10 wt%), which is unfavorable for the cycling stability of NIBs. Rhombohedral NaMHCF is the only phase that contains an acceptable level of water (<5 wt%), but the synthesis usually requires a long dehydration process in high vacuum or/and at high temperature [105]. In our case, we performed the synthesis at 40ºC under nitrogen atmosphere and expect to have monoclinic structure. We calculate theoretical diffraction pattern based on the structural parameters reported in the article [65] and profile parameters derived from silicon sample. Then we minimize the differences between calculated and observed pattern by least-squares method. Initially, it has been seen that phase was identified correctly (peaks at the right position) which confirmed monoclinic lattice structure for all three samples. However, some differences have been mentioned and refined in the program. Firstly, to get rid of small peak shifts, unit cell parameters were refined. Secondly, to fit the intensity of the peaks, scaling factor was refined. Thirdly, to fix the peak width we refined crystallite sizes and micro-strain parameters.

Final X-ray diffraction (XRD) pattern of the synthesized Na-rich MnHCF is reported in Figure 24 together with the Rietveld refinement. The refinement of the powder patterns led to a monoclinic structure (space group: P 2$_1$/n) in all samples with slightly different cell parameters presented in table. It is expected that after addition of chelating agents and consequent increase of sodium content, volume of cell will be increased as, for example, was shown by Liu and coworkers with synthesis of Na$_x$FeFe(CN)6 where with addition of sodium citrate (from 0 to 3,3 g) there was a shift in diffraction peaks at low angles directly indicating the increase of cell volume [106]. As we can see, overall the volume cell in our samples is almost the same. This can be explained by the fact that in our case comparatively small amount of citric and ascorbic acids (0.01 mol) were added that was not enough to induce mentionable cell expansion. Another difference can be arised from the temperature, which in our case was twice less than one proposed by Tang and was not enough to substantially decrease the water content [100].
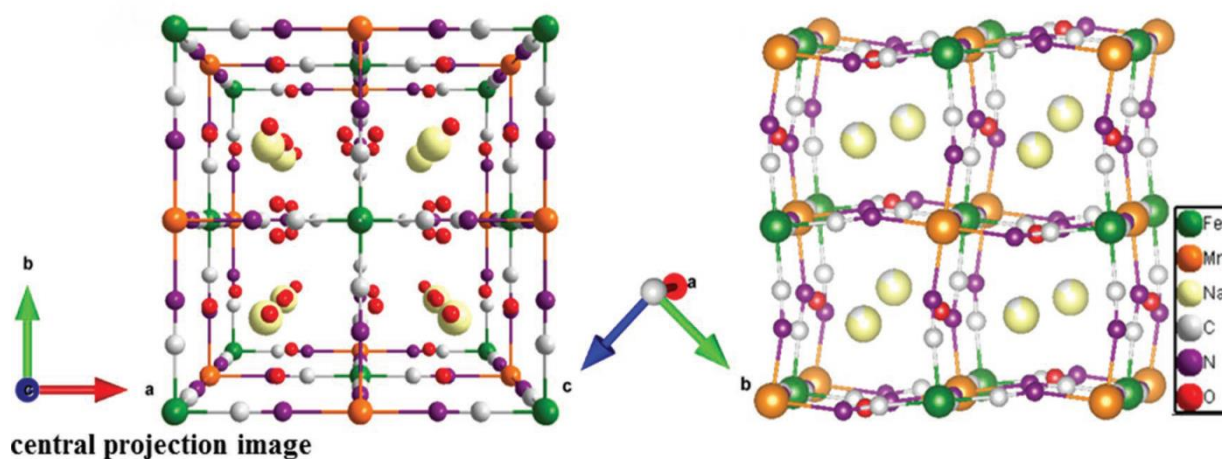


central projection image

*Figure 22. Schematic model of cubic and monoclinic Na-rich MnHCF compound* [100]

Overall, there are no new peaks observed in between XRD patterns, which proves the structural stability of the samples. The shifts in peaks at low angles are negligible, whereas the intensity of some peaks is higher in pure MnHCF (Figure 23). Elevated temperature of the synthesis which leaded to the partial removal of interstitial water and increase of sodium content cause the distortion of crystal structure and reduce the crystal symmetry, leading to the phase transitions from face-centered cubic (usual configuration of MnHCF synthesized at 25ºC [100]) to monoclinic phase. As shown in Figure 22, Tang et al. [100] suggest that the monoclinic cells can be considered as slightly distorted cubic cells if the CN$^-$ anion is rotated by 45°around the a-axis. Both iron and manganese are located in octahedral environments, Fe (2d site) surrounded by C-atoms, while Mn (2a site) coordinated to N-atoms. C- and N-atoms being the ends of cyanide bridges, water molecules and interstitial sodium ions

are placed in 4e Wyckoff sites. The refined positions of all atoms derived from the Rietveld refinement are presented in Appendix B.

*Table 5. Cell parameters and volume of synthesized compounds.*

| Sample | Cell parameters | | | | | | Volume of cell |
| | a | b | c | α | β | γ | ($Å^3$) |
|---|---|---|---|---|---|---|---|
| Mn-P | 10.56 | 7.48 | 7.39 | 90 | 92.184 | 90 | 583.43 |
| Mn-A | 10.58 | 7.53 | 7.34 | 90 | 92.098 | 90 | 584.86 |
| Mn-C | 10.59 | 7.52 | 7.32 | 90 | 92.192 | 90 | 583.81 |
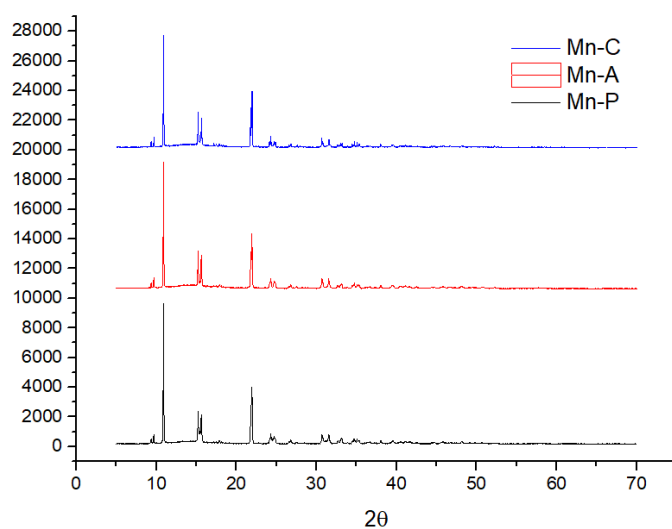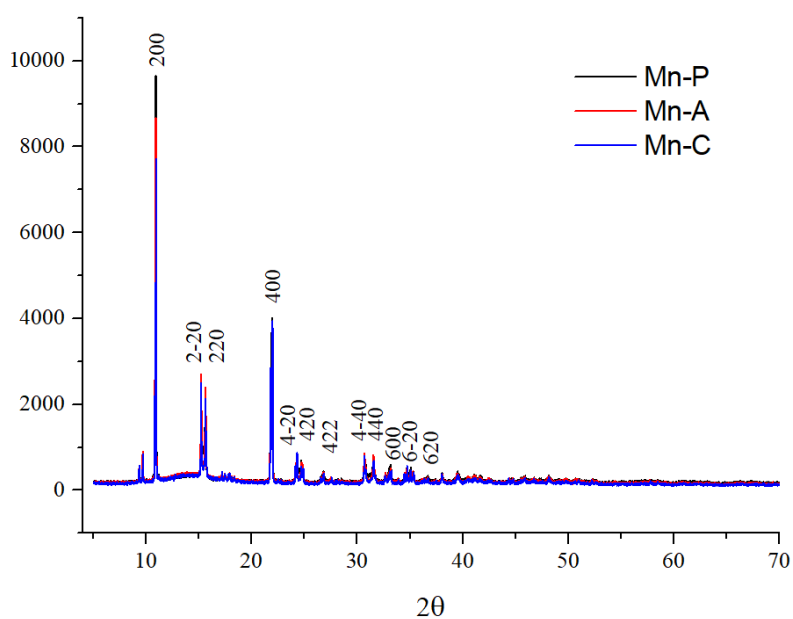




*Figure 23. XRD pattern of MnP, MnA and MnC samples.*
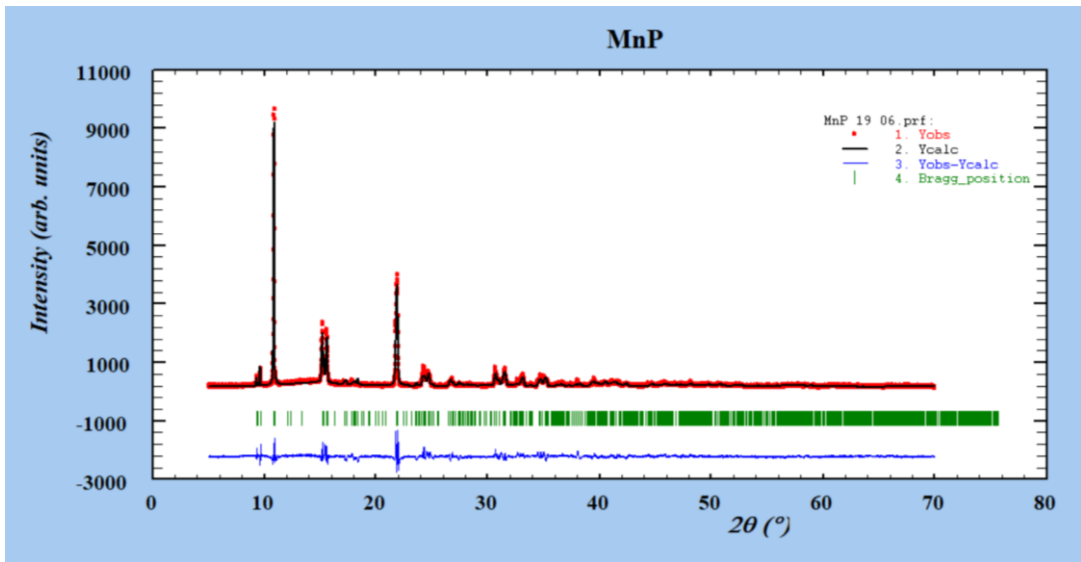*The most relevant Miller planes are indexed above the peaks.*
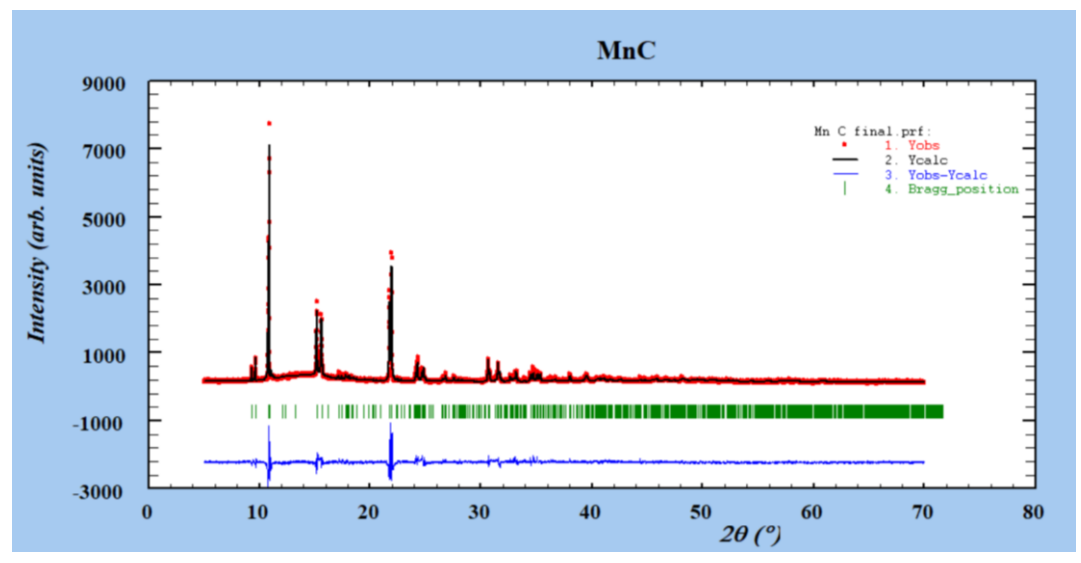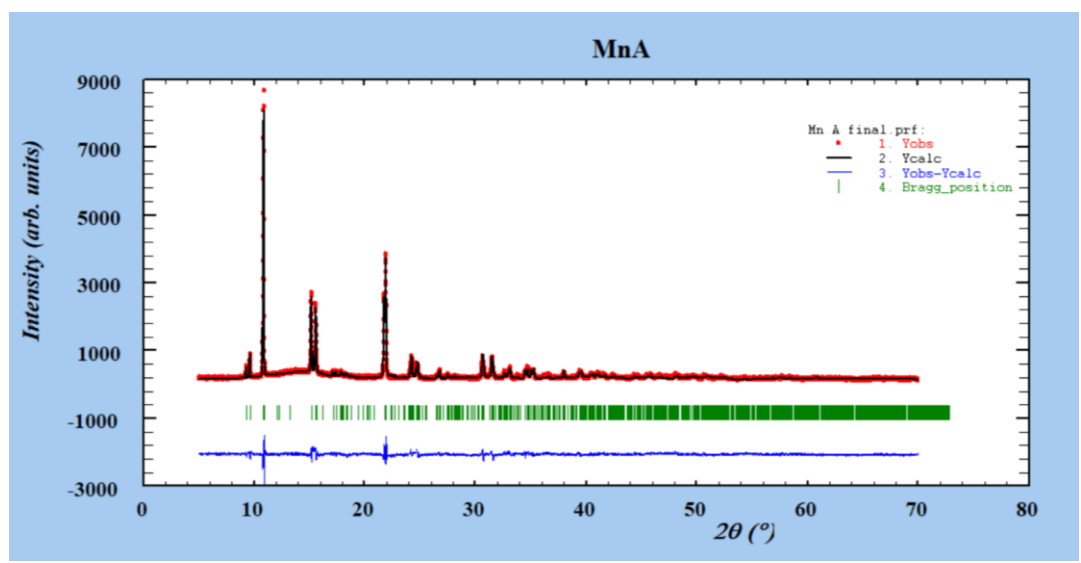
*Figure 24. Refined XRD patterns profiles of MnP, MnA and MnC samples*

The samples have been further investigated by means of the element sensitive x-ray absorption spectroscopy (XAS), which is powerful technique to study Prussian blue analogues materials because it can provide deep insight into the both transition metal centers.

Ex situ XANES spectra were recorded at both Mn and Fe K-edges of manganese hexacyanoferrates electrode materials. Starting with the Mn edge, we can see that there is a small shift (~0.3 eV) to the higher values in the row MnP-MnC-MnA as well as the slight change in the intensity of the edge.



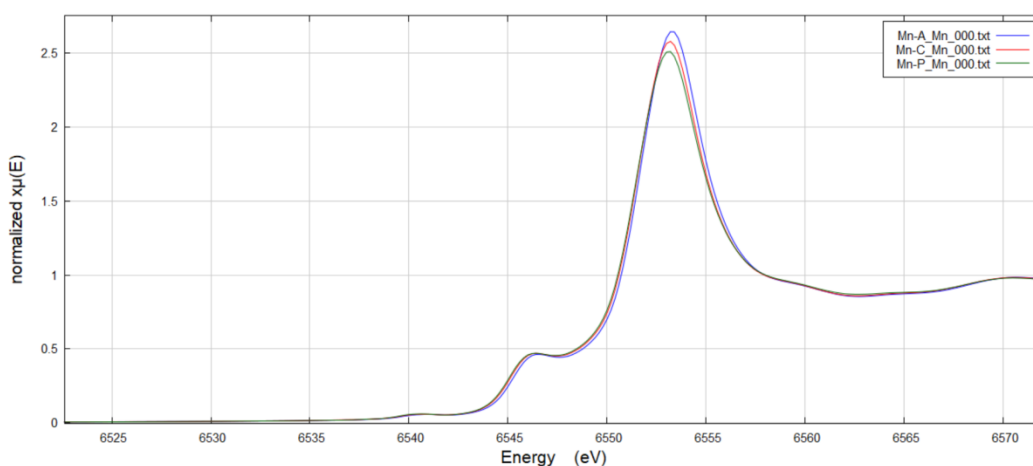*Figure 25. XANES spectra of Mn K-edge of MnP, MnA and MnC samples*

Manganese in MnHCF has high spin (HS) $Mn^{2+}$, $d^5$ electronic configuration; it is octahedrally coordinated to the N-end of cyanide ligands. In the pre-edge part, two peaks can be found and attributed to the transitions from 1s to 3d ($t_{2g}/e_g$) orbitals centered at 6540 eV and 1s to 4p orbitals at 6546 eV [65]. Again, negligible shift is observed from MnP to MnA samples especially at the second pre-edge transition.
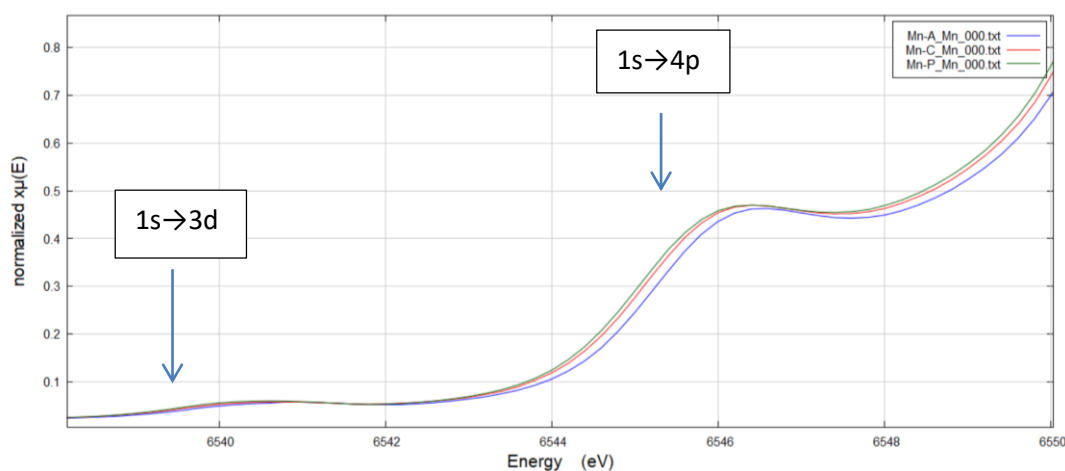


*Figure 26. Mn pre-edge structure of MnP, MnA and MnC samples*

*Table 6. Mn pre-edge transitions and corresponded energies*

| Transition | MnHCF | | MnHCF-A | | MnHCF-C | |
|---|---|---|---|---|---|---|
| | Energy (eV) | Absorption (normalized) | Energy (eV) | Absorption (normalized) | Energy (eV) | Absorption (normalized) |
| 1s→3d | 6541 | 0.0604 | 6541.2 | 0.0605 | 6541.1 | 0.0605 |
| 1s→4p | 6546.4 | 0.4525 | 6546.6 | 0.4504 | 6546.9 | 0.4524 |

Turning to Fe-edge, it can be seen that there is no observable shift found in-between samples indicating the stability of iron center. In MnHCF and its derivatives, $Fe^{II}$ is six fold coordinated to the C-end of cyanide ligands and it is expected to be found in its low spin state (LS-$Fe^{II}$) (Figure [65]) with a $t_{2g}^6 e_g^0$ electron configuration and spin multiplicity S = 0.
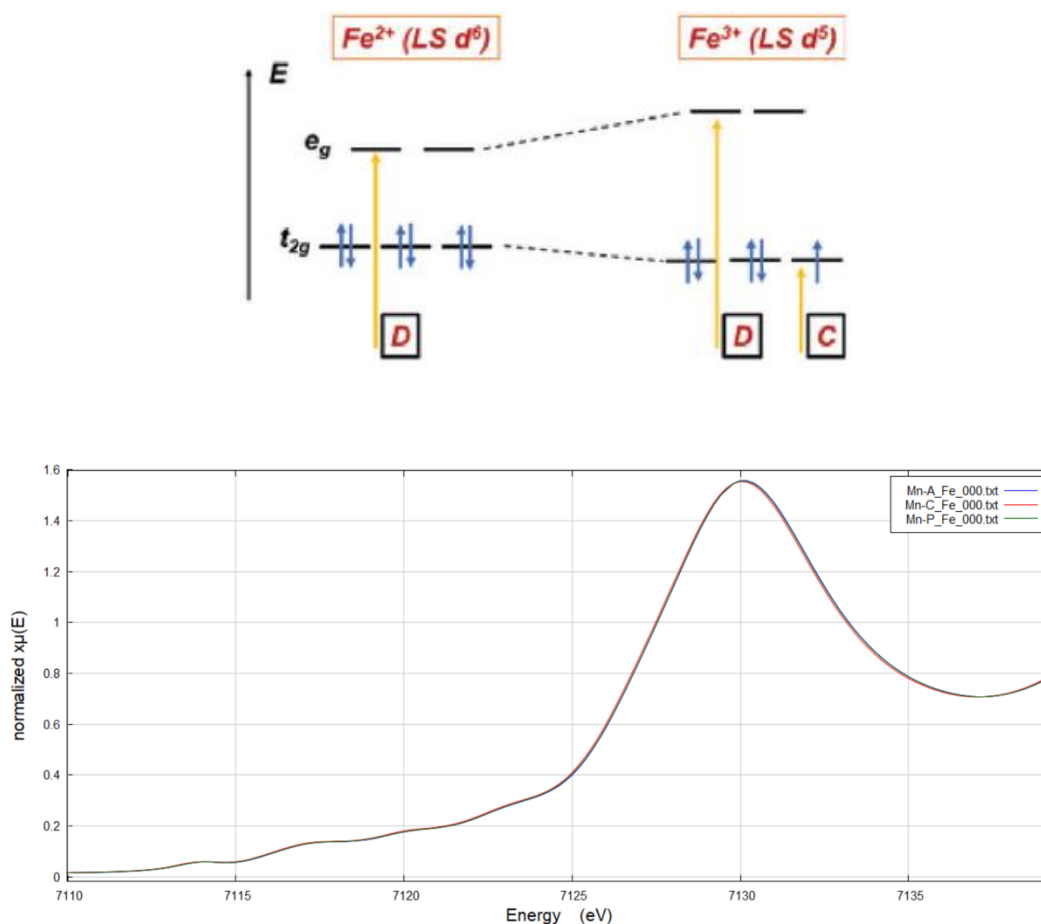


*Figure 27. Scheme of Fe low spin state (top) and XANES spectra of Fe K-edge of MnP, MnA and MnC samples (bottom)*

In pre-edge region a single transition around 7114 eV is attributed to the dipole forbidden but quadrupole allowed 1s-3d transition. Transitions occurring at higher energies (>7115 eV) arise from normally forbidden dipole transitions to the empty bound states that reflect longer-range effects of the shells beyond the cyanides [65]. The energy of transitions summarized in Table 7.
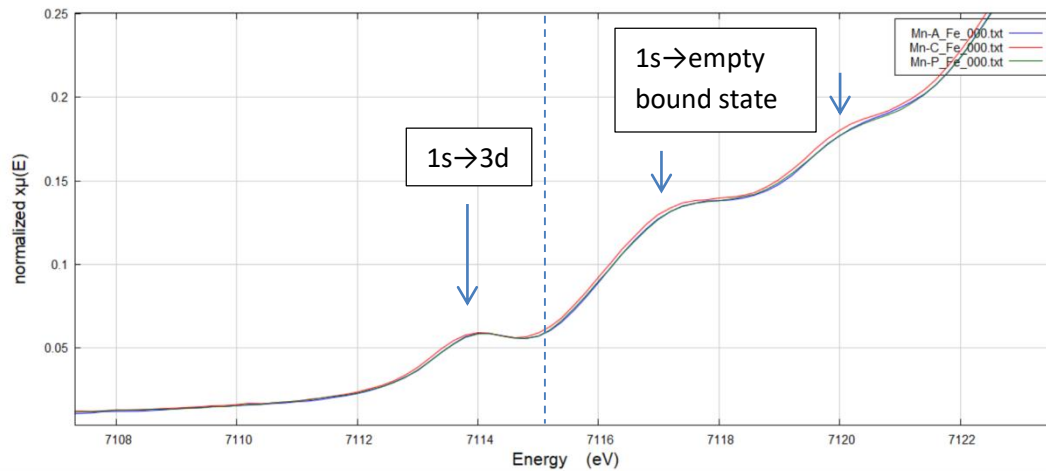


*Figure 28. Fe pre-edge structure of MnP, MnA and MnC samples*

*Table 7. Fe pre-edge transitions and corresponded energies*

| MnHCF | | MnHCF-A | | MnHCF-C | |
|---|---|---|---|---|---|
| Energy (eV) | Absorption (normalized) | Energy (eV) | Absorption (normalized) | Energy (eV) | Absorption (normalized) |
| 7114.4 | 0.059 | 7114.4 | 0.059 | 7114.3 | 0.06 |
| 7117.4 | 0.133 | 7117.39 | 0.133 | 7117.45 | 0.132 |
| 7120.4 | 0.181 | 7120.4 | 0.181 | 7120.5 | 0.183 |
| 7123.2 | 0.270 | 7123.2 | 0.271 | - | - |

A relevant structural information of the local coordination site around the metals can be gained by a suitable EXAFS analysis. The analysis have been performed by means the GNAXS program [107] which takes into consideration the multiple scattering formalism (MS) and allows a direct comparison of the experimental spectra to a theoretical one. The method used the decomposition of the EXAFS signals into a sum of several contributions, namely, the n-body terms. The theoretical signal was calculated ab initio and contained the relevant two-body $\gamma(2)$, three-body $\gamma(3)$, and four-body $\gamma(4)$ MS terms [108]. The two-body terms were associated with pairs of atoms and probed their distances and variances. The three-body terms were associated with triplets of atoms and probe angles, and bond–bond and bond–angle correlations. The four-body terms were associated with chains of four atoms, and probe distances and angles in-between, and bond–bond and bond–angle correlations. However, since Fe-C-N-Mn chains featured angles in-between close to 180°, the actual number of parameters used to define the $\gamma(3)$ or the $\gamma(4)$ peaks was reduced by symmetry. All details concerning the parameterization and optimization of the fit for the hexacyanometallate cases is available in the references [109].

Figure 29 illustrates an example of preliminary EXAFS data analysis, for the Mn-P powders. The left one displays the K2-extracted experimental EXAFS signals and the comparison to the theoretical model, which was built up based on the previous published similar material [65] whereas in the right picture corresponding Fourier Transforms (FTs) curves are shown. It can be said that even though this is a preliminary fitting, a good match between the two curves is reached therefore we can confirm the accuracy of the structural model used. Similar plots are available for the other two samples (MnA and MnC)(Appendix C). Table 8 summarizes the structural parameters, in terms of pair distance of the -Fe-C-N-Mn- structural unit. As we can see, the interatomic distances are approximately the same for all three samples indicating the identical local structure in the MnP sample and its derivatives (which was also previously confirmed for the extended range by XRD). Debye-Waller factor is also almost the same for all samples, whereas just for MnA asymmetric $\beta$ parameter which can be related to the structural disorder is taken higher for better fitting. We could say that Fe-C-N framework is quite stiff and stable and that has been confirmed by the obtained distances which show a good correlation.
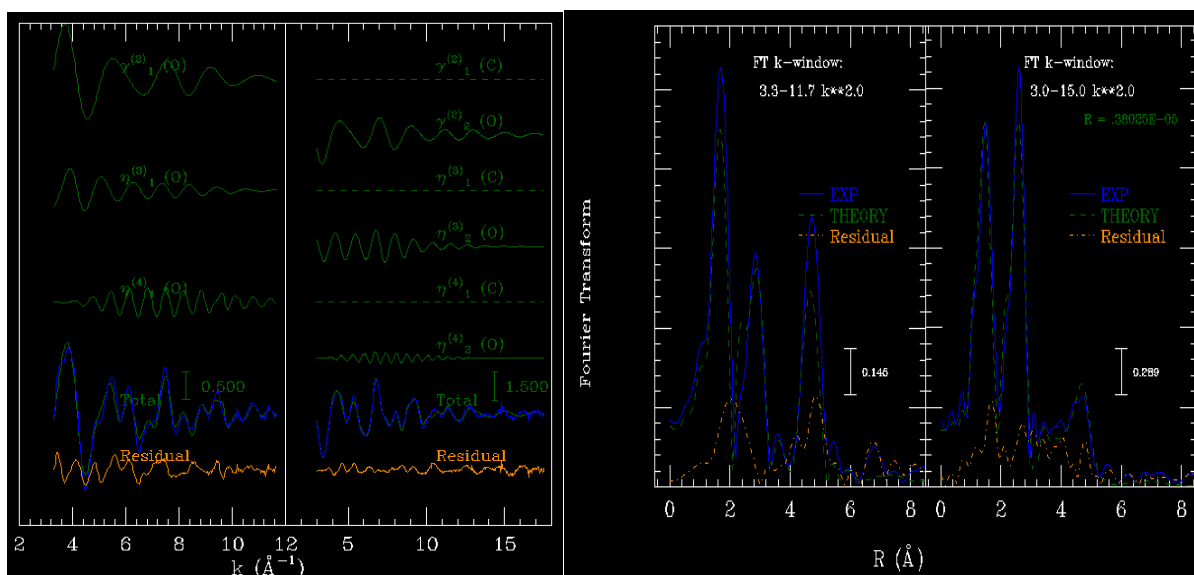
*Figure 29. K2-extracted experimental EXAFS signals and the comparison to the theoretical model (left); Fourier Transforms (FTs) curves (right)*

*Table 8. Interatomic distances derived from EXAFS fitting*

|  | *Mn-P* | *Mn-C* | *Mn-A* | *MODEL* |
|---|---|---|---|---|
| **Fe-C / Å** | *1.874* | *1.875* | *1.875* | *1.876* |
| **σ² Fe-C / Å²** | *0.0025* | *0.0024* | *0.0022* | *0.003* |
| **C≡N / Å** | *1.182* | *1.184* | *1.183* | *1.183* |
| **σ² C≡N / Å²** | *0.010* | *0.010* | *0.008* | *0.010* |
| **Mn-N/ Å** | *2.182* | *2.183* | *2.184* | *2.18* |
| **σ² Mn-N / Å²** | *0.0068* | *0.0058* | *0.0054* | *0.0065* |
| **beta (asym)** | | | *0.148* | |

# Electrochemical application

Electrochemical measurement of synthesized samples was performed by the means of cyclic voltammetry. For that purpose, series of pellets were tested in sodium nitrate electrolyte solution with different concentrations (0.1 M, 1M, 5M) at different scan rate (50 mV, 20mV, 10mV, 5mV, 1mV, 0.5mV) using three electrode system.

According to the literature, two pair of oxidation/reduction peaks should be observed in MnHCF material: first one is attributed to the redox transitions of the carbon-coordinated $Fe^{2+}/Fe^{3+}$ couple, whereas second - to the nitrogen-coordinated $Mn^{2+}/Mn^{3+}$ couple in the PB framework. For example, Cui and coworkers reported that three electrochemical processes have been clearly visible at 0.8, 0.9, and 1.4 V (vs. SHE) in manganese hexacyanoferrate sample presented in Figure 30. The electrochemical processes at 0.8 and 0.9 V are mainly attributed to the electrochemical activity of Fe ($Mn^{II}$–N-C–$Fe^{III/II}$), and they correspond to the extraction/insertion of sodium ions from the rhombohedral and cubic phases, respectively. Mn is primarily responsible for the poorly reversible electrochemical process at 1.4 V ($Mn^{II/III}$–N-C–$Fe^{III}$). This irreversibility can be explained by the combined effects of internal charge-transfer processes, hybridization between the Mn and N orbitals, and the oxidation of the aqueous electrolyte at this elevated potential [110].
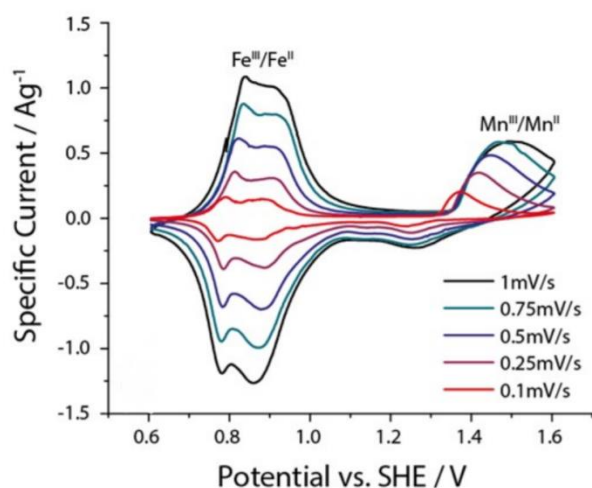


Figure 30. Cyclic voltammogram of a MnHCF in a pH=2, saturated NaClO4 aqueous electrolyte at different scan rates (0.1, 0.25, 0.5, 0.75, 1 mV s -1)

As shown in Figure 31, cyclic voltammetry (CV) curves of pristine MnHCF were recorded in the voltage range -1 to 1.2 at three different concentrations. The effects of scan rate on the peak resolution was examined. When the fast scan rate (50 mv/s, 20mV/s and 10mV/s) was applied, the electrolyte possibly does not have enough time to fully insert into the electrode material, and therefore the profile of oxy-reduction peaks is less evident. With increasing of scan rate peaks shifted to more positive values centered at 0.2 V for reduction and 0.7 V for oxidation. These peaks can be attributed to the reversible redox reaction of $Fe^{II}$ to $Fe^{III}$ in MnHCF. Even though the system should undergo double

reduction and double oxidation in NaNO$_3$ electrolyte and we expect to have a peak for Mn$^{2+}$/Mn$^{3+}$ at 1-1,2V, evident Mn peak has been found only at 1 mv/s in 0.1 M solution (anodic peak at 0.7 V). Looking at the influence of the concentration of electrolyte, it seems that 1 M solution is optimal for electrochemical test of manganese hexacyanoferrate sample because it gives the best resolution (separation) of peaks.
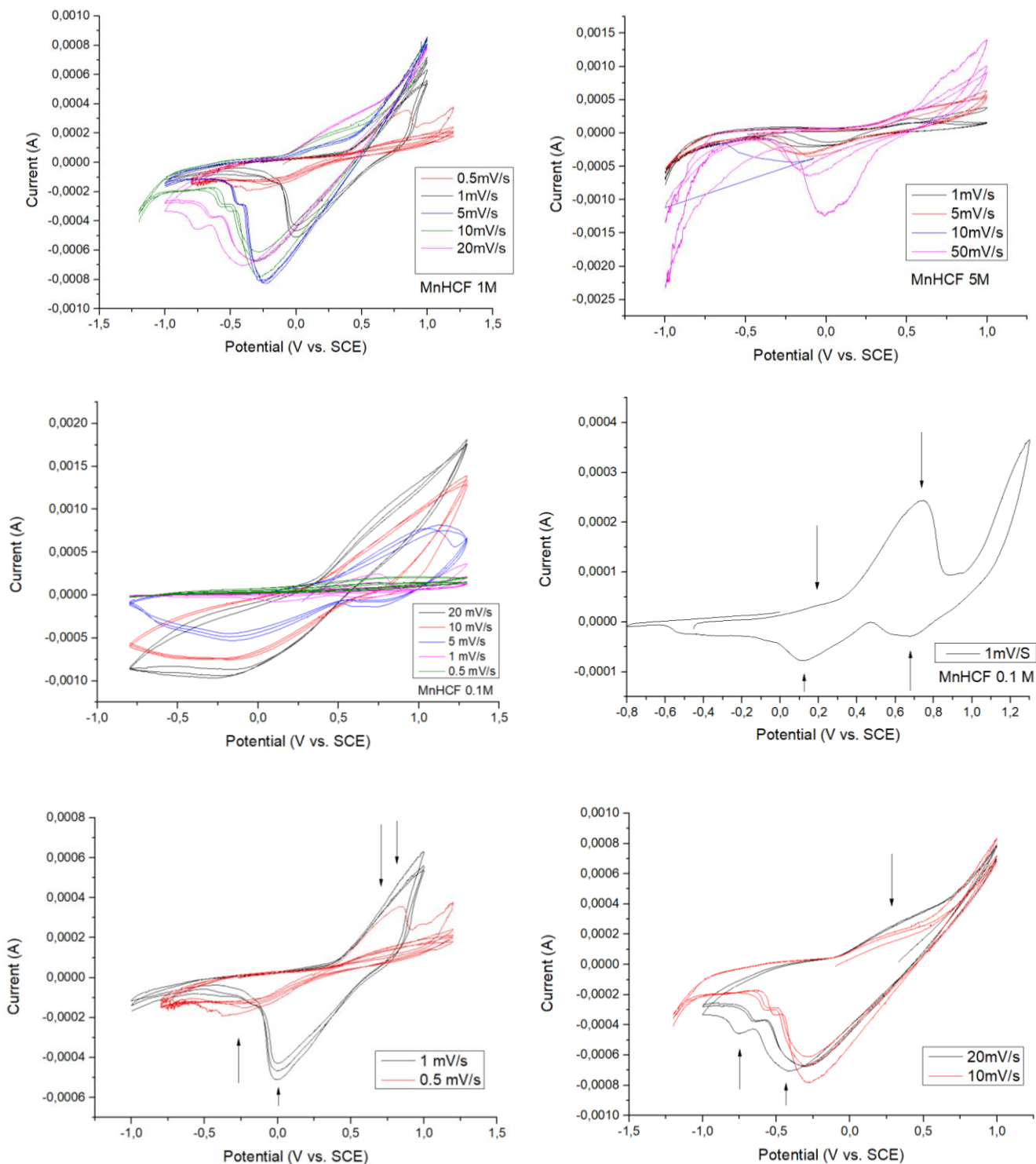


*Figure 31. Cyclic voltammetry of MnHCF in different concentrations of NaNO3 electrolyte at different scan rate*
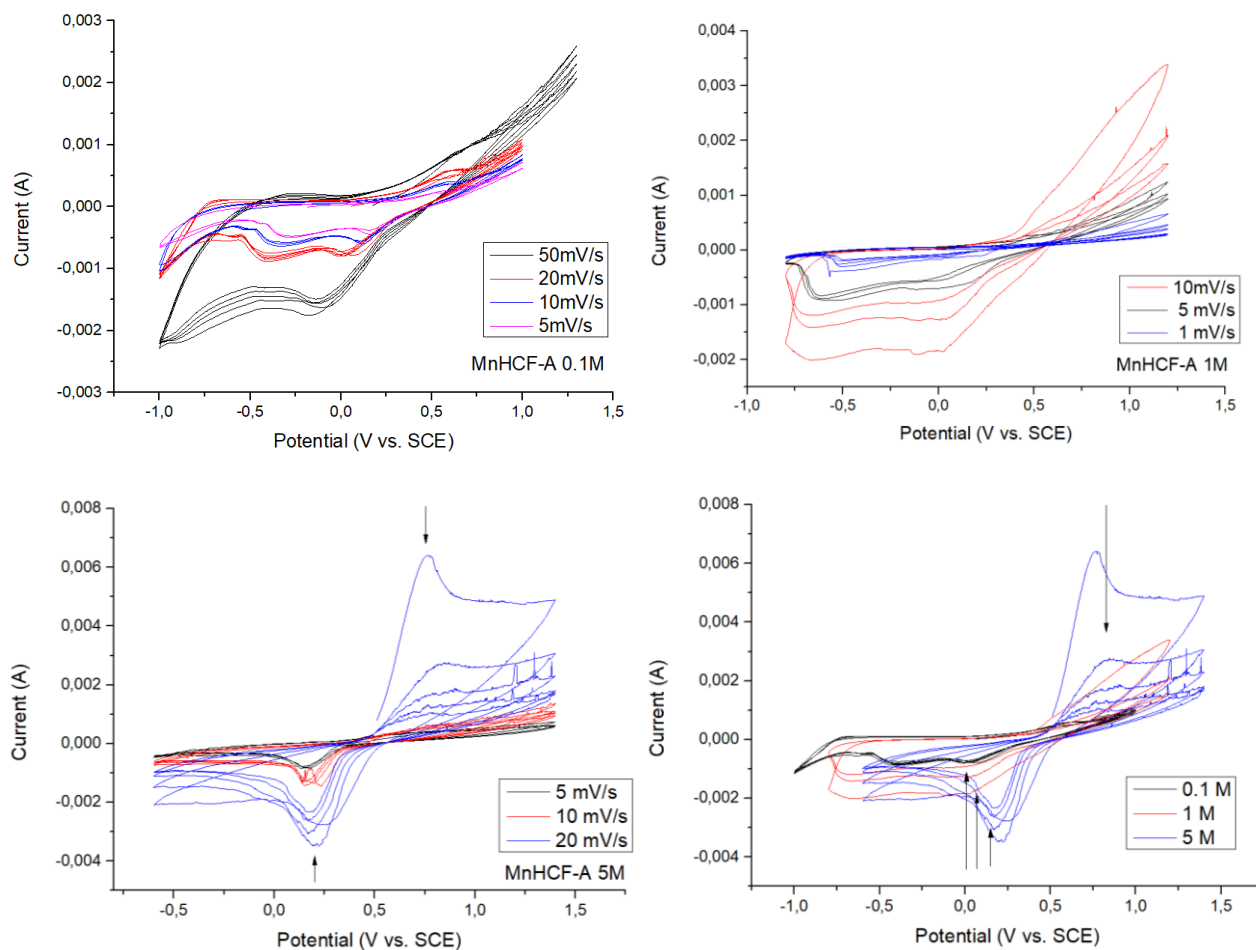
*Figure 32. Cyclic voltammetry of MnHCF-A in different concentrations of NaNO3 electrolyte at different scan rate*

Turning to MnHCF-A sample, cycling voltammetry tests were run in the -1 < E < 1.3 V vs. SCE potential window at different scan rates and various concentrations. One couple of oxy-reduction peaks is observed which position depends on the applied scan rate: at lower scan rate the process is being tested slowly, therefore the measured current is more sensitive to detail of the redox process. For example, in 5 M solution we can see the reduction peak centered around 0.2 V and oxidation peak centered at 0.7 which again can be attributed to $Fe^{2+}/Fe^{3+}$ redox couple. Comparing experiments in different concentrations, we can see that 5M solution provides better resolution, leads to the mentionable shift (~0.3 V) of the reduction peak to higher potentials and shows oxidation peak more distinct compared to less concentrated electrolytes. This result has been expected from Nernst equation which predict 0,295 V shift from 0.1 to 5 M concentration.
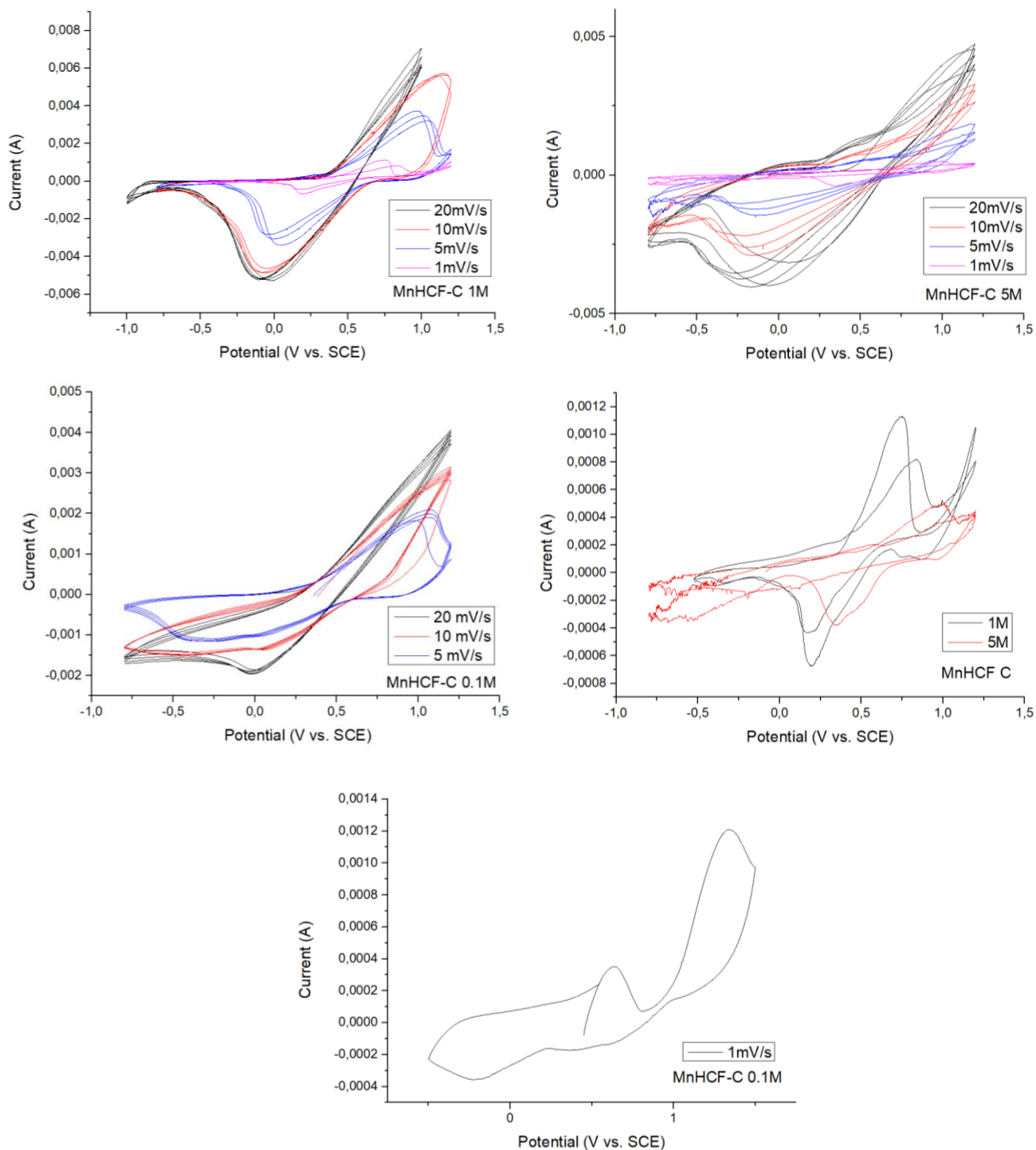
$$E = E^0 - \frac{0.0592V}{n} log \frac{[Ox]}{[Red]}$$

*Figure 33. Cyclic voltammetry of MnHCF-C in different concentrations of NaNO3 electrolyte at different scan rate*

As for MnHCF-C, in all three cyclic voltammograms, there have been sharp peaks centered around 0.7-0.8 V (oxidation) and 0.2-0.3 V (reduction) which were as previously ascribed to iron redox couple (Figure 33). At 1 and 5M solutions, the second peak attributed to $Mn^{2+}/Mn^{3+}$ has been visible in the reduction part at 1V, however no oxidation peak was detected. On the other hand, during one of the tests in 0.1 M solution, at first cycle distinct $Mn^{2+/3+}$ and $Fe^{2+/3+}$ have been detected

( at 0.65 and 1.35V respectively), but both disappeared during the cycling. The best resolution was achieved in 1 M sodium nitrate solution, whereas with the increase of the concentration, a mentionable shift to the higher potentials has been detected (~0.2 V).

Overall, it can be said that just in MnP and MnC samples there have been some evidence that Mn sites are active during the charge-discharge process, because its oxy-reduction peaks have appeared in cyclic voltammograms. $Fe^{2+}/ Fe^{3+}$ redox couple was consistent with values from the literature and has been observed at approximately the same values in all samples. We could say that by the means of CV tests, activation of second metallic center could not be confirmed with a great certainty. This can theoretically be explained by the fact that it merges within the Fe redox center, however no experimental evidence confirmed it.

**X-Ray Fluorescence spectroscopy**

2D XRF analysis was done on pristine, sodium containing charged (NaFC) and discharged (NaFD) samples and corresponding charged and discharged samples after 20 cycles (NaFC20 and NaFD20, respectively) at two different edges: manganese and iron. The samples have the similar to the MnP structure, but have been synthesized previously. Two different energies have been used 7200 and 6553 eV (for the selective excitation of Mn fluorescence solely); the beam size = 200 x 100 mm$^2$. As we can see (Figure 34), at both edges several hotspots can be observed which corresponded to areas with stronger signal intensity. After comparing these hotspots' XRF spectra with general spectrum, it can be seen that all hot spot regions show identical to the cumulative (total) spectrum. To investigate the nature of hotspots, we are working at Mn edge because the Mn K-edge evolution suggests a deep modification of the Mn local environment, as well its strong oxidation as a result of the alkali ion removal, resulting in the energy of the white line shifted roughly 5 eV toward higher energy, whereas the Fe K-edge displays a similar trend but with a much smaller energy shift of 1 eV which will be much more difficult to detect [65].

*Table 9. List of samples for XRF measurements*

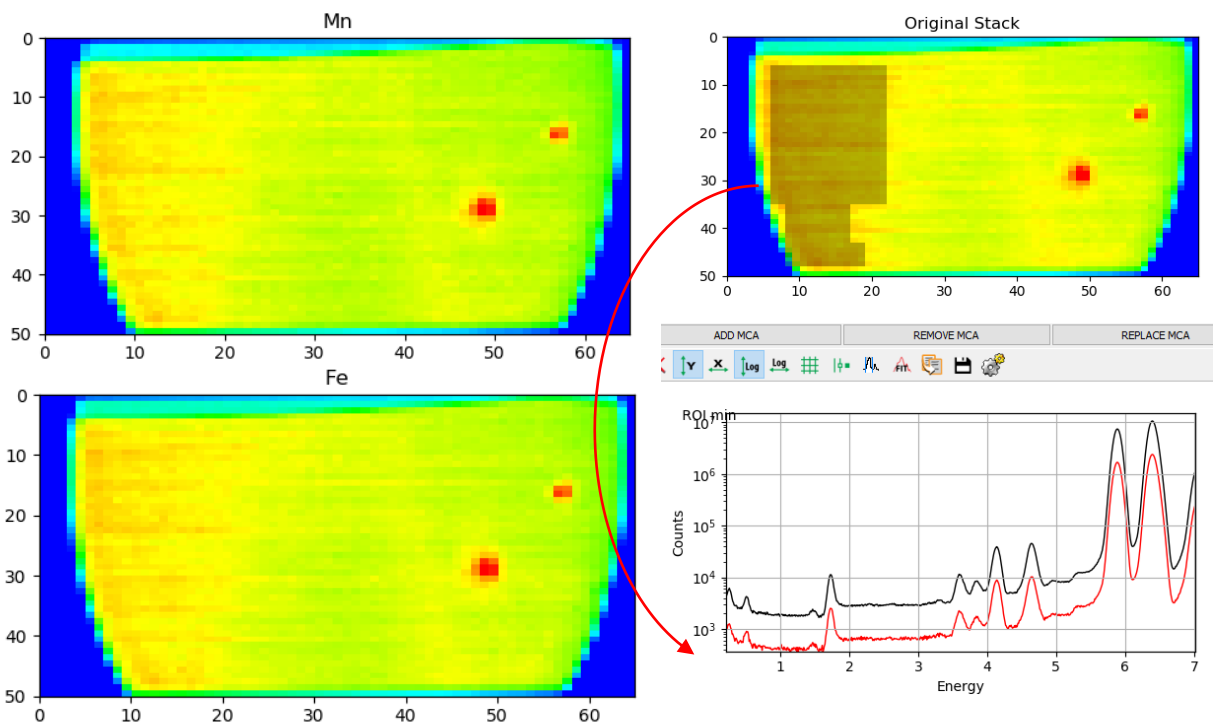| Sample | Conditions |
|---|---|
| *Pristine* | *Formulated electrode* |
| *NaFC* | *Fully charged, 1 cycle* |
| *NaFD* | *Fully discharged, 1 cycle* |
| *NaFC20* | *Fully charged, 20 cycles* |
| *NaFD20* | *Fully discharged, 20 cycles* |

*Figure 34. 2D image of Pristine sample at Fe and Mn edges, energy 7200eV and comparison of hot spots and average spectra*

After 20 consecutive cycles (Figure 35), more hotspots have been detected at 7200 eV at Mn edge. Again comparing the spectra of the inhomogenities in NaFC20 with general spectrum, it can be mentioned that they are similar which indicates no significant change in composition.
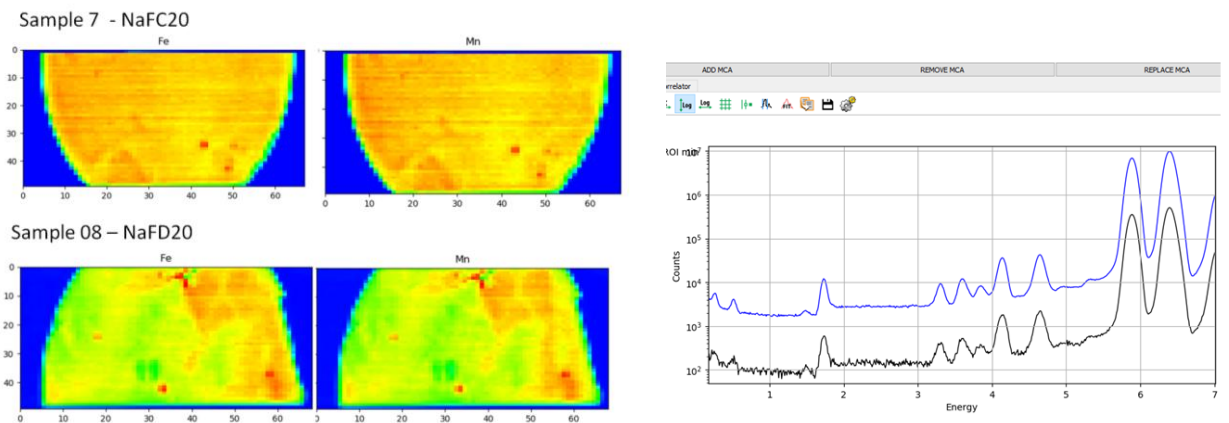


*Figure 35. 2D image of NaFC20 and NaFD20 samples, Fe (on the left) and Mn (on the right), energy 7200eV*

In discharged NaFD20 sample (Figure 36) inhomogenities at the borders are more evident. Looking at hotspots' spectra, again no changes in composition are observed, which is logical as these hotspots have been detected initially in pristine sample.
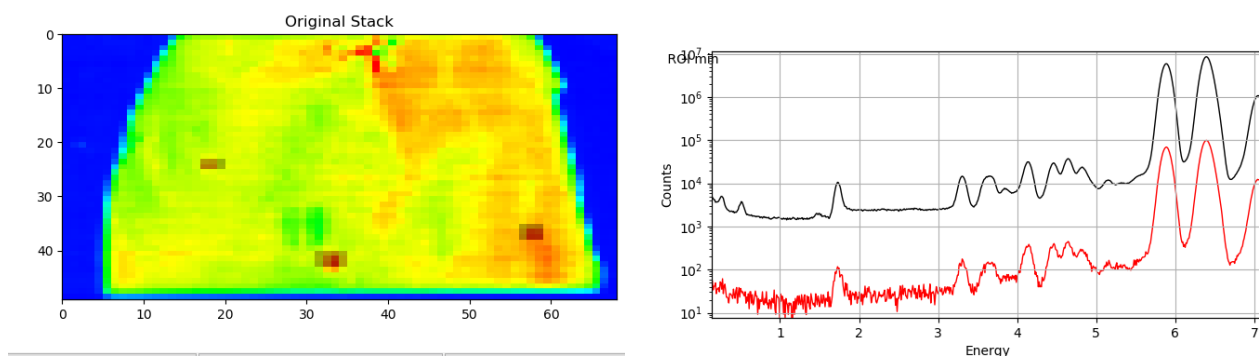
*Figure 36. 2D image of NaFD20 samples and comparison of its spectrum with general specrtum*

Moving the incident energy at 6553 eV and looking at XANES spectra, we can see that oxidized species will have a shift to higher values and consequently at 6553 eV the contribution of oxidized manganese is much lower, compared to the reduced one. This means that looking at the position of Mn edge at different spots, we can differentiate the presence of reduced/oxidized species or combination of both. Comparing the images of pristine sample at two energies (6553 and 7200 eV), no differences in Mn distribution were observed.
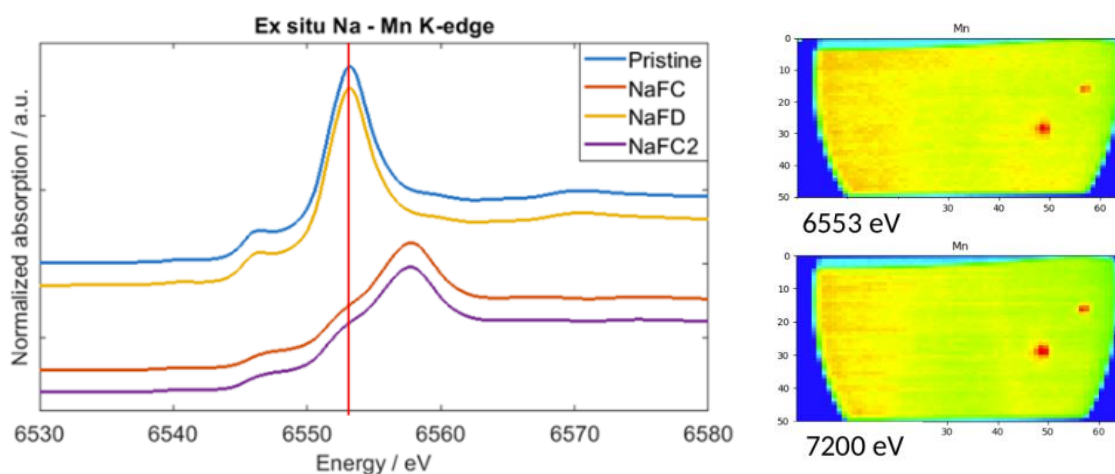


*Figure 37. K-edge of the Mn in the oxidized (charged: NaFC and NaFC2) and reduced (Pristine and NaFD) samples (on the left)* **[65]** *and 2D images of pristine sample at 6553 and 7200 eV*

As was mentioned previously, in NaFC20 the distribution of the (reduced) Mn is clearly higher at the borders at 6553 eV. This was not observed at 7200 eV, where we excite Mn in all the oxidation states. In the observed XRF spectrum, we can see some differences: the Cd doublet (probably from separator) is divided into two components found at low energy (red regions) and high energy (green region) (Figure 38).
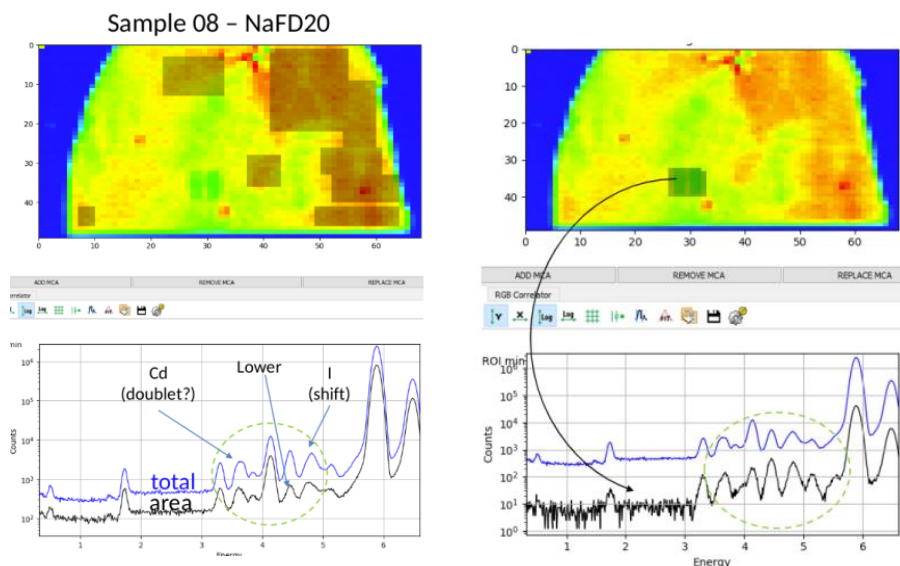
**53**

*Figure 38. 2D image of NaFD20 and corresponding XRF spectra of different hot spots*

Turning to XANES spectrum, it can be seen that after one cycle in both charged and discharged samples there is no differences in spectra indicating its structural stability. However, in NaFC20, some differences are observed in XANES spectrum which means the appearance of some reduced species after 20 cycles especially in the periphery areas (B and C regions respectively).
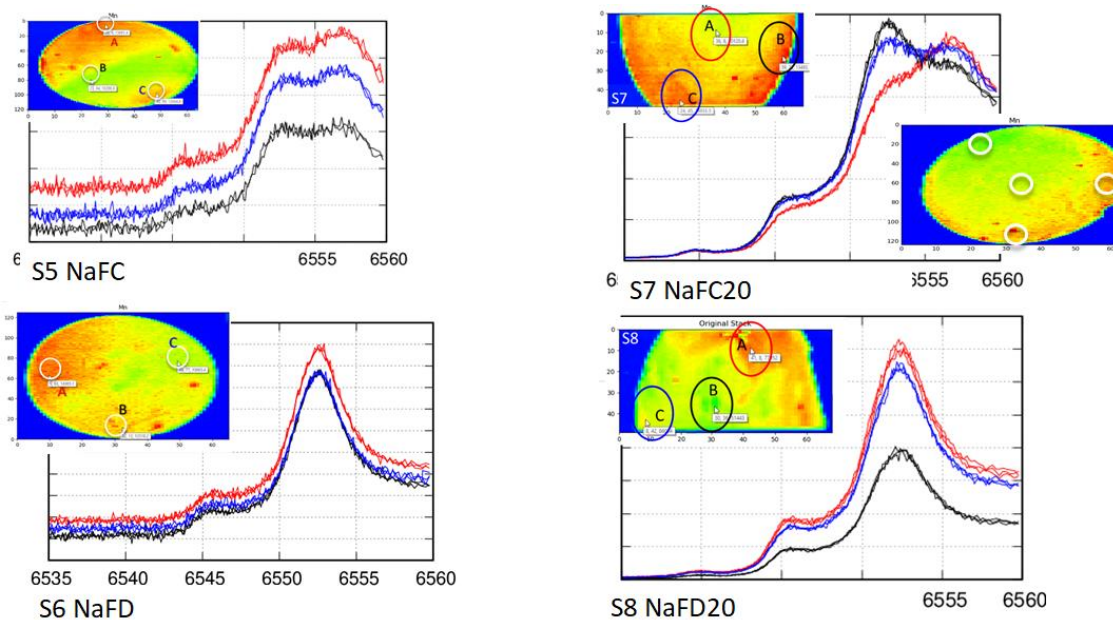


*Figure 39. 2D image of cycled charged and discharched samples and corresponding XANES spectra of different hot spots*
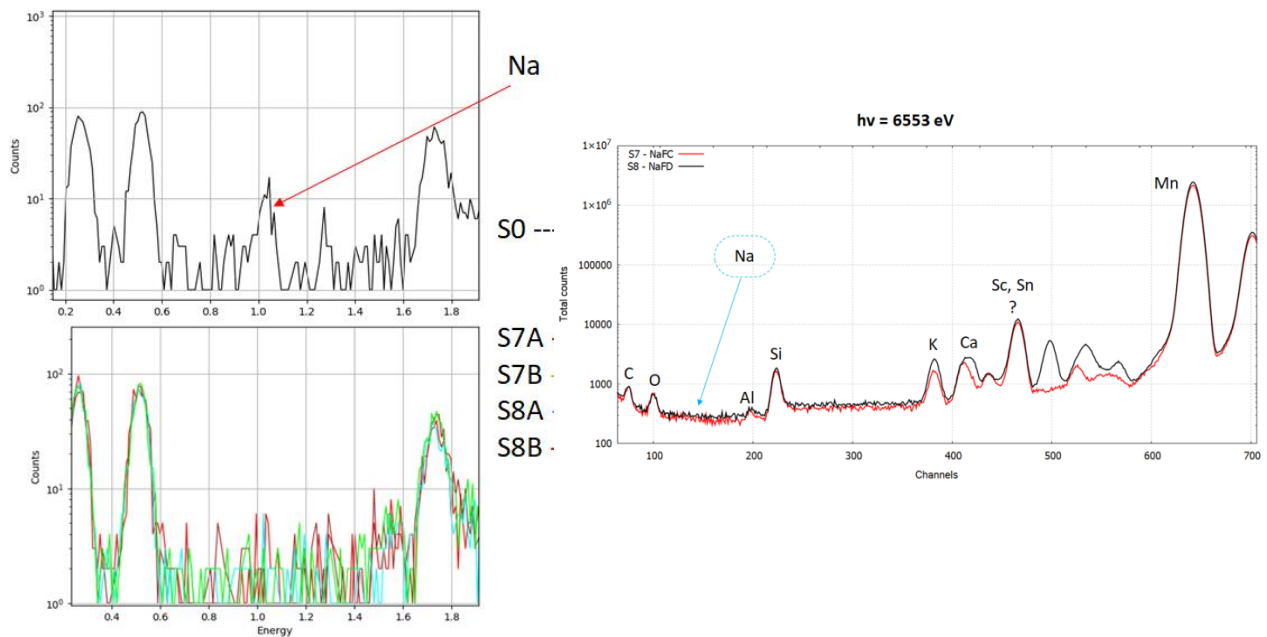
*Figure 40. XRF spectrum of NaFC and NaFD samples*

Interestingly, that in the XRF spectrum of pristine sample, al low energy part Na signal can be detected. However, in both charged and discharged samples it is disappeared. This can be explained by the fact that fluorescence energy of sodium was absorbed by plastic.

Overall, 2D XRF analysis can be very important technique for the characterization of the materials and revealing of the appearance of reduced/oxidized species during the cycling. In our case, it can be seen that during the cycling, discharges species of manganese started to appear in the charged samples (NaFC20) especially on the edges parts.

**Transmission X-ray Microscopy**

TXM measurements were performed at three different edges: iron, manganese and nitrogen of the pristine, charged and discharged sample, after one and fifty cycles (the samples have the similar structure to MnP, but synthesized previously). The following maps, unlike the XRF mapping, are characterized by very narrow spatial resolution, in terms of 40-50 nm. According to the literature, at N-edge the transition at 397 eV appears only in the charged state. It can be associated to the transition from nitrogen 1s to the hybridized state with Fe(III) 3d $t_{2g}$ main character. In the pristine and discharged states, Fe species are divalent and the transition does not occur. The transition involves a state with high metal character, hence characterized by low intensity [111]. At Fe L-edge, NaC01 feature a typical Fe (III) fingerprint, whereas Pristine, NaD01 have Fe (II) pattern. The differences after 50th cycle are less pronounced, however, the transition below 710 eV is visible for NaC50 [112]. Turning to Mn L-edge, pristine and discharged states are typical Mn (II) fingerprints. L-edge has several features (Figure 30): I is characteristic for Mn (II) and disappears in charged state, II decrease in intensity with cycling and III can appear due to a new configuration of electronic states as a consequence of Jahn-Teller distorted Mn (III) [113].

*Table 10. List of samples for TXM measurements*

| Sample | Conditions |
|---|---|
| *Pristine* | *Formulated electrode* |
| *NaC01* | *Fully charged, 1 cycle* |
| *NaD01* | *Fully discharged, 1 cycle* |
| *NaC50* | *Fully charged, 50 cycles* |
| *NaD50* | *Fully discharged, 50 cycles* |

*Figure 41. Scheme illustrated charge/discharge processes of NaMnHCF sample*
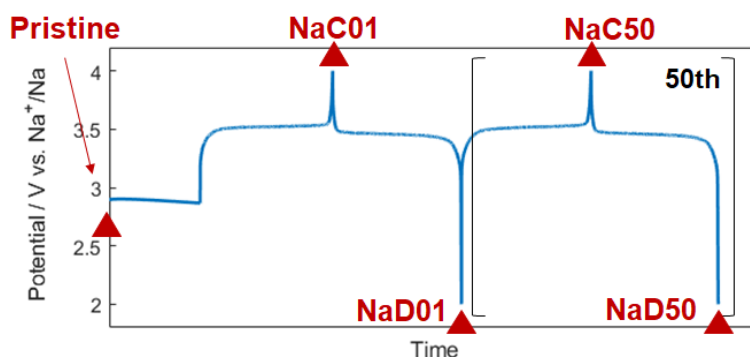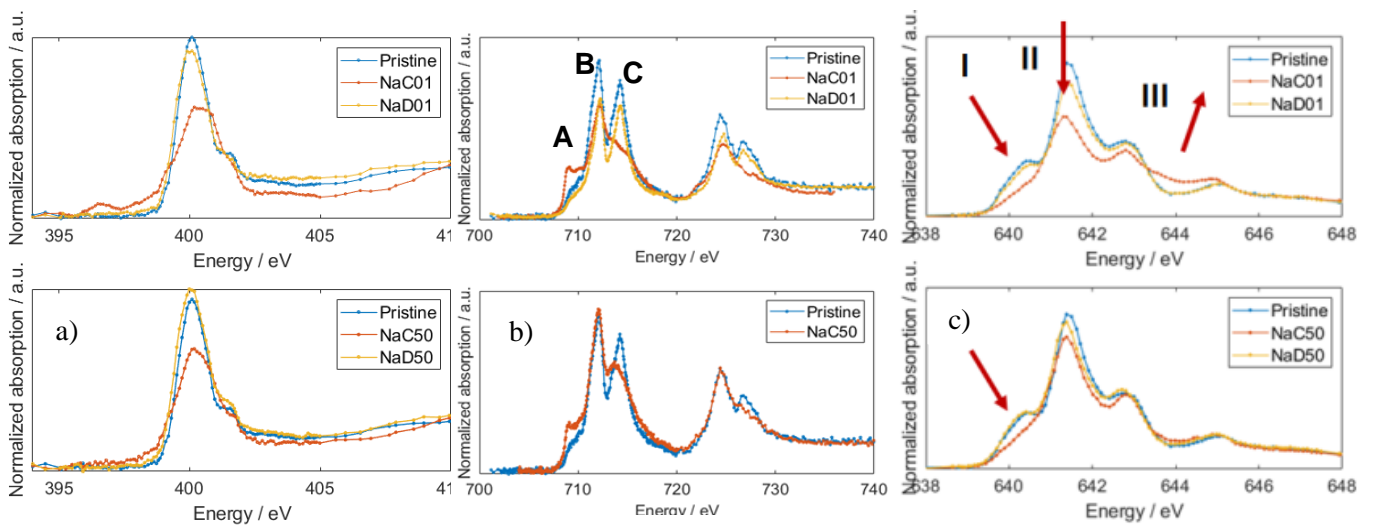
*Figure 42. X-ray absorption spectrum of a) N edge; b) Fe L-edge and c)Mn L-edge in different samples*

*Table 11. Characteristics of transitions at Fe L-edge*

| Fe L-edge | |
|---|---|
| *Transition A* | $2p \rightarrow 3d\ t_{2g}$<br>*visible only for Fe(III)*<br>*Fe(III) low spin $3d^5$ ($t_{2g}^5 + e_g^0$)* |
| *Transition B* | $2p \rightarrow 3d\ e_g$<br>*visible for both Fe(III) and Fe(II)*<br>*Fe(III) low spin 3d5 ($t_{2g}^5 + e_g^0$)*<br>*Fe(II) low spin 3d6 ($t_{2g}^6 + e_g^0$)* |
| *Transition C* | *$2p \rightarrow \pi^*(CN)$-3d(metal with $t_{2g}$ symmetry)        (π backdonation)*<br>*visible for both Fe(III) and Fe(II)*<br>*Fe(II) has higher backdonation than Fe(III)* |

At the beginning, for accurate assessing of the spectra, we should consider several factors such as  a) saturation and  b) presence of the carbon. Saturation can be checked from the scatter plot of peak versus preabsorption. For obtaining such plots, peak image and pre-absorption image were transformed to their corresponding matrices and then plotted against each other as usual xy plot. For example, as

shown in Figure 43, we can see that for NaC01 N edge, peak C is saturated at 1,5 where the linearity is already violated and quantifications can be effected.
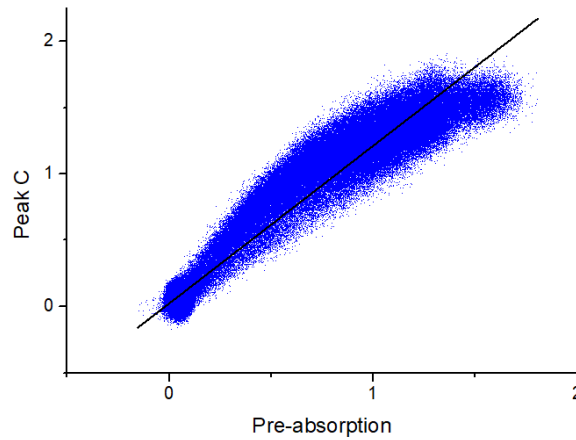


*Figure 43. Peak C vs. preabsorption*

Also we expect that the part of absorbance can come from the carbon. In the preabsorption part, signal is coming from both carbon and selected element, so as we are moving near to the edge, the absorbance of the element is raising whereas the absorbance of the carbon stays approximately the same. So by subtracting the preabsorption from the peak, we get the resulted image which is free from carbon contribution. By overlaying the resulting image to preabsorption image, the part with carbon will be highlighted. This can be confirmed by corresponded spectra of these highlighted regions. For instance, in NaC50 composite image (green color-peak-preabsorption, red color-preabsorption) (Figure 44), we can see that spectra of reddish zones show the high absorbance in the preedge region directly indicating the presence of carbon (in this case glass fiber from separator). The red zones can also correspond to the well-dispersed binder which has characteristics different from carbon.
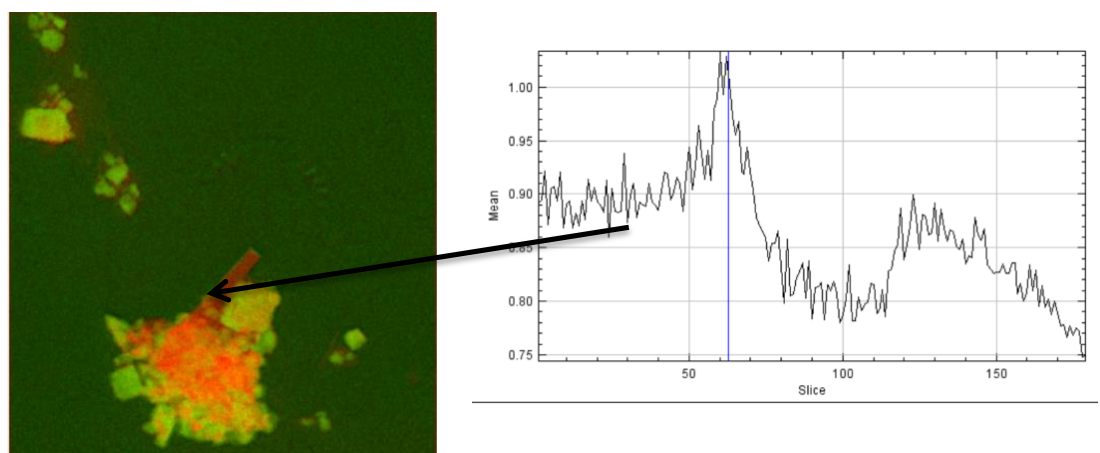


*Figure 44. Composite image of peak-preabsorption and preabsorption and corresponded spectrum*

Then we try to assess general homogeneity of the samples using so-called «core-shell» method. For that purpose, in NaC50 sample we choose the threshold values corresponded to bulk and surface to restrict these areas, plot corresponded spectra and compare them. The results are presented in Figure 45. For bulk we take range 0.8-1.5, for surface 0.2-0.8. As we can see, two spectra are perfectly correlated indicating that the composition inside and on the surface of the active material particles are quite similar.
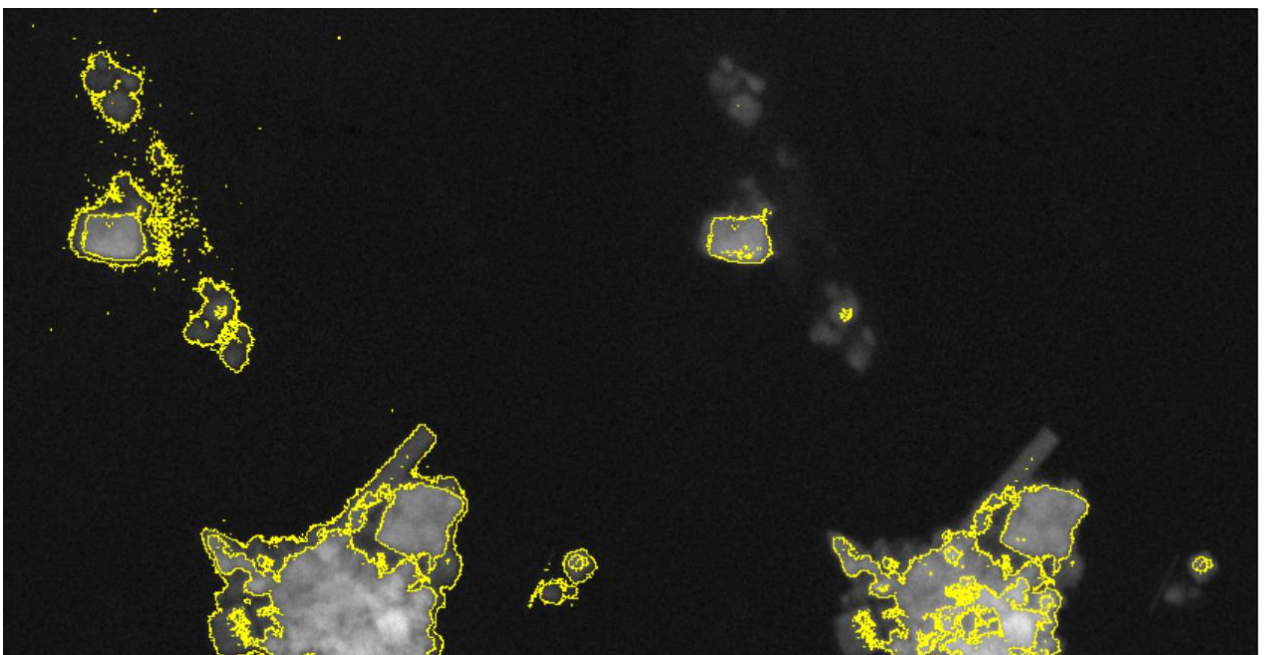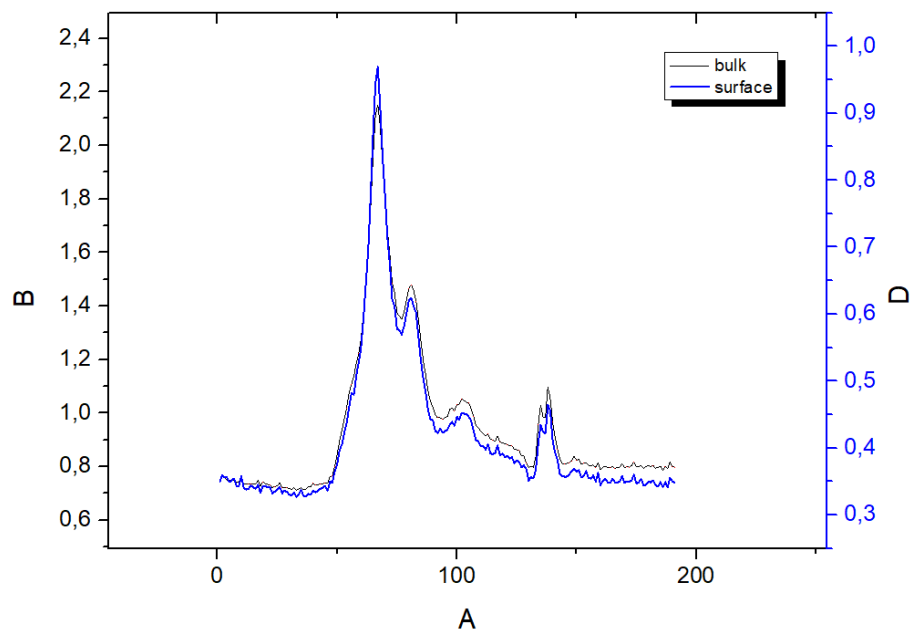
Plotting the average spectra of every sample at three different edges, we can see good correlation with spectra from literature. At Mn edge, in the discharged samples Peak at 640.2 eV is observed, whereas in the charged one it is absent. Looking at the Fe edge, it can be seen that Peak at 709 eV in NaC01 is intense, but after 50 cycles there is a mentionable decrease that can be attributed to the beginning of the intercalation. In the nitrogen edge, the same pattern with disappearance of peak at 396.6 eV with cycling is preserved.
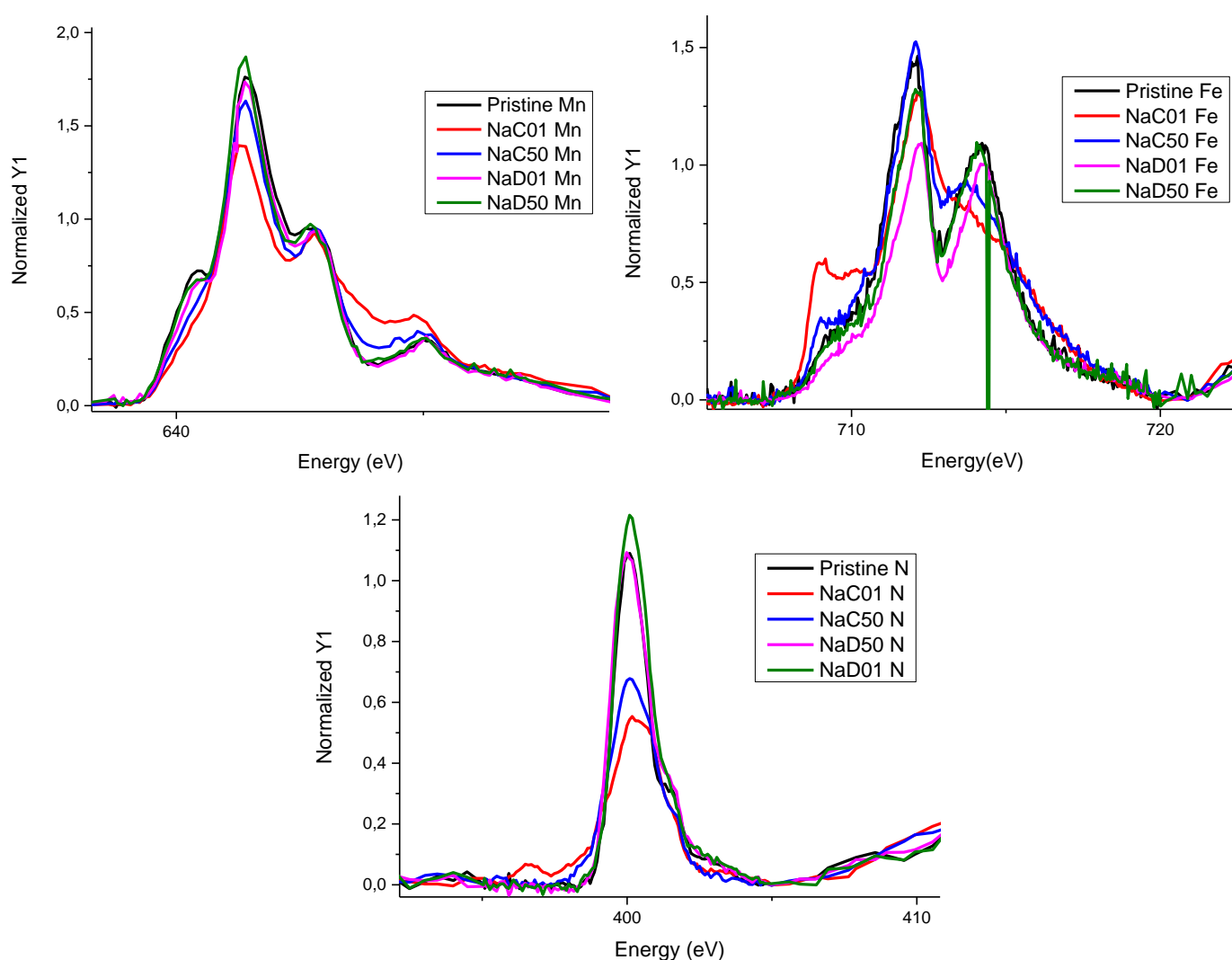


*Figure 46. Average spectra of every sample at Mn, Fe and N edges*

To check the presence of inhomogenities in manganese hexacyanoferrate samples after cycling, we start with the scatter plots to understand if we have some special regions where we can, for instance, find intercalated species in the charged samples. For that purpose, we plot Peak A-preabsorption versus Peak C-preabsorption in Origin software and divide the derived scatter plot on several regions which should catch the asymmetry of the cloud as shown in Figure 47. The points representing the identical spectra will have the same (Peak A-preabsorption/Peak C-preabsorption)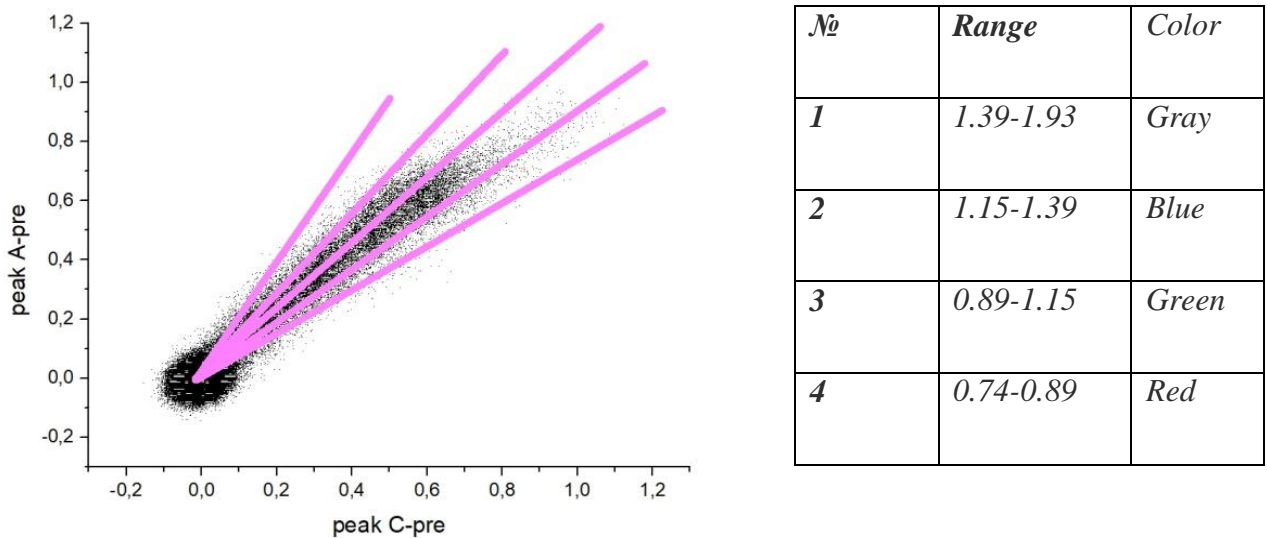 ratio and lay on the same line, being the distance from origin proportional to its intensity. Finding the slope (k value) of the lines we obtain the corresponding threshold values in the ratio map allowing us to create the masks showing the spatial distribution of the selected kind of the spectrum. After that these selections are applied on stack and the average spectrum of every selection should be obtained compared with discharged spectrum. Starting from the Mn-edge in NaC50 sample, we derived 4 regions from scatter plots which are corresponded to the threshold selection values as shown in Figure 47.



| № | Range | Color |
|---|---|---|
| 1 | 1.39-1.93 | Gray |
| 2 | 1.15-1.39 | Blue |
| 3 | 0.89-1.15 | Green |
| 4 | 0.74-0.89 | Red |

*Figure 47. The scatter plot of Peak A-preabsorption vs. Peak C-preabsorption (on the left) and corresponded regions derived from k values (on the right)*

After applying these four threshold selection on Peak A-preabsorption/Peak C-preabsorption image and creating corresponded masks, we use them on stack which are presented in Figure 48. For better understanding of the yellow selections, we show the selections overlapped with different colors. For that we create the composite maps using Colors>Merge channels function on Image J software. We can see that distribution of the particles is quite extensive, and it seems quite obvious that the spectra directly derived from the selected areas look too much the same (Figure 49). So we decide that

it would be better to take manually particles from particular regions (red, green,blue,gray) and plot their average spectra.
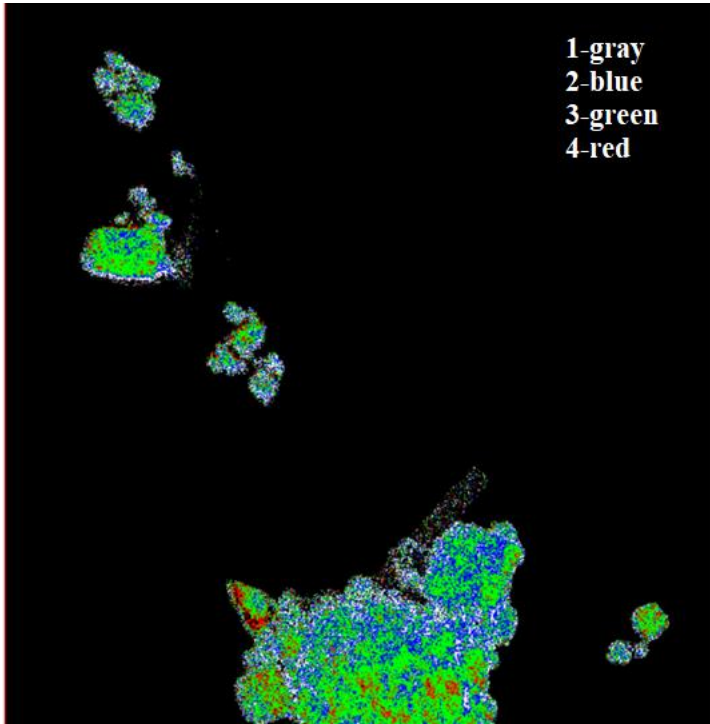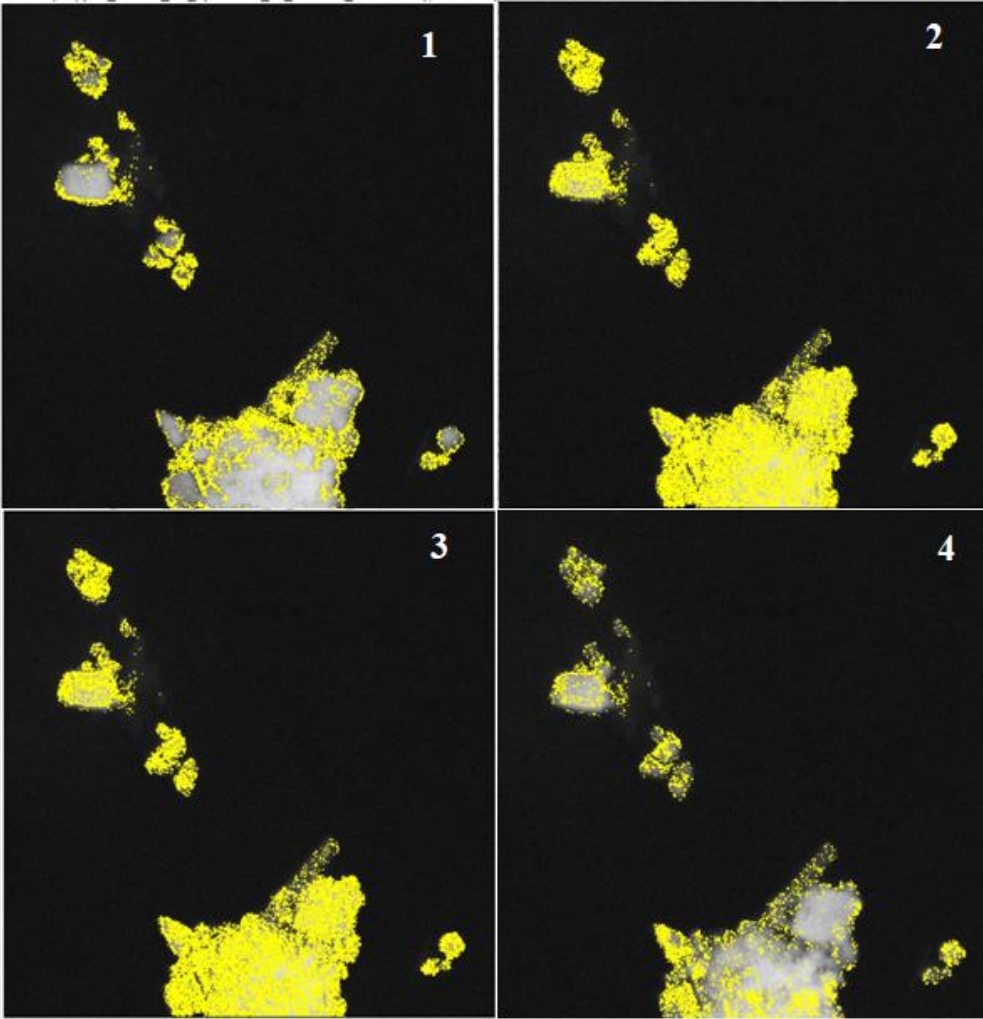




1-gray
2-blue
3-green
4-red
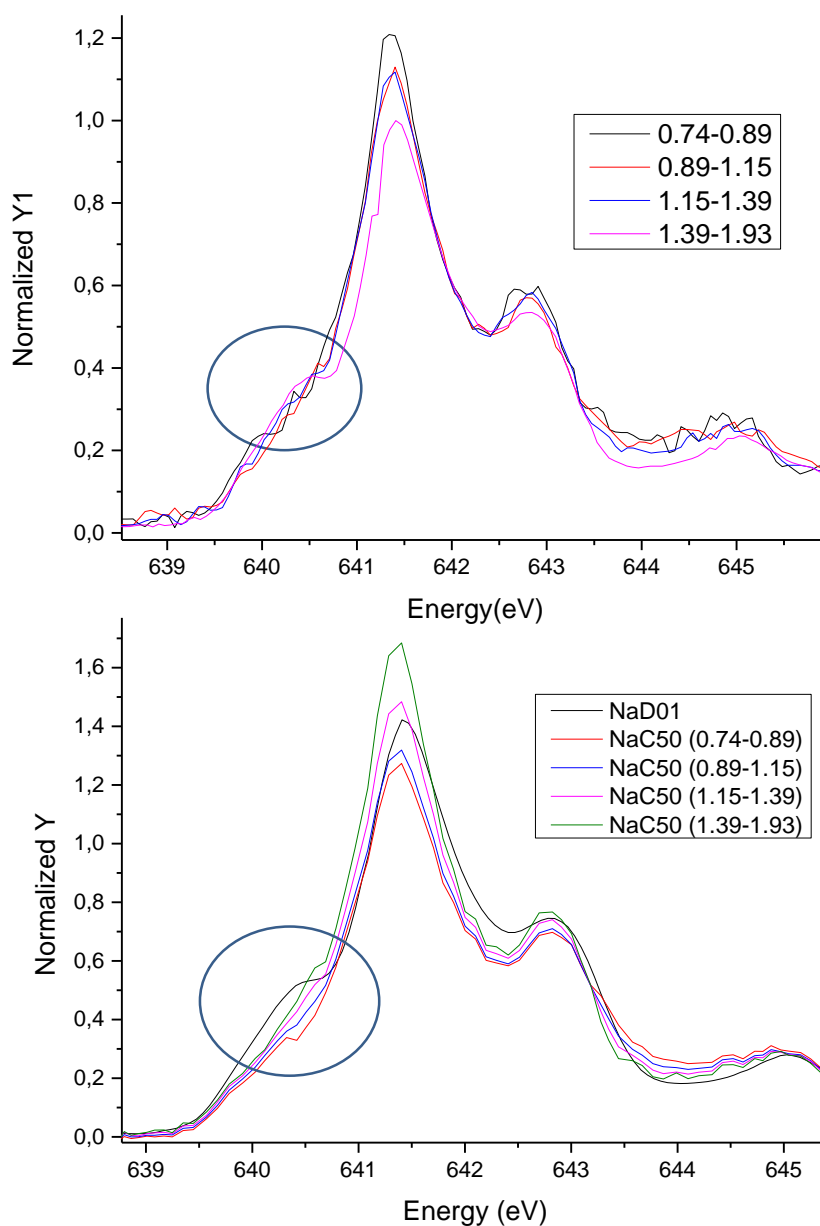
*Figure 49. (a) Spectra directly derived from the selected areas 1-4 (top); (b) Spectra derived from averaging 5 points from each area and compared with NaD01 spectrum (bottom)*

By close inspection of the selected areas, five particles from each region have been selected with visual maximum different spectra (coordinates of the particles are summarized in Appendix E). Then we subtract background, average, normalize to peak at 654 eV (to avoid saturation effect of peak B) and plot the spectra compared with NaD01 (Figure 49 b). As we can see, the difference between NaC50 Mn and NaD01 Mn are still quite obvious even though particles from the highest ratio (1.39-1.93) show some tendency to peak A appearance which can indicate small intercalation. But overall, it

can be said that there is no specific intercalated regions found in NaC50 Mn sample. This can be seen as a direct indication of homogeneity of the sodium manganese hexacyanoferrate sample and structural stability after 50 cycles.

The next step is to compare the spectra from NaC50 Mn with NaC01 Mn. If the regions of NaC50 are fully deintercalated, we should have the same spectra in NaC01. As we can see there is the same general pattern in spectra, but the beginning of intercalation visible at Peak A (which is responsible for presence of discharged particles) in the gray region is evident. Summarizing, we could say that independtly of number of cycles intercalation is really small which again confirm the structural stability of sodium hexacyanoferrate material.
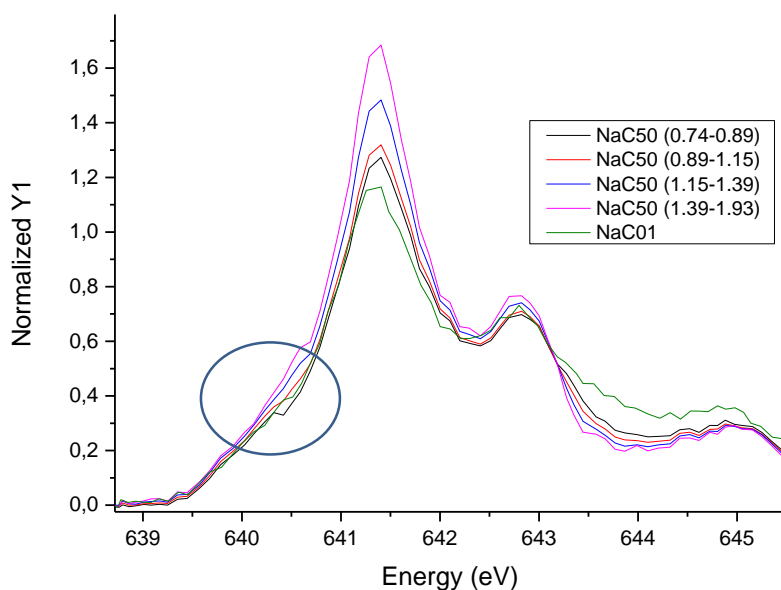


*Figure 50. Comparison between NaC50 Mn and NaC01 Mn spectra*

To assess the homogeneity of sodium manganese hexacyanoferrate samples, we can compare the obtained results with spectra of the sodium manganese hexacyanoferrate samples but cycled in Li electrolyte. As shown in Figure 51, in lithium samples, after the same procedure of manual selection of 5 points where intercalated species expected to be found, the correlation of derived spectrum with LiD01 spectrum is more obvious indicating the higher inhomogeneity of Li samples in comparison with Na ones.
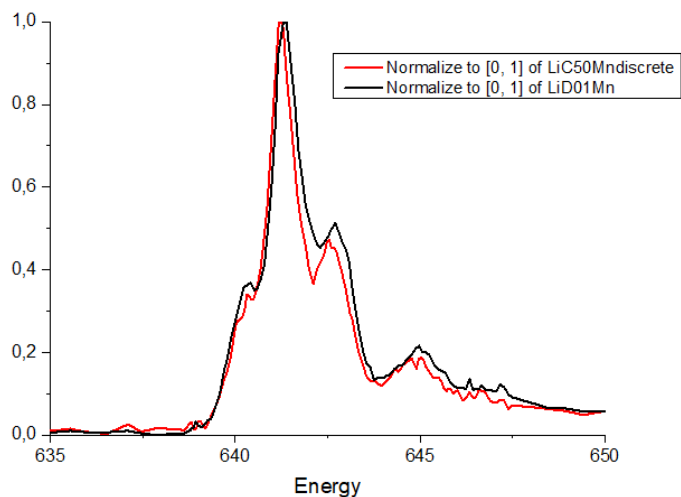
*Figure 51. Comparison between LiD50 (averaged 5 points) and LiD01 spectra*

We also try to find in the Fe edge the same regions we found in Mn. For that we again subtract the background, normalize (at peak 724 eV) and plot the spectra of the selected particles from NaC50 Fe and compare them with NaD01 Fe and NaC01 Fe. Resulting spectra are presented in Figure 52. In NaC01 Fe, we can see an intense Peak A, whereas Peak C is visible as a slope; on the other hand, in NaD01 Fe Peak A has practically disappeared and Peak C intensity significantly increased. In NaC50 Fe, the spectrum is intermediate between LiC01 Fe and LiD01 Fe: Peak A is observed however the intensity is lower than in NaC01, whereas peak C is also visible, but less intense than in LiD01 Fe. We could conclude that some partial intercalation is observed for iron species. Comparison with NaC01 Fe allows assessing the degree of intercalation: it is quite obvious that after 50 cycles intercalation of Fe species increased.
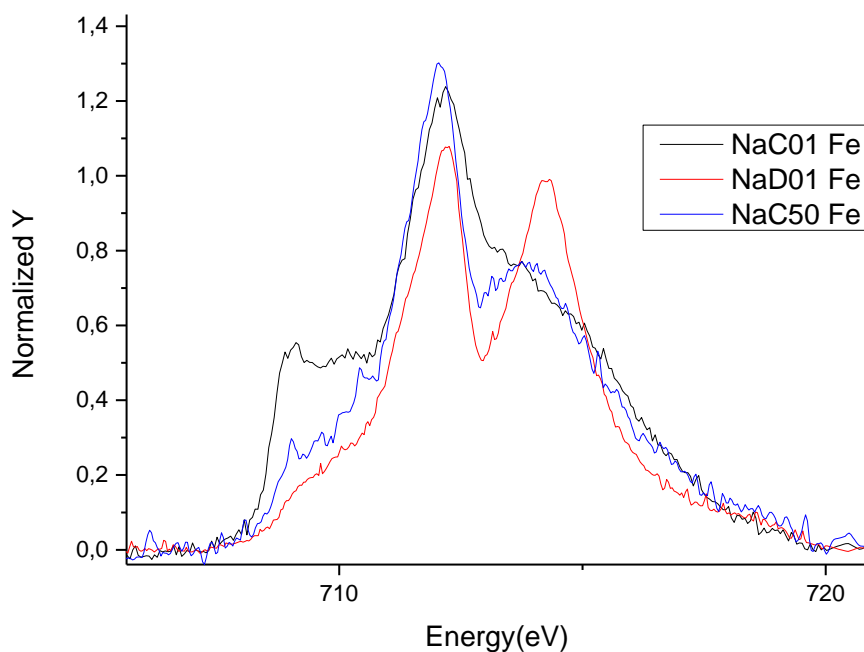


*Figure 52. Comparison between NaC50 Fe ,NaD01 Fe and NaC01 Fe spectra*

Turning to the nitrogen edge, we perform the same procedure as we do with Fe, searching for the same regions as in Mn and checking the presence of intercalation. The resulted spectra are presented in Figure. Peak A at 397 eV for NaC50 is not that flat as in NaD01. But, compared with NaC01, we can see mentionable decrease in intensity which can be an indication of the presence of intercalated species.
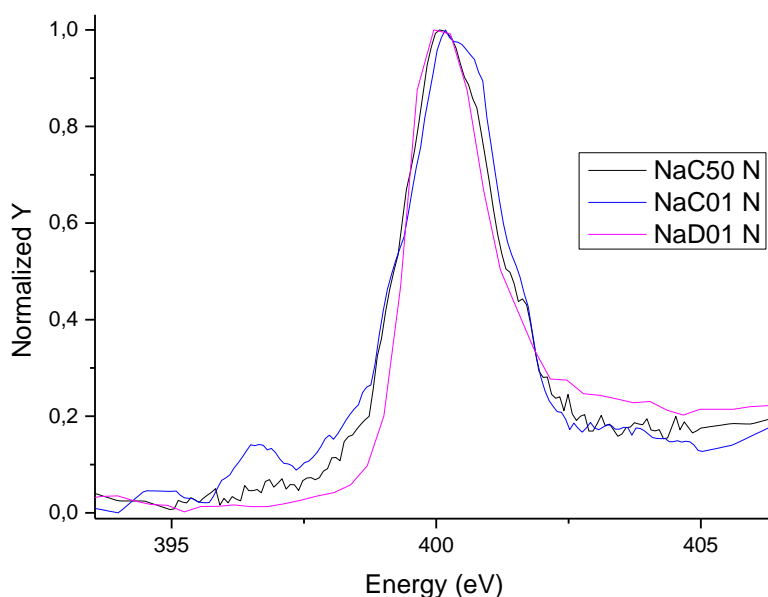


*Figure 53. Comparison between NaC50 N, NaD01 N spectra and NaC01 N spectra*

To sum up, after 50 cycles in NaC50 sample we found only slight indication of the presence of intercalated species. Starting with Mn-edge, several points have been found which show the beginning tendency of appearance of peak A (presented just in discharged sample) and the same pattern is observed at Fe-edge and N-edge ( where peak A is in an «intermediate» position between NaC01 and NaD01). It can be said that there is no specific regions found associated with big amount of intercalated species (rather particular points) and comparison with lithium sample shows the evident homogeneity of sodium samples confirming the general stability of sodium samples during the cycling. Despite the fact that the manual search and selection of intercalated particles can be rather tricky, we can say that use of the TXM technique can be helpful in determination of minor inhomogenities in cycled electrode materials.

# Conclusion

In this work, Manganese hexacyanoferrate (MnHCF) and its derivatives (MnHCF-A and MnHCF-C) have been synthesized by simple co-precipitation method and then characterized by means of the combination of the laboratory and synchrotron techniques. It has been found that addition of chelating agents has led to the relative increase of sodium content which was confirmed by means of MP-AES technique. XRD analysis has revealed that all three samples preserved the monoclinic structure ($P2_1/c$) of pristine material with negligible difference in lattice parameters and cell volume. Both XANES and EXAFS have verified the structural stability of the –Fe-C-N-Mn- pattern with just little difference in edge position and interatomic distances.

The electrochemical measurements of the synthesized samples have been performed by means of cyclic voltammetry tests using three-electrode system at different electrolyte concentrations. $Fe^{3+}/Fe^{2+}$ redox couple has been observed at approximately the same values in all samples, whereas $Mn^{3+/2+}$ peak has been found just in several cyclic voltammograms. We could say that by the means of CV tests, activation of second metallic center could not be confirmed with a great certainty. For that purpose, more extensive experiments should be done to find the optimal condition and repeat the tests for good reproducibility.

Then, structural stability of sodium manganese hexacyanoferrate electrode material has been tested using two different techniques: 2D XRF imaging and Transmission X-ray microscopy. By comparison of the XRF images, several hot spots have been found and corresponded micro XANES revealed the presence of some intercalated species. By manual search and selection of the intercalated particles in the TXM images at three different edges, we have detected the very beginning of the intercalation of sodium samples after 50 cycles. By accurate comparison with lithium samples, we can state that NaMnHCF is mostly homogeneous and has good structural stability relative to lithium samples after cycling.

# References

[1] Ould Ely Teyeb, Kamzabek Dana, Chakraborty Dhritiman., "Batteries Safety: Recent Progress and Current Challenges," *J. Frontiers in Energy Research,* no. 7, p. 71, 2019.

[2] Tarascon, J., Armand, M, "Issues and challenges facing rechargeable lithium batteries," *Nature,* no. 414, pp. 359-367, 2001.

[3] Naoki Nitta, Feixiang Wu, Jung Tae Lee, Gleb Yushin, "Li-ion battery materials: present and future," *Materials Today,* vol. 18, no. 5, pp. 252-264, 2015.

[4] Ikeda, H., Saito, T. & Tamura, H, "Manganese Dioxide Symposium," Cleveland, 1975.

[5] Thackeray, M. M., David, W. I. F., Bruce, P. G. & Goodenough, "Lithium insertion into manganese spinels," *J. B. Mat. Res.,* vol. 18, p. 461–472, 1983.

[6] Nagaura, T. & Tozawa, K, "Lithium ion rechargeable battery," *Prog. Batteries Solar Cells,* vol. 9, no. 209, 1990.

[7] Goodenough, J. B., and Kim, Y, "Challenges for rechargeable Li batteries," *Chem. Mater,* vol. 22, p. 587–603, 2009.

[8] Pan, H., Hu, Y-S., and Chen, L, "Room-temperature stationary sodiumion batteries for large-scale electric energy storage," *Energy Environ,* no. 6, p. 2338–2360, 2013.

[9] D. Brown, J. Philos., "Trans," 1724, pp. 33, 17.

[10] "Miscellanea Berolinensia and Incrementium Scientiarum," Berlin, 1710, p. 377.

[11] F.D. Miles, J.F. Keggin , "Structure and formulae of the Prussian blue and related compounds," *Nature,* no. 137, p. 577–578, 1936.

[12] F. Herren, P. Fisher, A. Ludi, and W. Halg, "Neutron difraction study of Prussian blue, Fe4[Fe(CN)6]3 xH2O. Location of water molecules and long-range magnetic order," *Inorgan. Chem,* no. 19, pp. 956-959, 1980.

[13] I.V.Tananaev, M.A.Glushkova and G.B.Seifer, *Zhur.Neorg.Khim,* no. 1, p. 66, 1956.

[14] Bull, S.-H. Lee and Y.-D. Huh., *Korean Chem. Soc,* no. 33, pp. 1078-1080, 2012.

[15] M.B. Zakaria, T. Chikyow, *Coordination Chemistry Reviews,* vol. 352, pp. 328-345,

2017.

[16]     T. Archived, Machine, Heyltex Corporation, 2007, pp. 11-12.

[17]     V. Neff., "Electrochemical oxidation and reduction of thin films of Prussian Blue," *J. Electrochem. Soc,* no. 25, pp. 886-887, 1978.

[18]     K. Itaya, H. Akahoshi, S. Toshima., "Electrochemistry of Prussian Blue modified electrodes: an electrochemical preparation method," *J. Electrochem. Soc.,* no. 129, pp. 1498-1500, 1982.

[19]     A. Karyakin, "Chemical and biological sensors based on electroactive inorganic polycrystals," *Academic Press ,* pp. 411-439, 2008.

[20]     Kevin Hurlbutt, Samuel Wheeler, Isaac Capone, Mauro Pasta, "Prussian Blue Analogs as Battery Materials," *Joule,* vol. 2, no. 10, pp. 1950-1960, 2018.

[21]     Yutaka Moritomo, Masamitsu Takachi, Yutaro Kurihara, "Thin Film Electrodes of Prussian blue Analogues with Rapid Li+ Intercalation," *Applied Physics Express,* vol. 5, no. 4, 2012.

[22]     Kevin Hurlbutt, Samuel Wheeler, Isaac Capone, Mauro Pasta, "Prussian Blue Analogs as Battery Materials," vol. 2, p. 1950–1960, 2018.

[23]     M. Okubo, D. Asakura,Y. Mizuno,J.-D. Kim,T. Mizokawa,T. Kudo,I. Honma., "Switching Redox-Active Sites by Valence Tautomerism in Prussian Blue Analogues AxMny[Fe(CN)6]•nH2O (A: K, Rb): Robust Frameworks for Reversible Li Storage," *J. Phys. Chem,* 2010.

[24]     C.D. Wessells, R.A. Huggins and Y. Cui, "Copper hexacyanoferrate battery electrodes with long cycle life and high power," *Nature Communication,* vol. 2, p. 550, 2011.

[25]     Y. Lu, L. Wang, J. Cheng and J.B. Goodenough, "Prussian blue: a new framework of electrode materials for sodium batteries," *Chem. Commun,* no. 48, pp. 6544-6546, 2012.

[26]     C.D. Wessells, S.V. Peddada, R.A. Huggins and Y. Cui., "Nickel hexacyanoferrate nanoparticle electrodes for aqueous sodium and potassium ion batteries," *Nano Lett,* no. 11, pp. 5421-5425, 2011.

[27]     Man Xie, Yongxin Huang,Menghao Xu,Renjie Chen,Xiaoxiao Zhang,Li Li Feng Wu, "Sodium titanium hexacyanoferrate as an environmentally friendly and low-cost cathode material for sodium-ion batteries," *Journal of Power Sources,* vol. 302, pp. 7-12, 2016.

[28]     H.J. Buser, A. Ludi, D. Schwarzenbach and W. Petter., "The crystal structure of Prussian blue: Fe4[Fe(CN)6]3•xH2O," *Inorg. Chem,* vol. 16, pp. 2704-2710, 1977.

[29]     Y.-M. Chiang, Y.-I. Jang, H. Wang, B. Huang, D.R. Sadoway and P. Ye., "Synthesis of LiCoO2 by decomposition and intercalation of hydroxide," *J. Electrochem. Soc.,* no.

145, p. 887, 1998.

[30]   M. Takachi, T. Matsuda and Y. Moritomo., "Redox reactions in prussian blue analogues against Li concentration," *J. Appl. Phys.,* no. 52, p. 9, 2013.

[31]   Y. Moritomo, K. Wakaume, M. Takachi, X.H. Zuo and H. Kamioka., "Li+ intercalation of manganese hexacyanoferrate as investigated by in situ valence-differential absorption spectroscopy.," *J. Appl. Phys,* vol. 52, p. 17, 2013.

[32]   Xiaomin Yan, Yang Yang, Ershuai Liu, Liqi Sun, Hong Wang, Xiao-Zhen Liao, Yushi He, Zi-Feng Ma, "Improved cycling performance of prussian blue cathode for sodium ion batteries by controlling operation voltage range," *Electrochimica Acta,* vol. 225, pp. 235-242, 2017.

[33]   L. Wang, Y. H. Lu, J. Liu, M. W. Xu, J. G. Cheng, D. W. Zhang,J. B. Goodenough, *Angew. Chem., Int. Ed.,* no. 52, p. 1964, 2013.

[34]   W. J. Li, S. L. Chou, J. Z. Wang, J. L. Wang, Q. F. Gu, H. K. Liu, S. X. Dou, *Nano Energy,* vol. 200, p. 13, 2015.

[35]   J. Song, L. Wang, Y. H. Lu, J. Liu, B. K. Guo, P. H. Xiao, J. J. Lee,X. Q. Yang, G. Henkelman, J. B. Goodenough, *J. Am. Chem. Soc.,* vol. 137, p. 2658, 2015.

[36]   Y. Tang, W. Zhang, L. Xue, X. Ding, T. Wang, X. Liu, J. Liu, X. Li and Y. Huang., "Polypyrrole-promoted superior cyclability and rate capability of NaxFe[Fe(CN)6] cathodes for sodium-ion batteries," *Journal of Materials Chemistry A,* vol. 4, pp. 6036-604, 2016.

[37]   Y. You, X.-L. Wu, Y.-X. Yin and Y.-G. Guo., "High-quality Prussian blue crystals as superior cathode materials for room-temperature sodium-ion batteries," *Energy & Environmental Science,* vol. 7, pp. 1643-1647, 2014.

[38]   X. Wu, C. Wu, C. Wei, L. Hu, J. Qian, Y. Cao, X. Ai, J. Wang and H. Yang., "Highly Crystallized Na2CoFe(CN)6 with Suppressed Lattice Defects as Superior Cathode Material for Sodium-Ion Batteries.," *ACS Appl. Mater. Interfaces,* vol. 8, pp. 5393-5399, 2016.

[39]   Y. Moritomo, S. Urase and T. Shibata., "Enhanced battery performance in manganese hexacyanoferrate by partial substitution," *Electrochimica Acta.,* vol. 210, pp. 963-969, 2016.

[40]   W.J. Li, S.L. Chou, J.Z. Wang, Y.M. Kang, J.L. Wang, Y. Liu, Q.F. Gu, H.K. Liu and S.X. Dou., "Facile method to synthesize Na-enriched Na1 + xFeFe(CN)6 frameworks as cathode with superior electrochemical performance for sodium-ion batteries," *Chemistry of Materials,* vol. 27, pp. 1997-2003, 2015.

[41]   McBreen, J., O'Grady, W.E., Pandya, K.I., "EXAFS: A New Tool for the Study of

Battery and Fuel Cell Materials," *Journal of Power Sources,* vol. 22, pp. 323-340, 1988.

[42] Delmas, C., Fouassier, C., and Hagenmuller, P, "Structural classification and properties of the layered oxides," *Physica,* vol. 99, p. 81–85, 1980.

[43] Ellis, B. L., and Nazar, L. F, "Sodium and sodium-ion energy storage batteries," *Curr. Opin. Solid State Mater,* vol. 16, p. 168–177, 2012.

[44] Stevens, D.A.; Dahn, J.R., "High Capacity Anode Materials for Rechargeable Sodium-Ion Batteries," *J. Electrochem. Soc.,* vol. 147, p. 1271–1273, 2000.

[45] Wessells, C. D., Huggins, R. A., and Cui, Y, "Copper hexacyanoferrate battery electrodes with long cycle life and high power," *Nat. Commun.,* vol. 2, no. 550, 2011.

[46] Jian, Z., Zhao, L., Pan, H., Hu, Y-S., Li, H., Chen, W., et al., "Carbon coated Na3V2(PO4)3 as novel electrode material for sodium ion batteries.," *Electrochem. Commun.,* vol. 14, p. 86–89, 2012.

[47] Gover, R. K. B., Bryan, A., Burns, P., and Barker, J., "The electrochemical insertion properties of sodium vanadium fluorophosphate, Na3V2(PO4)2F3," *Solid State Ionics,* no. 177, p. 1495–1500, 2006.

[48] Oh, S-M., Myung, S-T., Hassoun, J., Scrosati, B., and Sun, Y-K., "Reversible NaFePO4 electrode for sodium secondary batteries.," *Electrochem. Commun.,* vol. 22, p. 149–152., 2012.

[49] Mizushima, K., Jones, P. C., Wiseman, P. J., and Goodenough, J. B., "LixCoO2 a new cathode material for batteries of high energy density," *Mater. Res.,* vol. 15, p. 783–789, 1980.

[50] Doeff, M. M., Peng, M. Y., Ma, Y. P., and Dejonghe, L. C., "Orthorhombic NaxMnO2 as a cathode material for secondary sodium and lithium polymer batteries," *J. Electrochem. Soc.,* no. 141, p. 145–147, 1994.

[51] Sun, Q., Ren, Q-Q., Li, H., and Fu, Z-W., "High capacity Sb2O4 thin film electrodes for rechargeable sodium battery.," *Electrochem. Commun.,* vol. 13, p. 1462–1464., 2011.

[52] Wang, L.; Bi, X.; Yang, S., "Partially Singl-Crystalline Mesoporous Nb2O5 Nanosheets in between Graphene for Ultrafast Sodium Storage," *Adv. Mater.,* vol. 28, p. 7672–7679, 2016.

[53] J. Qian, C. Wu, Y. Cao, Z. Ma, Y. Huang, X. Ai, H. Yang, "Sodium-Ion Batteries: Prussian Blue Cathode Materials for Sodium-Ion Batteries and Other Ion Batteries," *Adv. Energy Mater,* vol. 17, no. 8, 2018.

[54] S.L. Hulbert, G.P. Williams, "SYNCHROTRON RADIATION SOURCES," *Vacuum Ultraviolet Spectroscopy,* 2000.

[55]  [Online]. Available: https://www.lightsource.ca/about_the_cls.

[56]  [Online]. Available: https://www.lightsource.ca/inside_the_synchrotron.

[57]  N. M. SERC, "SYNCHROTRON RADIATION SOURCES," *U.K Radiat. Phys. Chem,* vol. 45, no. 3, pp. 315-331, 995.

[58]  Bak, "In situ/operando synchrotron-based X-ray techniques for lithium-ion battery research," *NPG Asia Materials,* vol. 10, no. 5, pp. 563-580, 2018.

[59]  Y. Hirose, "Materials analysis using synchrotron radiation".

[60]  [Online]. Available: http://pd.chem.ucl.ac.uk/pdnn/inst2/work.htm.

[61]  M. Giorgetti, "A Review on the Structural Studies of Batteries and Host Materials by X-Ray Absorption Spectroscopy.," *ISRN Mater. Sci. ,* 2013.

[62]  Shearing, P., Wu, Y., Harris, S.J., Brandon, N., "In Situ X-Ray Spectroscopy and Imaging of Battery Materials.," *Electrochem. Soc. Interface.,* vol. 20, pp. 43-47, 2011.

[63]  Croy, J.R., Balasubramanian, M., Kim, D., Kang, S.-H., Thackeray, M.M., "Designing High-Capacity, Lithium-Ion Cathodes Using X-ray Absorption Spectroscopy.," *Chem. Mater.,* no. 23, p. 5415–5424, 2011.

[64]  Balasubramanian, M., Sun, X., Yang, X.Q., McBreen, J., "In Situ X-Ray Diffraction and X-Ray Absorption Studies of High-Rate Lithium-Ion Batteries.," *J. Power Sources.,* no. 92, pp. -8, 2001.

[65]  Angelo Mullaliu, Jakob Asenbauer, Giuliana Aquilanti, Stefano Passerini, Marco Giorgetti., "Highlighting the Reversible Manganese Electroactivity in Na-Rich Manganese Hexacyanoferrate Material for Li- and Na-Ion Storage," *Small Methods Journal,* 2020.

[66]  J. Song, L. Wang, Y.h.Lu, J. Liu, B.k. Guo, P.h. Xiao, J.-J. Lee, X.-Q. Yang, G. Henkelman, J. B. Goodenough., "Removal of Interstitial H2O in Hexacyanometallates for a Superior Cathode of a Sodium-Ion Battery.," *J. Am. Chem. Soc.,* vol. 137, pp. 2658-2664, 2015.

[67]  Y. Hiromi, "XAFS analysis and applications to carbon and catalysts," in *Carbon Alloys: Novel Concepts to Develop Carbon Science and Technology*, 2003, pp. 189-195.

[68]  Berry A J, Hack A C, Mavrogenes J A, Newville M and S R Sutton, "XANES study of Cu speciation in hightemperature brines using synthetic fluid inclusions," *Am Mineral,* pp. 1773-1782, 2006.

[69]  Yishida T, Tanaka S, "Fundamentals of X-ray absorption spectroscopy," *Analysis of Solid Surface I,* pp. 149-195, 1995.

[70] Tanaka, S. Yoshida and T., "Metal oxide catalysts," *X-ray Absorption Fine Structure for Catalysts and Structure,* p. 304–325, 1996.

[71] Abhijeet Gaur, B D Shrivastava and H L Nigam, "X-Ray Absorption Fine Structure (XAFS) Spectroscopy – A Review," *Proc Indian Natn Sci Acad,* vol. 79, no. 4, pp. 921-966, 2013.

[72] Gates Vol 1 Capter 12. 3, in *W P Handbook of clay science*, vol. 12, Elsevier.

[73] T. Chen, "Extracting structural information of higher coordination shells by analyzing EXAFS derivative spectrum," *Phys. Scr,* p. 93, 2018.

[74] Riggs-Gelasco P J, Stemmler T L and Penner-Hahn J E, "XAFS of dinuclear metal sites in proteins and model compounds," *Coord Chem Rev,* no. 144, pp. 245-286, 1995.

[75] Kelly S D, Hesterberg D and Ravel B, "Methods of soil analysis Part 5 Mineralogical Methods," *Soil Science Society of America,* vol. 14, no. 5, 2008.

[76] Yuan, Li-Xia & Wang, Zhaohui & Zhang, Wu-Xing & Hu, Xianluo & Chen, Ji-Tao & Huang, Yunhui & Goodenough, John, "Development and challenges of LiFePO4 cathode material for lithium-ion batteries," *Energy & Environmental Science,* pp. 269-284, 2010.

[77] Skoog, D.; Holler, F.; Crouch, S., Principles of Instrumental Analysis, 2007.

[78] [Online]. Available: https://chem.libretexts.org/Bookshelves/Analytical_Chemistry/Supplemental_Modules_(Analytical_Chemistry)/Instrumental_Analysis/Cyclic_Voltammetry#:~:text=Cyclic%20Voltammetry%20(CV)%20is%20an,and%20measuring%20the%20resulting%20current..

[79] [Online]. Available: https://www.ossila.com/pages/cyclic-voltammetry.

[80] [Online]. Available: https://en.wikipedia.org/wiki/Cyclic_voltammetry.

[81] Nicholson, R. S.; Shain, Irving., "Theory of Stationary Electrode Polarography. Single Scan and Cyclic Methods Applied to Reversible, Irreversible, and Kinetic Systems," *Analytical Chemistry.,* vol. 4, no. 36, p. 706–723, 1964.

[82] Noémie ElgKelley J. Rountree, Brian D. McCarthy, Eric S. Rountree, Thomas T. Eisenhart, and Jillian L. Dempsey, "A Practical Beginner's Guide to Cyclic Voltammetry," *Journal of Chemical Education,* vol. 2, no. 95, pp. 197-206, 2018.

[83] Kissinger, P. T., Heineman, W. R., "Cyclic Voltammetry," *Journal of Chemical Education,* vol. 60, no. 702, 1983.

[84] R. Nicholson, "Theory and Application of Cyclic Voltammetry for Measurement of

Electrode Reaction Kinetics," *Anal. Chem. ,* vol. 11, no. 37, p. 1351–1355, 1965.

[85]    DuVall, Stacy DuVall; McCreery, Richard, "Control of Catechol and Hydroquinone Electron-Transfer Kinetics on Native and Modified Glassy Carbon Electrodes," *Anal. Chem.,* vol. 20, no. 71, p. 4594–4602, 1999.

[86]    Bond, Alan M.; Feldberg, Stephen, "Analysis of Simulated Reversible Cyclic Voltammetric Responses for a Charged Redox Species in the Absence of Added Electrolyte," *J. Phys. Chem.,* vol. 49, no. 102, p. 9966–9974, 1998.

[87]    G. Carriedo, "The use of cyclic voltammetry in the study of the chemistry of metal carbonyls," *J.. Chem. Educ. ,* vol. 11, no. 65, p. 1020, 1988.

[88]    J. Telegdi, A. Shaban, G. Vastag, "Biocorrosion—Steel," *Encyclopedia of Interfacial Chemistry,* pp. 28-42, 2018.

[89]    Paul S. Nnamchi, Camillus S. Obayi, "Electrochemical Characterization of Nanomaterials," in *Characterization of Nanomaterials*, 2018, pp. 103-127.

[90]    A Beginners Guide Thermogravimetric Analysis, PerkinElmer.

[91]    Allen, Kyle & Coker, Eric & Auyeung, Nicholas & Klausner, James., "Cobalt Ferrite in YSZ for Use as Reactive Material in Solar Thermochemical Water and Carbon Dioxide Splitting, Part I: Material Characterization," *Journal of Minerals,* 2013.

[92]    Oisik Das, Nam Kyeun Kim, Mikael S.Hedenqvist, Debes Bhattacharyya, "The flammability of biocomposites," in *Durability and Life Prediction in Biocomposites, Fibre-Reinforced Composites and Hybrid Composites*, 2019, pp. 335-365.

[93]    W. Perkins, "Fourier Transform-Infrared Spectroscopy," *Journal of Chemical Education,* no. 63, 1986.

[94]    F. Daniels, J.W. Williams, P. Bender, R.A. Alberty, C.D. Cornwell, J. E. Harriman., Experimental Physical Chemistry, 7th Ed, 1970.

[95]    [Online]. Available: https://en.wikipedia.org/wiki/Fourier-transform_infrared_spectroscopy.

[96]    [Online]. Available: https://www.cbrnetechindex.com/Chemical-Detection/Technology-CD/Elemental-Analysis-CD-T/Microwave-Plasma-Atomic-Emission-Spectroscopy-CD-EA#:~:text=MP%2DAES%20consists%20of%20a,of%20major%20and%20minor%20elements.&text=The%20atomized%20sample%20passes%20t.

[97]    A. Technologies, MP AES application e-handbook, 2016.

[98]    "ALBA synchrotron, MISTRAL beamline," [Online]. Available: https://www.cells.es/en/beamlines/bl09-mistral.

[99] You, Y., Yu, X., Yin, Y., "Sodium iron hexacyanoferrate with high Na content as a Na-rich cathode material for Na-ion batteries.," *Nano Res.,* no. 8, p. 117–128, 2015.

[100] Yun Tang, Wei Li, Pingyuan Feng, Min Zhou, Kangli Wang, Yuesheng Wang, Karim Zaghib, Kai Jiang, "High-Performance Manganese Hexacyanoferrate with Cubic Structure as Superior Cathode Material for Sodium-Ion Batteries," *Advances Functional Materials,* vol. 30, no. 10, 2020.

[101] Zhilong Shen, Yunpo Sun, Jian Xie, Shuangyu Liu, Dagao Zhuang, Genlin Zhang, Wenquan Zheng, Gaoshao Caob and Xinbing Zhao, "Manganese hexacyanoferrate/graphene cathodes for sodium-ion batteries with superior rate capability and ultralong cycle life.," *Inorg.Chem.Front.,* vol. 5, pp. 2914-2920, 2018.

[102] L.J. Boucher, Mirjana Kotowski, Karl Koeber, Dieter Tille, Mn Manganese: Coordination Compounds 7.

[103] Wilde R.E, Ghosh S.N, Marshall B., *Journal of Inorganic Chemistry,* no. 9, p. 2512, 1970.

[104] H.A.Chu, M.T. Gardner,J.P.O'Brien,G.T.Babcock, *Biochemistry,* no. 38, pp. 4533-4541, 1999.

[105] Goodenough, Aijun Zhou Zemin Xu Hongcai Gao Leigang Xue Jingze Li John B., "Size-, Water-, and Defect-Regulated Potassium Manganese Hexacyanoferrate with Superior Cycling Stability and Rate Capability for Low-Cost Sodium-Ion Batteries," *Small Methods,* vol. 15, no. 42, 2019.

[106] Yang Liua, Yun Qiaoa, Wuxing Zhanga, Zhen Lia, Xiao Jic, "Sodium storage in Na-rich NaxFeFe(CN)6 nanocubes," *ElsevierLtd,* pp. 2211-2855, 2015.

[107] Adriano Filipponi, Andrea Di Cicco, and Calogero Renzo Natoli, "X-ray-absorption spectroscopy and n-body distribution functions in condensed matter. I. Theory," *Phys. Rev. B,* p. 52, 1995.

[108] M. Giorgetti, M. Berrettoni, A. Filipponi, P.J. Kulesza, R. Marassi, "Evidences for four body contribution in the EXAFS spectrum of Na2Co[Fe(CN)6]," *Chem. Phys. Lett. ,* vol. 275, pp. 108-112, 1997.

[109] Marco Giorgetti and Mario Berrettoni, "Structure of Fe/Co/Ni Hexacyanoferrate As Probed by Multiple Edge X-ray Absorption Spectroscopy," *Inorg. Chem. ,* vol. 47, no. 13, pp. 6001-6008, 2008.

[110] Mauro Pasta, Richard Y. Wang,Riccardo Ruffo, Ruimin Qiao, Hyun-Wook Lee,Michael F. Toney and Yi Cui, "Manganese–cobalt hexacyanoferrate cathodes for sodium ion batteries," *J. Mater. Chem. A,* vol. 4, p. 4211, 2016.

[111] Ali Firouzi, Ruimin Qiao,Colin D. Wessells, Wanli Yang,Yi-De Chuang,L. Andrew

Wray, Mai Fujimoto, "Monovalent manganese based anodes and cosolvent electrolyte for stable low-cost high-rate sodium ion batteries," *Nature Communications,* vol. 9, p. 861, 2018.

[112]   Rosalie K. Hocking, Erik C. Wasinger, Frank M. F. de Groot, Keith O. Hodgson, Britt Hedman, and Edward I. Solomon, "Fe L-Edge XAS Studies of K4[Fe(CN)6] and K3[Fe(CN)6]: A Direct Probe of Back-Bonding," *J. Am. Chem. Soc.,* vol. 128, no. 32, p. 10442–10451, 2006.

[113]   *Current Applied Physics,* no. 13, pp. 544-548, 2013.

[114]   M. F. T. a. Y. Cui, "Manganese–cobalt hexacyanoferrate cathodes for sodium ion batteries," *J. Mater. Chem. ,* vol. 4, 2016.

# Appendix A

## MP-AES calculations

| MnP | | | | | | |
|---|---|---|---|---|---|---|
| *Fe* | | | *Mn* | | *Na* | |
| *nm* | *ppm (mg/L)* | *nm* | *ppm* | *nm* | *ppm* | |
| *259.940* | *13.18* | *257.610* | *16.93* | *568.820* | *12.15* | |
| *373.486* | *13.12* | *280.108* | *16.00* | *588.995* | *11.10* | |
| *371.993* | *13.43* | *403.076* | *15.96* | *589.592* | *12.30* | |
| *Average* | *13.24* | | *16.30* | | *11.85* | |
| *Molar concentration (mmol/L)* | *0.24* | | *0.30* | | *0.52* | |
| *Molar ratio* | */ Fe* | *1* | | *1.25* | | *2.16* |
| | */ Mn* | *0.8* | | *1* | | *1.73* |

| MnA | | | | | | |
|---|---|---|---|---|---|---|
| *Fe* | | | *Mn* | | *Na* | |
| *nm* | *ppm (mg/L)* | *nm* | *ppm* | *nm* | *ppm* | |
| *259.940* | *14.11* | *257.610* | *16.36* | *568.820* | *12.68* | |
| *373.486* | *14.64* | *280.108* | *15.50* | *588.995* | *11.60* | |
| *371.993* | *14.00* | *403.076* | *15.55* | *589.592* | *12.66* | |
| *Average* | *14.25* | | *15.80* | | *12.31* | |
| *Molar concentration (mmol/L)* | *0.26* | | *0.29* | | *0.54* | |
| *Molar ratio* | */ Fe* | *1* | | *1.12* | | *2.07* |
| | */ Mn* | *0.89* | | *1* | | *1.85* |

| MnC | | | | | | |
|---|---|---|---|---|---|---|
| *Fe* | | | *Mn* | | *Na* | |
| *nm* | *ppm (mg/L)* | *nm* | *ppm* | *nm* | *ppm* | |
| *259.940* | *15.37* | *257.610* | *18.30* | *568.820* | *13.24* | |
| *373.486* | *15.72* | *280.108* | *17.25* | *588.995* | *12.36* | |
| *371.993* | *15.16* | *403.076* | *17.24* | *589.592* | *13.20* | |
| *Average* | *15.42* | | *17.60* | | *12.93* | |
| *Molar concentration (mmol/L)* | *0.28* | | *0.32* | | *0.56* | |
| *Molar ratio* | */ Fe* | *1* | | *1.14* | | *2.0* |
| | */ Mn* | *0.88* | | *1* | | *1.75* |

## Appendix B

## Results of XRD data treatment

| Mn-P | Coordinates | | | | |
|---|---|---|---|---|---|
| Atom label | *x* | y | z | *Wyckoff site position* | *Occupation* |
| Mn | *0.50000* | *0.50000* | *0.50000* | *2a* | *2.06* |
| Fe | *0.50000* | *0.00000* | *0.00000* | *2d* | *1.67* |
| N1 | *0.49939* | *0.31393* | *0.74298* | *4e* | *3.20* |
| N2 | *0.29412* | *0.50590* | *0.50582* | *4e* | *3.20* |
| N3 | *0.50173* | *0.26558* | *0.31835* | *4e* | *3.20* |
| C1 | *0.49796* | *0.19145* | *0.83494* | *4e* | *3.20* |
| C2 | *0.18931* | *0.49940* | *0.51831* | *4e* | *3.20* |
| C3 | *0.50246* | *0.16216* | *0.20308* | *4e* | *3.20* |
| O | *0.25400* | *0.21607* | *0.28021* | *4e* | *2.56* |
| Na | *0.28848* | *0.45552* | *0.00378* | *4e* | *6.9* |

| Mn-A | Coordinates | | | | |
|---|---|---|---|---|---|
| Atom label | *x* | y | z | *Wyckoff site position* | *Occupation* |
| Mn | *0.50000* | *0.50000* | *0.50000* | *2a* | *1.96* |
| Fe | *0.50000* | *0.00000* | *0.00000* | *2d* | *1.76* |
| N1 | *0.49939* | *0.31393* | *0.74298* | *4e* | *3.52* |
| N2 | *0.29412* | *0.50590* | *0.50582* | *4e* | *3.52* |
| N3 | *0.50173* | *0.26558* | *0.31835* | *4e* | *3.52* |
| C1 | *0.49796* | *0.19145* | *0.83494* | *4e* | *3.52* |
| C2 | *0.18931* | *0.49940* | *0.51831* | *4e* | *3.52* |
| C3 | *0.50246* | *0.16216* | *0.20308* | *4e* | *3.52* |
| O | *0.25400* | *0.21607* | *0.28021* | *4e* | *2.2* |
| Na | *0.25515* | *0.43296* | *0.01400* | *4e* | *7.4* |

| Mn-C | Coordinates | | | | |
|---|---|---|---|---|---|
| Atom label | x | y | z | Wyckoff site position | Occupation |
| Mn | 0.50000 | 0.50000 | 0.50000 | 2a | 1.78 |
| Fe | 0.50000 | 0.00000 | 0.00000 | 2d | 1.61 |
| N1 | 0.49939 | 0.31393 | 0.74298 | 4e | 3.56 |
| N2 | 0.29412 | 0.50590 | 0.50582 | 4e | 3.56 |
| N3 | 0.50173 | 0.26558 | 0.31835 | 4e | 3.56 |
| C1 | 0.49796 | 0.19145 | 0.83494 | 4e | 3.56 |
| C2 | 0.18931 | 0.49940 | 0.51831 | 4e | 3.56 |
| C3 | 0.50246 | 0.16216 | 0.20308 | 4e | 3.56 |
| O | 0.25400 | 0.21607 | 0.28021 | 4e | 2.16 |
| Na | 0.26109 | 0.43763 | 0.01099 | 4e | 7 |

| Space group | $P2_1/n$ |
|---|---|
| Symmetry operations | x, y, z <br> x, -y, -z <br> -x+1/2, y+1/2, -z+1/2 <br> x+1/2, -y+1/2, z+1/2 |

### Wyckoff Positions of Group $P2_1/c$ (No. 14) [unique axis b]

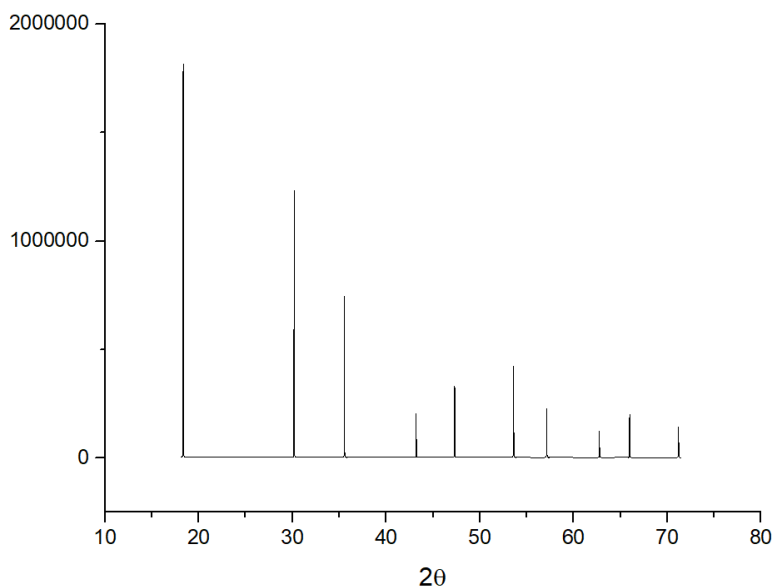| Multiplicity | Wyckoff letter | Site symmetry | Coordinates |
|---|---|---|---|
| 4 | e | 1 | (x,y,z) (-x,y+1/2,-z+1/2) (-x,-y,-z) (x,-y+1/2,z+1/2) |
| 2 | d | -1 | (1/2,0,1/2) (1/2,1/2,0) |
| 2 | c | -1 | (0,0,1/2) (0,1/2,0) |
| 2 | b | -1 | (1/2,0,0) (1/2,1/2,1/2) |
| 2 | a | -1 | (0,0,0) (0,1/2,1/2) |

*Figure 54. Si NIST XRD spectrum*

**Wyckoff Positions of Group *Fd*-3*m* (No. 227) [origin choice 2]**

| Multiplicity | Wyckoff letter | Site symmetry | Coordinates |
|---|---|---|---|
| | | | (0,0,0) + (0,1/2,1/2) + (1/2,0,1/2) + (1/2,1/2,0) + |
| 192 | i | 1 | (x,y,z) (-x+3/4,-y+1/4,z+1/2) (-x+1/4,y+1/2,-z+3/4) (x+1/2,-y+3/4,-z+1/4)<br>(z,x,y) (z+1/2,-x+3/4,-y+1/4) (-z+3/4,-x+1/4,y+1/2) (-z+1/4,x+1/2,-y+3/4)<br>(y,z,x) (-y+1/4,z+1/2,-x+3/4) (y+1/2,-z+3/4,-x+1/4) (-y+3/4,-z+1/4,x+1/2)<br>(y+3/4,x+1/4,-z+1/2) (-y,-x,-z) (y+1/4,-x+1/2,z+3/4) (-y+1/2,x+3/4,z+1/4)<br>(x+3/4,z+1/4,-y+1/2) (-x+1/2,z+3/4,y+1/4) (-x,-z,-y) (x+1/4,-z+1/2,y+3/4)<br>(z+3/4,y+1/4,-x+1/2) (z+1/4,-y+1/2,x+3/4) (-z+1/2,y+3/4,x+1/4) (-z,-y,-x)<br>(-x,-y,-z) (x+1/4,y+3/4,-z+1/2) (x+3/4,-y+1/2,z+1/4) (-x+1/2,y+1/4,z+3/4)<br>(-z,-x,-y) (-z+1/2,x+1/4,y+3/4) (z+1/4,x+3/4,-y+1/2) (z+3/4,-x+1/2,y+1/4)<br>(-y,-z,-x) (y+3/4,-z+1/2,x+1/4) (-y+1/2,z+1/4,x+3/4) (y+1/4,z+3/4,-x+1/2)<br>(-y+1/4,-x+3/4,z+1/2) (y,x,z) (-y+3/4,x+1/2,-z+1/4) (y+1/2,-x+1/4,-z+3/4)<br>(-x+1/4,-z+3/4,y+1/2) (x+1/2,-z+1/4,-y+3/4) (x,z,y) (-x+3/4,z+1/2,-y+1/4)<br>(-z+1/4,-y+3/4,x+1/2) (-z+3/4,y+1/2,-x+1/4) (z+1/2,-y+1/4,-x+3/4) (z,y,x) |
| 96 | h | ..2 | (0,y,-y) (3/4,-y+1/4,-y+1/2) (1/4,y+1/2,y+3/4) (1/2,-y+3/4,y+1/4)<br>(-y,0,y) (-y+1/2,3/4,-y+1/4) (y+3/4,1/4,y+1/2) (y+1/4,1/2,-y+3/4)<br>(y,-y,0) (-y+1/4,-y+1/2,3/4) (y+1/2,y+3/4,1/4) (-y+3/4,y+1/4,1/2)<br>(0,-y,y) (1/4,y+3/4,y+1/2) (3/4,-y+1/2,-y+1/4) (1/2,y+1/4,-y+3/4)<br>(y,0,-y) (y+1/2,1/4,y+3/4) (-y+1/4,3/4,-y+1/2) (-y+3/4,1/2,y+1/4)<br>(-y,y,0) (y+3/4,y+1/2,1/4) (-y+1/2,-y+1/4,3/4) (y+1/4,-y+3/4,1/2) |
| 96 | g | ..m | (x,x,z) (-x+3/4,-x+1/4,z+1/2) (-x+1/4,x+1/2,-z+3/4) (x+1/2,-x+3/4,-z+1/4)<br>(z,x,x) (z+1/2,-x+3/4,-x+1/4) (-z+3/4,-x+1/4,x+1/2) (-z+1/4,x+1/2,-x+3/4)<br>(x,z,x) (-x+1/4,z+1/2,-x+3/4) (x+1/2,-z+3/4,-x+1/4) (-x+3/4,-z+1/4,x+1/2)<br>(x+3/4,x+1/4,-z+1/2) (-x,-x,-z) (x+1/4,-x+1/2,z+3/4) (-x+1/2,x+3/4,z+1/4)<br>(x+3/4,z+1/4,-x+1/2) (-x+1/2,z+3/4,x+1/4) (-x,-z,-x) (x+1/4,-z+1/2,x+3/4)<br>(z+3/4,x+1/4,-x+1/2) (z+1/4,-x+1/2,x+3/4) (-z+1/2,x+3/4,x+1/4) (-z,-x,-x) |
| 48 | f | 2.m m | (x,1/8,1/8) (-x+3/4,1/8,5/8) (1/8,x,1/8) (5/8,-x+3/4,1/8)<br>(1/8,1/8,x) (1/8,5/8,-x+3/4) (7/8,x+1/4,3/8) (7/8,-x,7/8)<br>(x+3/4,3/8,3/8) (-x+1/2,7/8,3/8) (7/8,3/8,-x+1/2) (3/8,3/8,x+3/4) |
| 32 | e | .3m | (x,x,x) (-x+3/4,-x+1/4,x+1/2) (-x+1/4,x+1/2,-x+3/4) (x+1/2,-x+3/4,-x+1/4)<br>(x+3/4,x+1/4,-x+1/2) (-x,-x,-x) (x+1/4,-x+1/2,x+3/4) (-x+1/2,x+3/4,x+1/4) |
| 16 | d | .-3m | (1/2,1/2,1/2) (1/4,3/4,0) (3/4,0,1/4) (0,1/4,3/4) |
| 16 | c | .-3m | (0,0,0) (3/4,1/4,1/2) (1/4,1/2,3/4) (1/2,3/4,1/4) |
| 8 | b | -43m | (3/8,3/8,3/8) (1/8,5/8,1/8) |
| 8 | a | -43m | (1/8,1/8,1/8) (7/8,3/8,3/8) |

*Figure 55. Wyckoff positions of Si NIST symmetry group*
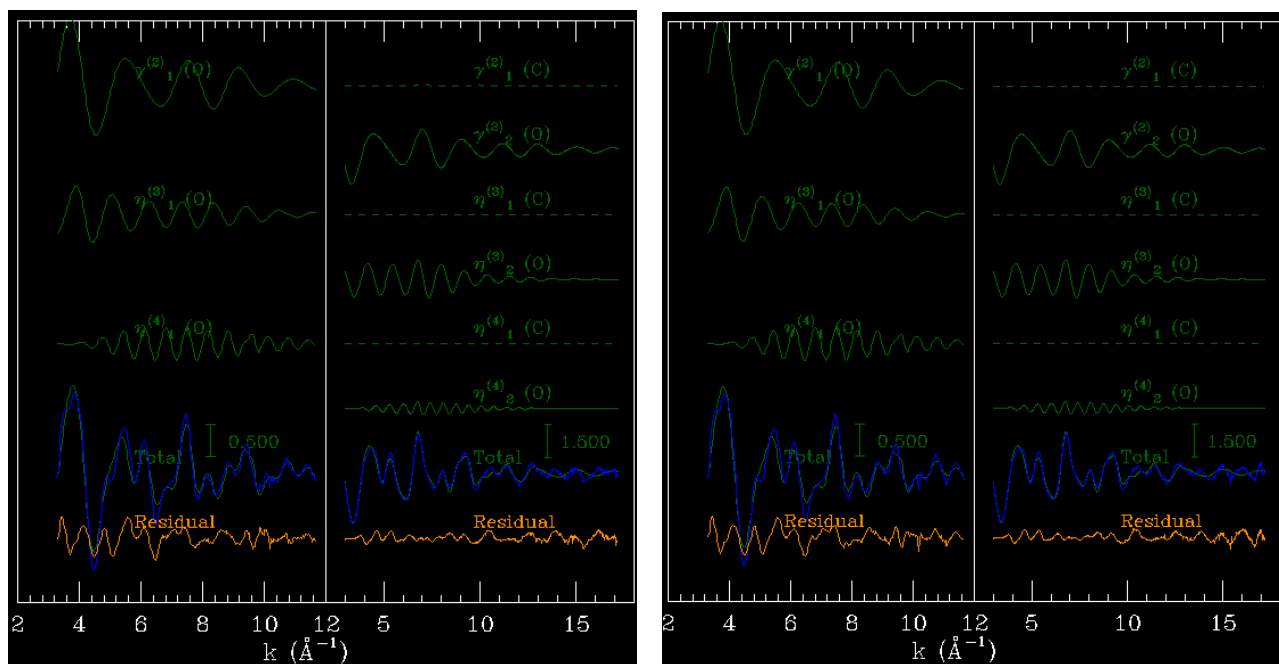
# Appendix C

## EXAFS fitting



*Figure 56. MnC (left) and MnA (right) EXAFS fitting*

## Appendix D

*Table 12. Masses of pellets for experiments with different electrolyte concentration*

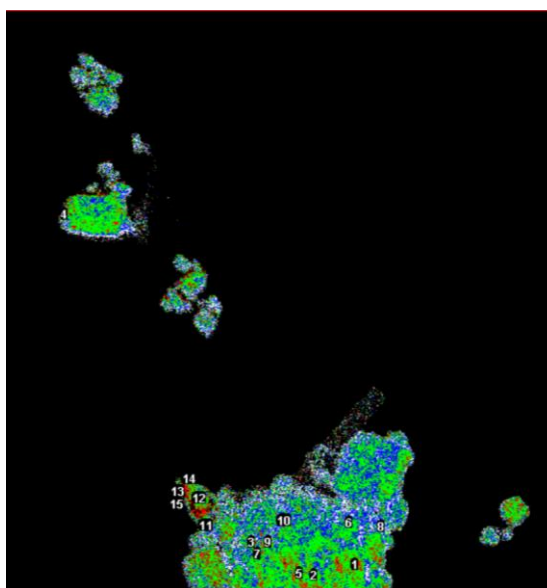| Electrolyte (M) | Pellet (mg) | Formula |
|---|---|---|
| NaNO$_3$ (0.1 M) | 1.75 | MnHCF |
| | 1.03 | MnHCF-A |
| | 1.89 | MnHCF-C |
| NaNO$_3$ (1 M) | 3,1 | MnHCF |
| | 1,71 | MnHCF-A |
| | 1,96 | MnHCF-C |
| NaNO$_3$ (5 M) | 3,34 | MnHCF |
| | 2,0 | MnHCF-A |
| | 1.76 | MnHCF-C |

**Appendix E**



*Figure 57. Position of chosen particle on composite image*

*Table 13. Coordinates of the points from different areas in NaC50 Mn sample.*

| Green area | x | y |
|---|---|---|
| 1 | 526 | 822 |
| 2 | 470 | 844 |
| 3 | 376 | 794 |
| 4 | 98 | 306 |
| 5 | 466 | 840 |
| Blue area | x | y |
| 1 | 522 | 765 |
| 2 | 426 | 762 |
| 3 | 386 | 812 |
| 4 | 570 | 771 |
| 5 | 386 | 802 |
| Red area | x | y |
| 1 | 310 | 769 |
| 2 | 300 | 729 |
| 3 | 268 | 719 |
| 4 | 263 | 710 |
| 5 | 267 | 717 |

## Acknowledgement

First of all I want to thank the ASC Erasmus Mundus Joint master degree program which accepted me and provided a unique opportunity to study at one of the best universities in Europe. This was an incredible journey which I will remember through years with a warm heart.

I want to thank my supervisor, Professor Marco Giorgetti, who always supported and guided me throughout my second year in University of Bologna. Thank you for giving me a chance to work and get new experience in the electrochemical field, and inspire me to continue my scientific career.

In addition, I want to thank Min Li, who was always so kind and patient in laboratory and really helped me in my electrochemical research. Separate thank to my colleague Mariam Maisuradze who was literally every day by my side and whom with all confidence I can now call one of my closest friend.

I want also to thank two people because of whom I start my path in science, my school teacher Tatyana Kim and my friend Bogdan Zagribelnyy, who a long time ago chose me to participate in the chemical competition, put in an enormous amount of time and efforts and believe in me. And after nine years I am still here, doing chemistry.

At last, I want to say thanks to my family: my parents and my sister who never understand what specifically I do in science but always encourage me to follow my dreams.